POLITECNICO DI MILANO
POLO REGIONALE DI LECCO

I Facoltà di Ingegneria Civile, Ambientale e Territoriale

Master of Science in Civil Engineering
CERM - Civil Engineering for Environmental Risks Mitigation

A Study on the Dynamic Response of Plates Subjected to Blast Loadings by means of Pressure-Impulse Diagrams

Supervisors: Ph.D. Matteo COLOMBO
Ph.D. Paolo MARTINELLI

Master Thesis of:
Marco SUTTI Matr. 734214
Luis Alejandro GONZALEZ Matr. 737449

Academic Year 2009/2010

Enimvēro is dēmum mihi vīvere atque fruī animā vidētur quī aliquō negōtiō intentus praeclārī facinoris aut artis bonae fāmam quaerit.

Sallustius

Acknowledgements

We owe our deepest gratitude to Ph.D. Matteo Colombo and Ph.D. Paolo Martinelli, supervisors of this thesis, for their assistance and patience.

Marco Sutti

My personal gratitude goes also to all my friends and to my family for their moral and financial support. It is quite emotional after all these years to be still here with all of you. However, I'm doing this also for all those people who could not be here.
A very special thanks goes to my dearest friend Lele, who was so close to me during this difficult year.
Special thanks also to my friend and thesis mate Luis Alejandro Gonzalez, who suffered me so much during the hard writing sessions of this thesis.

Luis Alejandro Gonzalez

It is an honour for me to have Marco Sutti as a friend, who worked with me side by side to make possible this work.
I thank God for taking me to this point of my life and showing me the good paths to be a better man every day. I thank my brothers for giving me inspiration, I thank my father for giving me force and support and I thank my mother for watching me every day from the heaven.
I am very grateful to Sutti and Bressani families for their support and for welcoming me to their families.

Abstract

Tunnels have recently become a very interesting case of study when special conditions like fire or blasting are taken into account. An accurate treatment of these special conditions is not usually familiar to many structural designers and this work tries to provide a useful tool for the assessment of structural elements under blasting phenomena (or general vibration), with particular focus on tunnel structures.

In order to analyse the behaviour of the shell structure of a tunnel, it is useful to evaluate the material and load conditions through experimental test. The shock tube test is specifically created to simulate accurately the shock pressure produced by an explosion. The shock tube test is intended to evaluate the maximum resistance of circular plates made in different materials and under several boundary conditions.

In this work, simplified models are proposed for the analysis of circular plates made in traditional reinforced concrete (R/C) and fibre-reinforced concrete (FRC). These materials are commonly used in design of tunnels and many other structures on which this work can be applied. By means of energetic processes it is possible to reduce a bidimensional structure with distributed mass an elasticity into a generalized single-degree-of-freedom system. This simplification allows to treat the dynamic issues in an easier way.

This work analyses the maximum resistance of circular plates in two cases: a simply supported plate and a plate resting on a Winkler-type soil. The aim of these analyses is the development of pressure-impulse diagrams for several pulse shapes. Pressure-impulse diagrams are created analogously to bending-axial force diagrams in columns, and they represent a very useful graphical method for the preliminary assessment of structural components subjected to blast loadings. In fact, according to the conditions of a plate sample (amongst them: pressure, pulse shape, material characteristics), it is possible to know immediately if the structure will be damaged, just placing a point in the pressure-impulse diagram.

Keywords: blast loadings, structural assessment, SDOF systems, circular plates, pressure-impulse diagrams, collapse mechanism.

Sommario

Lo studio delle gallerie in presenza di azioni eccezionali come incendi o esplosioni è recentemente diventato di grande interesse. Solitamente il progettista non è familiare ad una trattazione accurata di tali azioni, e questo lavoro cerca di fornire un utile strumento per l'assessment di strutture sottoposte ad esplosione, con particolare riguardo alle gallerie.

Per analizzare il comportamento di un concio di galleria, è utile effettuare dei test sperimentali ipotizzando materiali e condizioni di carico. Lo shock tube è uno strumento appositamente creato per simulare l'onda d'urto prodotta da un'esplosione. Con lo shock tube test si cerca di valutare la resistenza massima di piastre circolari per diversi materiali e diverse condizioni al contorno.

In questo lavoro vengono proposti dei modelli semplificati per l'analisi di piastre circolari realizzate in calcestruzzo armato o fibrorinforzato. Questi materiali sono comunemente usati nella progettazione di gallerie e molte altre strutture a cui questo lavoro può essere applicato. Attraverso approcci energetici una struttura bidimensionale avente massa ed elasticità distribuite può essere ricondotta ad un sistema ad un grado di libertà generalizzato. Questa semplificazione consente di trattare in maniera più semplice il problema dinamico.

Questo lavoro analizza la resistenza massima di una piastra circolare in due casi: una piastra semplicemente appoggiata ed una piastra su suolo elastico alla Winkler. L'obiettivo di queste analisi è lo sviluppo di diagrammi pressione-impulso per diverse forme di carico. I diagrammi pressione-impulso vengono costruiti in modo analogo ai diagrammi di interazione momento-azione assiale per le colonne, e rappresentano un metodo grafico molto utile per l'assessment preliminare degli elementi strutturali soggetti a carichi esplosivi. Infatti, in funzione delle condizioni a cui è soggetta una piastra assunta come provino (tra cui la pressione massima, la forma dell'impulso, le caratteristiche dei materiali), è possibile determinare immediatamente se la struttura risulterà danneggiata, collocando un punto nel diagramma pressione-impulso.

Parole chiave: carichi esplosivi, assessment strutturale, sistemi ad un grado di libertà, piastre circolari, diagrammi pressione-impulso, meccanismo di collasso.

Contents

List of Symbols

p	overpressure
t	time
p_0	peak instantaneous overpressure; intensity of a uniform distributed load
R	distance of the point of measurement from the centre of the explosion; circular plate radius
E	instantaneous energy release; concrete Young modulus
t_0	duration of the positive phase
K	non-dimensional parameter; kinetic energy
K_1	dimensional parameter
W	equivalent weight of an explosive charge in TNT
x, y, z	rectangular coordinates
z	normalized distance from the center of the explosion; vertical distance of a point from the plate middle plane
σ_z	local stress in the z direction
a	length dimension of a rectangular plate; acceleration
b	width dimension of a rectangular plate; load radius in the slab on grade example; base of a structural element section
u	local displacement component in the x direction
v	local displacement component in the y direction; velocity
$w(x, y)$	middle plane displacement in the vertical direction z
$\underline{s}(x, y, z)$	vector of local displacements
$\varphi_x(x, y)$	rotation around the y axis occurring in the x-z plane
$\varphi_y(x, y)$	rotation around the x axis occurring in the y-z plane
$\underline{U}$	vector of generalized displacements
$\underline{\underline{n}}$	correlation matrix between local and generalized displacements
ε_x, ε_y, ε_z	elongation strains
γ_{xy}, γ_{xz}, γ_{yz}	shear strains
$\underline{q}$	vector of generalized strains
$\underline{\underline{b}}$	correlation matrix between local and generalized strains
χ_x	curvature in the x-z plane
χ_y	curvature in the y-z plane
χ_{xy}	torsional curvature

t_x	shear angular deformation in the x-z plane
t_y	shear angular deformation in the y-z plane
$\underline{F}$	vector of the volume forces
F_x, F_y, F_z	volume forces
W_E	external work
W_I	internal work
δ	indicates the virtual quantities
$\underline{P}$	vector of the generalized loads
$p(x,y)$	surface distributed load in the direction z
$m_x(x,y)$	distributed moment per unit length acting in the x-z plane
$m_y(x,y)$	distributed moment per unit length acting in the y-z plane
h	plate thickness
$\delta\underline{\widehat{\varepsilon}}$	virtual local strains
$\underline{\sigma}$	vector of the local stresses
$\underline{\varepsilon}$	vector of the local strains
$\underline{Q}$	vector containing the generalized stresses
σ_x, σ_y	normal stresses in the x and y direction
τ_{xy}	shear stress acting on the surface of normal x in the direction y
τ_{xz}	shear stress acting on the surface of normal x in the direction z
τ_{yz}	shear stress acting on the surface of normal y in the direction z
M_x	bending moment acting in the x-z plane
M_y	bending moment acting in the y-z plane
M_{xy}	torsional moment
V_x	shear force acting in the y-z plane
V_y	shear force acting in the x-z plane
M'_x	incremented bending moment acting in the x-z plane
M'_y	incremented bending moment acting in the y-z plane
M'_{xy}	incremented torsional moment
V'_x	incremented shear force acting in the y-z plane
V'_y	incremented shear force acting in the x-z plane
$\underline{\underline{D}}$	stiffness matrix containing the elastic constants
ν	Poisson modulus; order of the Bessel function of the first kind
Ω	elastic strain energy
$\underline{\underline{D}}^*$	generalized stiffness matrix
$\overline{D}$	flexural rigidity of a plate
G	shear modulus
I	moment of inertia of a unit length element; total impulse
r, θ	polar coordinates
χ_r, χ_θ, $\chi_{r\theta}$	curvatures in polar coordinates
M_r	bending moment acting in the r direction
M_θ	bending moment acting in the θ direction
$M_{r\theta}$	torsional moment in polar coordinates
U, U_{el}	elastic strain energy
∇^4	laplacian operator of the fourth order

∇_r^4	laplacian operator of the fourth order in polar coordinates
$w(r)$, $w(r,t)$	plate vertical displacement in polar coordinates
w_h	solution of the homogeneous differential equation of plates
w_p	particular solution of the differential equation of plates
C_1, C_2, C_3, C_4	constants to be evaluated from the boundary conditions
$f_I(r,t)$	inertia forces
ρ	concrete density
$z(t)$, $\dot{z}(t)$, $\ddot{z}(t)$	generalized coordinate and its time derivatives
$\psi(r)$, $\psi_{el}(r)$, $\psi_{pl}(r)$	shape function, elastic shape function and plastic shape function
m^*, c^*, k^*, $p^*(t)$	generalized mass, generalized damping, generalized stiffness and generalized load of the equivalent SDOF system; with $_e$ they refer to the elastic stage, with $_p$ to the plastic one
K_M, K_R, K_L	normalized version of the transformation coefficients with ^{e} they refer to the elastic stage, with ^{p} to the plastic one
m_t	total mass
k_t	force per unit displacement
$p_t(t)$	total load
$p(r,t)$	dynamic load in polar coordinates
$p(t)$	dynamic load in polar coordinates; load-time curve
L^*	multiplier coefficient to get $p^*(t)$
χ_r, χ_θ, $\chi_{r\theta}$	curvatures in polar coordinates
U_{max}	maximum elastic strain energy
K_{max}	maximum kinetic energy
ω	natural frequency of vibration of the plate
w_{el}	plate displacement at the elastic limit
F_s	resistance force
F_{su}	ultimate resistance force (or collapse load)
$\widetilde{w}_{max}$	damage threshold
w_{max}	maximum displacement in the slab, $w(r=0,t)$; when talking about pressure-impulse diagrams it denotes also the maximum displacement reached during the time history
$\dot{w}$	incremental displacement
$\dot{F}_s$	incremental resistance force
p_{max}	peak load of the load-time function
t_r	rise time to reach the peak load p_{max}
t_d	total time duration of the pulse
λ	coefficient of the exponential pulse function
$\triangle t$	time-step in the average acceleration method
i	iteration index; specific impulse
$_i$	subscript that indicates the quantities at the i-th time-step
$_{i+1}$	subscript that indicates the quantities at the $_{i+1}$-th time-step
t_m	time to reach the maximum value of a response parameter
$K.E.$	kinetic energy of the system at time zero
$S.E.$	strain energy of the system at maximum displacement
$W.E.$	maximum work done by the load
$(i_0; p_0)$	coordinates of the pivot point in the p-i diagram
k, kk	dilation factor for locating the pivot point

ϕ_i	angle in the p-i diagram searching algorithm
Δs	spatial step in the p-i diagram searching algorithm
f	indicates the value given by $(w_{max} - \widetilde{w}_{max})$
ε_j	error of convergence at j-th iteration
α	angle separating the two sectors in the p-i diagram
$i.a.$	impulsive asymptote
$q.s.a.$	quasi-static asymptote
f_{yd}	design yielding stress of steel
f_{yk}	characteristic yielding stress of steel
ε_{yd}	design yielding strain of steel
E_s	steel Young modulus
ε_{sd}	design steel strain at ultimate deformation
f_{ck}	cylindrical characteristic strength of concrete
f_{cd}	design ultimate strength of concrete
f_{cu}	ultimate strength of concrete under fatigue
ε_{cu}	ultimate strain of high strength concrete
A_s	specific steel area per unit length
n_{rebar}, ϕ	number and diameter of the reinforcement bars
ρ_s	geometrical steel ratio
χ_b	ductility ratio
d	effective distance, equal to $h - c$; radius of the negative circular yield line
c	concrete cover of the steel reinforcement
x	neutral axis position
m_0	ultimate bending moment resistance per unit length
$CTOD_u$	ultimate crack tip opening displacement
l_{cs}	characteristic length for a FRC element
σ_s, ε_s	stress and deformation in the reinforcement steel
y	distance between the lower reinforcement and the neutral axis in elastic cracked phase
s_{rm}	average distance between cracks
E_c	concrete Young modulus
ξ	non-dimensional coefficient equal to 1.0
k_1	coefficient equal to 0.8 for ribbed bars and equal to 1.6 for smooth bars
k_2	coefficient equal to 0.5 for simple or compound bending with $y \leq h$ and equal to 1.0 for tension or compound bending with $y > h$
ε_{Ftu}	ultimate tensile strain of the FRC
f_{Ftsk}	residual characteristic tensile strength at serviceability limit state
f_{eq1}, f_{eq2}	mean values of the FRC tensile strength computed in a given interval of crack opening
f_{Ftuk}	ultimate characteristic tensile strength of the FRC
$CTOD_2$	crack tip opening displacement equal to 2.5 mm
f_{Ftud}	design ultimate tensile strength
f_{Ftsd}	residual design tensile strength at serviceability limit state
ϕ_θ	rotation about the radial yield line in the θ direction
δ	virtual displacement

U_{el}	elastic strain energy
W^{el}_{max}	maximum work in an elastic system
U_{ep}	elastoplastic strain energy
W^{pl}_{max}	maximum work in an elastoplastic system
$\overline{m}$	specific mass per unit area
A_{load}	plate area occupied by the load
k_s, k_{soil}	soil elastic modulus (Winkler constant)
$w_1(r)$	deflection of the slab within the loaded region
$w_2(r)$	deflection of the slab within the unloaded region
l, l_c	characteristic length, equal to $\sqrt[4]{D/k_s}$
ζ	dimensionless coordinate, equal to r/l
Z_1, Z_3, Z_3, Z_4	functions defined to obtain the elastic solution of a circular slab on grade
$J_0\left(\zeta\sqrt{i}\right)$	Bessel function of the first kind of zero order
$H_0^{(1)}\left(\zeta\sqrt{i}\right)$	Hankel function of the first kind of zero order
$Y_\nu(z)$	Bessel function of the first kind of ν order
Q_r	shear force in a circular plate
$\triangle r$	spatial step for the numerical integration
q, q_0	subgrade reaction
W_p	work done by the applied load
W_q	work done by the upward subgrade reaction
W_r	internal energy dissipation by the radial yield lines
W_d	internal energy dissipation by the circular yield line
ϕ_d	rotation about the circular yield line in the radial direction
v_0	initial velocity
$w_{plate+soil}$	denote the midspan displacement of the overall plate-soil system

List of Figures

List of Tables

Introduction

It is very well known the importance of safety in civil structures and moreover, during the last years, it has been highlighted and required by the national and international codes of design and construction, in order to avoid disaster events. These requirements have been evolving along the time, making them more rigorous. This evolution is coming from the necessity to take into account real factors that influence the structural behaviour, factors which were not considered in the past or new factors created by the human behaviour evolution. In the same way, new tools or more efficient tools are needed in order to supply this necessity, having an evolution of design techniques as well.

Blasting is one of those new factors which has gained great importance and popularity during the last years. The evidence of this fact could be illustrated by many examples like explosion of storage flammable materials, vehicle collisions, terrorist attacks and others (Lu, 2009). When one of these unwanted events occurs, energy is liberated destroying what is around it. Generally structures like buildings, tunnels, bridges, etc. are conceived to have the presence of big amount of people; if blasting loads reach these important structures, the catastrophic effects would be greater than those produced by the explosion itself, because the weakening of one part of the structure could lead to the entire collapse of it, causing lost of human lives and economic goods.

The present work consists in the dynamic analysis of circular slabs subjected to blast loads. This work aims at the construction of pressure-impulse diagrams for several types of blast loading patterns. In order to obtain these diagrams is necessary to assess the maximum resistance of slabs through a dynamic simulation of their behaviour. Blast loads vary with time and their main parameters are pressure and impulse, therefore it is needed a dynamic analysis.

This work concerns in the theoretical treatment of two cases: the first one consists in a simply supported circular slab and the second one corresponds to a circular slab on grade, where the grade is modelled as a Winkler soil. Each case is analysed for two types of material: reinforced concrete (R/C) and fibre reinforced concrete (FRC). The use of these materials has a great connotation because most of the slab or shell structures are designed and built with these types of material.

Many authors have already tackled the issue of concrete pavement slabs subjected to blast loading (Luccioni and Luege, 2006; Zhou et al., 2008), whilst several others concentrated on the internal explosion of box-type buried structures (Ma et al., 2009; Park and Krauthammer, 2009; Feldgun et al., 2008; Wang and Tan, 1995), thus giving special attention to the soil-structure interaction aspect of the problem.

Pressure-impulse diagrams are very useful in the practical-design field, since they represent a powerful tool that allows to assess directly, in a graphical way, the resistance of a structural element subjected to a determinate type of explosive event. We are talking about a wide field of applications; e.g., tunnel design, foundations, elevated slabs and plates can take advantage of this work in order to improve designs, maintenance and control of structures. Concerns in blast-resistant design by means of pressure-impulse diagrams have been tackled by Alaoui and Oswald (2007) considering precast and prestressed structures; El-Dakhakhni et al. (2009) focused on the capacity assessment of RC columns subjected to blast; Lan et al. (2005) and Li et al. (2009) studied composite structural elements subjected to explosive loadings, whilst Lan et al. (2005) considered fibre reinforced plastic slabs tackling the problem of the retrofitting of blast damaged structures.

Moreover, the results of this work could be compared with the results obtained from experimental test (e.g., from the shock tube tests). The shock tube test is specifically created to simulate accurately the shock pressure produced by an explosion. The shock tube test is intended to evaluate the maximum resistance of circular plates made of different materials and under several boundary conditions.

Thesis outline

The present work is organized in the following way. In the first chapter a quick outline of the main concepts about blasting phenomena will be presented. In chapter 2 the fundamentals of the elastic theory of plates will be reviewed. Chapter 3 will tackle the problem of the vibration of plates, focusing on the variational approach, the virtual work theorem and the numerical solutions, including also a short review of the upper bound theorem from the theory of plasticity. In chapter 4 the basic concepts about pressure-impulse diagrams will be presented, giving special attention to the algorithms used in the present work for their development. All the first four chapters will tackle the problems of interest from a pure theoretical point of view. In addition to the theoretical concepts, in chapter 5 some applicative examples will be solved and discussed, developing the theory presented in the previous chapters. The cases under study will be represented by a simply supported circular plate and a circular slab on grade.

Chapter 1

Blasting phenomena

1.1 Generalities

In spite of explosion events occurred due to several reasons, the engineering profession in general is not well tended to design structures able to resist under explosive loading. This happens because specifications have rarely included explosive loading as a factor in design, and also because dynamic effects of explosions on structures have only been examined as research subjects in a small number of experimental test (Lu, 2009; Gong et al., 2009; Ishikawa and Beppu, 2007; Li et al., 2009).

Actually in many countries the experimental research has been left to the armed service, government or larger industrial explosive manufacturers. Very often, the results are not openly reported due to security restrictions. However, there are several useful texts on the physics of explosions, the science of detonation and the design of protective structures. Unfortunately, these were not well collected or did not show a specific examination of the fundamentals and did not present parameters and coefficients that could influence future design and research.

1.2 Detonation and shock in free air

Detonation propagates as a wave through gas in a very similar way to the propagation of a shock wave through air (Bulson, 1997). This similitude was inspired by earlier work on the theory of sound and sound waves by Earnshaw (1860) and Lamb (1895). The publication of their works on the motion of fluids coincided with the beginning of the interest in explosions.

The most useful analysis of the detonation process was set down by G. I. Taylor in a paper written for the UK Civil Defence Research Committee, Ministry of Home Security, in 1941, during the Second World War (Bulson, 1997). He took a cylindrical bomb, in which the charge was detonated from one end and the reaction might advance along the length of the bomb at a speed of over 600 m/sec if the charge were TNT. The internal pressure forces the casing to expand, the expansion being greatest at the initiating end. When the casing breaks, the explosive gases escape and form an incandescent zone that expands so rapidly that a shock wave or pressure pulse is formed.

The dynamic loading of structures from detonating explosions is due to the instantaneous or very fast increase in air pressure associated with the shock front, and to the transient forces associated with the blast winds that follow the passage of the shock front.

1.3 Pressure-time function

The form of the overpressure-duration relationship for a high explosive or nuclear explosion in air is shown in figure 1.1, where p is overpressure (or air blast pressure) and t is time. In the figure the decay of pressure after the first instantaneous rise is expressed exponentially. There are other ways to indicate the form of the pressure-time relationship, as it will be shown later.
The value of the peak instantaneous overpressure p_0 will depend on the distance of the point of measurement from the centre of the explosion. The duration of the positive phase is t_0 units of time.
Theoretically, for a perfectly spherical charge in air, the relationship between p_0, the distance of the point of measurement from the centre of the explosion (R), and the instantaneous energy release (E), takes the form:

$$p_0 = \frac{K\,E}{R^3} \tag{1.1}$$

In imperial units E is measured in ft·lb, and in SI units in joules; $K = p_0 \cdot R^3/E$ is a non-dimensional parameter.

For a given type of chemical high explosive, energy is proportional to total weight, then equation 1.2 changes for design purposes as:

$$p_0 = \frac{K_1\,W}{R^3} \tag{1.2}$$

where K_1 is a dimensional parameter.

Some other pressure-time functions, like an improved version that was proposed in the US Army Technical Manual *Fundamentals of Protective Design (Non-nuclear)*, argue that the previous equation did not give very accurate values of p_0 over the entire time range. Therefore it was proposed a new function:

$$p_0 = \frac{4120}{z^3} - \frac{105}{z^2} + \frac{39.5}{z} \tag{1.3}$$

where p_0 is the peak pressure in psi and $z = R/W^{1/3}$ (with R in feet and W in lb), with W being the equivalent weight of charge in TNT. The relationship should only be applied when $2 < p_0 < 160$ psi, and $3 < R/W^{1/3} < 20$ ft/lb$^{1/3}$.

The pressure-distance characteristics discussed above only apply to a truly spherical charge in air, but in many practical circumstances the shape of the charge is cylindrical, or a plane sheet, or a line source such as detonating cord. Figure 1.2 illustrates the dependency of the pressure with the distance for different kind of charge shapes.
So far it was discussed mainly the free field conditions that result from many types of explosion, anyway it is interesting to notice that the propagation of air blast through closed structures, like systems of tunnels, can change. Figure 1.3, taken from Philip (1944), can illustrate this behaviour for a straight tunnel.

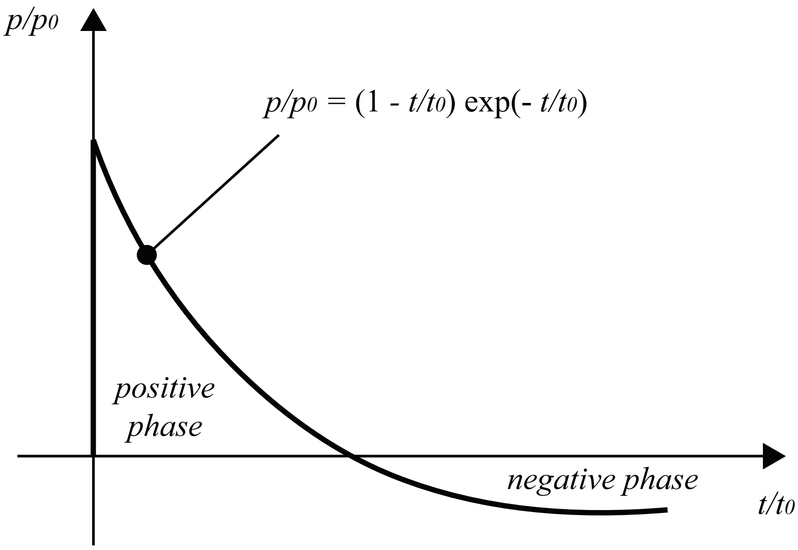

Figure 1.1: Overpressure-duration curve for detonation in air (idealization with exponential decay).

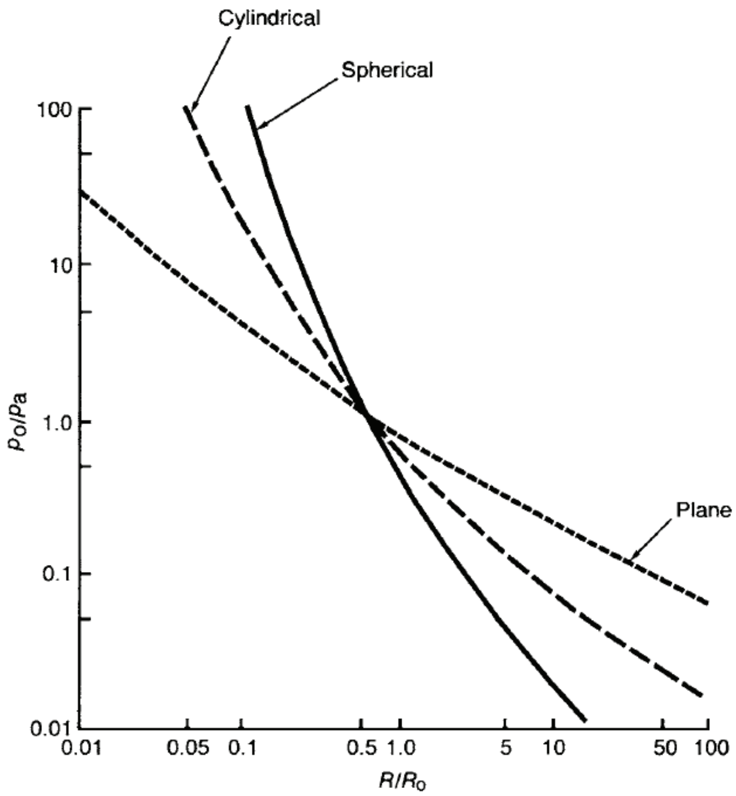

Figure 1.2: Peak overpressure vs range for various charge shapes (Lindberg and Firth, 1967).

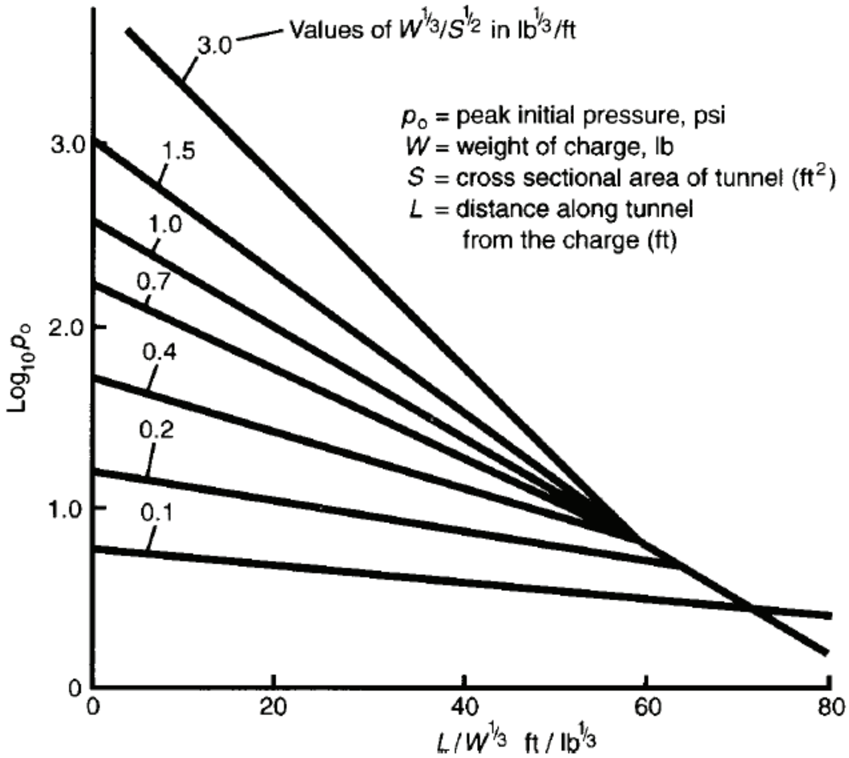

Figure 1.3: Peak pressure from a charge exploding inside a tunnel (Philip, 1944).

1.4 The shock tube

The shock tube is intended to simulate a scenario in which a spread pressure shocks against a representative structure sample (figure 1.4). The shock tube diameter depends on the specimen dimensions. In the case of tunnels, a portion of a lining segment will be represented as a circular slab in the shock tube test. Circular slabs represents very well the tunnel segment as long as the tunnel curvature is small. It is not practical having shock tube diameters as big as tunnel segments, that is why the real tunnel dimensions are scaled, for instance with factor of 1:3 (Colombo et al., 2010).
The shock tube consists of two rigid cylindrical chambers of equal cross section, named high pressure and low pressure chamber, respectively, which are separated by a diaphragm. The gas contained in the high pressure chamber (driver) causes the diaphragm rupture, leading to a rapid expansion of gas trough the low pressure chamber (driven). The result of this experience is a shock wave propagation along the driven section. When shock and expansion waves reach the close ends they are reflected and start moving toward the center of the shock tube, interacting at the same time with the induced flow (Colombo et al., 2010).

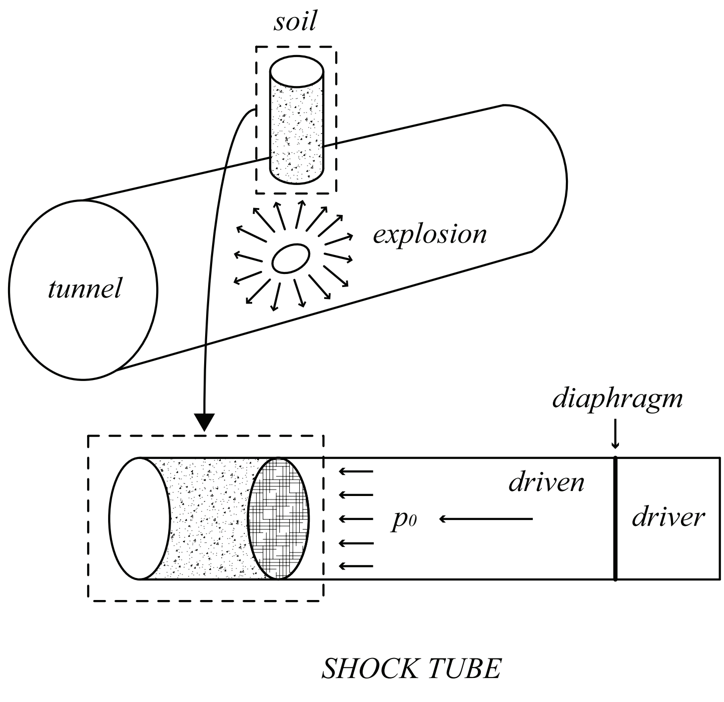

Figure 1.4: Sketch of an underground tunnel explosion and corresponding experimental test (Colombo et al., 2010).

Chapter 2

Elastic theory of plates

In this chapter the elastic theory of plates will be reviewed following different authors, amongst the others Timoshenko and Woinowsky-Krieger (1959), Belluzzi (1966), Selvadurai (1979), Ventsel and Krauthammer (2001), Corigliano and Taliercio (2005). Along this chapter, the elastic theory of plates is explained starting from the general theory, passing through rectangular plates and finishing with the theory of thin plates. All this process describes how to derive the elastic equations for circular thin plates. These equations are achieved via a transformation of the reference system from rectangular to polar coordinates. The axial symmetry of circular plates simplifies the problem to one spatial variable r, thus making the dynamic analysis more manageable.

2.1 The plate model

Let's now consider a generic plate element as shown in figure 2.1. The plate model can be viewed as a bidimensional extension of the beam model. The basic idea is to analyse the plate deformation by studying the deformation of its middle plane. In this way, the state of deformation will be associated to the loads acting in the middle plane of the plate. As in the beam model the beam deformation is analyse by studying its axis, analogously herein the plate deformation is analysed by referring to its middle plane.

The displacement in the vertical direction z is defined as $w \equiv w(x, y)$, i.e., it is function of x and y, but not of z.

The hypotheses made in order to develop the plate model are the following ones:

- small displacements and small deformations;
- homogeneous, isotropic, Green iper-elastic material (i.e. there exists a potential function by which stresses and strains can be represented);
- the medium is a Cauchy continuum (that is, the stress-state tensor is symmetric, and there are no distributed microcouples);
- two geometrical dimensions are prevalent with respect to the third one;
- $\sigma_z = 0$, hypothesis that does not allow to represent the state of stress diffusivity.

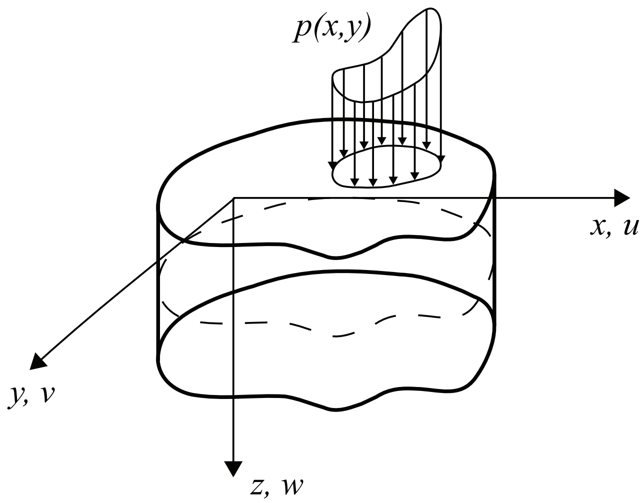

Figure 2.1: A generic plate element with the reference system located in its middle plane.

The kinematic model of the deflected plate assumes that a generic straight segment, initially perpendicular to the middle plane (see figure 2.2), after the deformation it is still straight. Not necessarily, after the deformation, the generic straight segment is still perpendicular to the deformed mid plane, as shown in figure 2.3.
Within this discussion the focus will be on the flexural behaviour of plates, thus only forces acting perpendicularly to the middle plane will be considered, decoupling the flexural problem from the one related to the forces acting parallel to the middle plane (membrane theory).

Displacement components. The local displacement vector is represented by:

$$\underline{s}(x,y,z) = \begin{bmatrix} u \\ v \\ w \end{bmatrix} = \begin{bmatrix} -z\varphi_x(x,y) \\ -z\varphi_y(x,y) \\ w(x,y) \end{bmatrix} \tag{2.1}$$

where:

- u is the displacement component in the x direction;
- v is the displacement component in the y direction;
- w is the displacement component in the z direction.

and $\varphi_x(x,y)$, $\varphi_y(x,y)$ and $w(x,y)$ are the generalized displacements:

- $\varphi_x(x,y)$ is the rotation around the y axis occurring in the x-z plane;
- $\varphi_y(x,y)$ is the rotation around the x axis occurring in the y-z plane;
- $w(x,y)$ is the middle plane displacement in the vertical direction z.

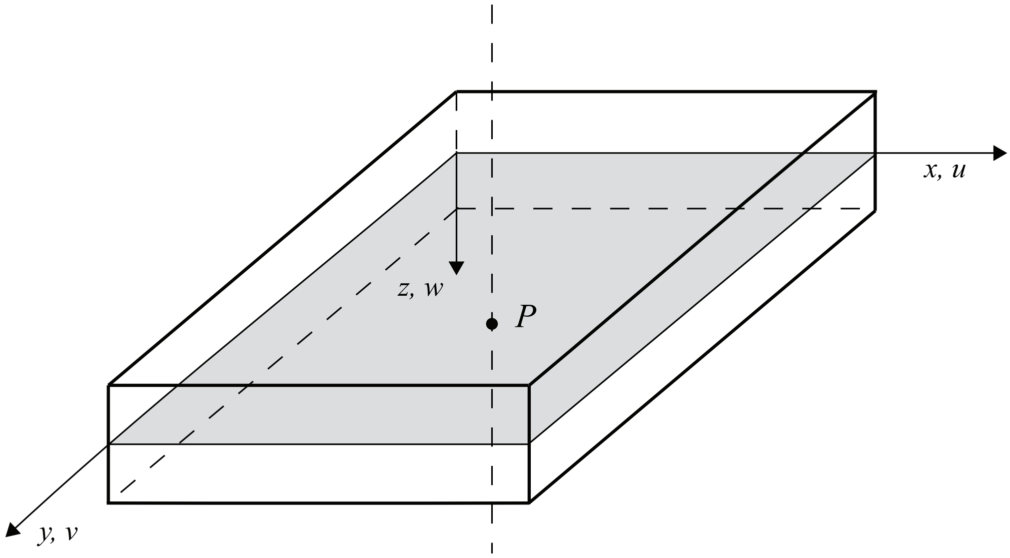

Figure 2.2: A generic point on the generic straight segment initially orthogonal to the plate middle plane.

The displacement vector can be rewritten as:

$$\underline{s} = \underline{\underline{n}} \cdot \underline{U} \tag{2.2}$$

where $\underline{U}$ is the vector of generalized displacements:

$$\underline{U} = \begin{bmatrix} w(x,y) \\ \varphi_x(x,y) \\ \varphi_y(x,y) \end{bmatrix} \tag{2.3}$$

and $\underline{\underline{n}}$ is the correlation matrix between local displacements and generalized ones:

$$\underline{\underline{n}} = \begin{bmatrix} 0 & -z & 0 \\ 0 & 0 & -z \\ 1 & 0 & 0 \end{bmatrix} \tag{2.4}$$

Strain components. The strain components can be worked out by means of the compatibility equations:

$$\underline{\varepsilon} = \begin{bmatrix} \varepsilon_x \\ \varepsilon_y \\ \varepsilon_z \\ \gamma_{xy} \\ \gamma_{xz} \\ \gamma_{yz} \end{bmatrix} = \begin{bmatrix} u_{,x} \\ v_{,y} \\ w_{,z} \\ u_{,y} + v_{,x} \\ u_{,z} + w_{,x} \\ w_{,y} + v_{,z} \end{bmatrix} = \begin{bmatrix} -z\varphi_{x,x} \\ -z\varphi_{y,y} \\ 0 \\ -z\varphi_{x,y} - z\varphi_{y,x} \\ -\varphi_x + w_{,x} \\ -\varphi_y + w_{,y} \end{bmatrix} = \underline{\underline{b}} \cdot \underline{q} \tag{2.5}$$

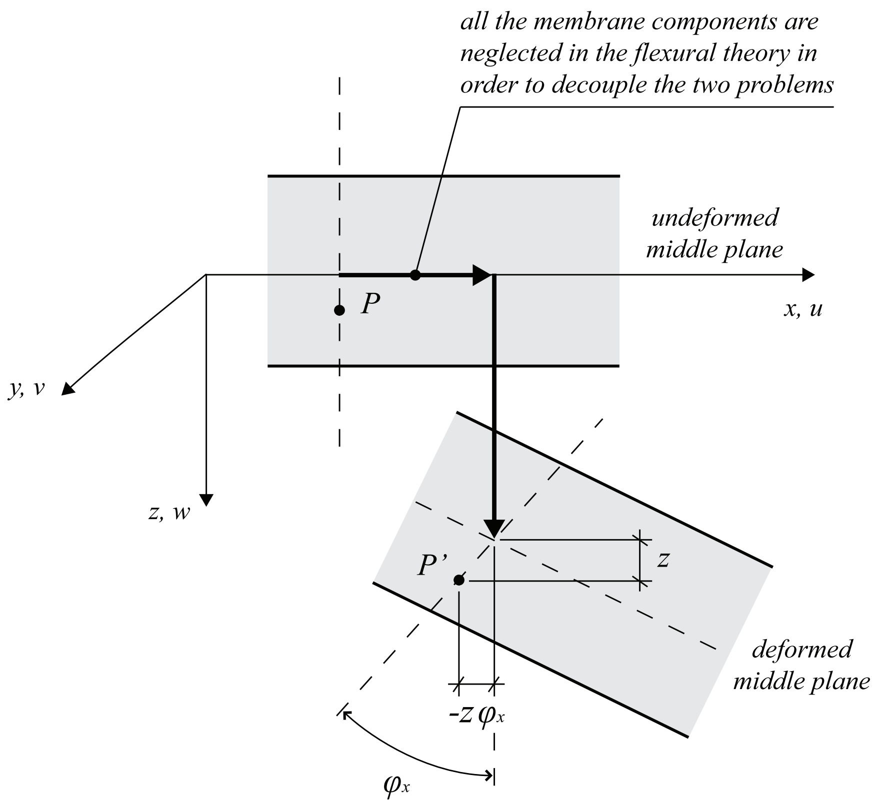

Figure 2.3: A section of a plate, traced in the x-z plane, before and after the deformation.

where $\underline{q}$ is the vector of generalized strains and $\underline{\underline{b}}$ is the correlation matrix between local strains and generalized ones.

$$\underline{q} = \begin{bmatrix} -\varphi_{x,x} \\ -\varphi_{y,y} \\ -(\varphi_{x,y} + \varphi_{y,x}) \\ -\varphi_x + w_{,x} \\ -\varphi_y + w_{,y} \end{bmatrix} = \begin{bmatrix} \chi_x \\ \chi_y \\ \chi_{xy} \\ t_x \\ t_y \end{bmatrix} \tag{2.6}$$

The terms denoted with χ are the generalized curvatures; in particular, χ_{xy} is the torsional curvature. The terms t_x and t_y represent the shear angular deformations.

$$\underline{\underline{b}} = \begin{bmatrix} z & 0 & 0 & 0 & 0 \\ 0 & z & 0 & 0 & 0 \\ 0 & 0 & z & 0 & 0 \\ 0 & 0 & 0 & 1 & 0 \\ 0 & 0 & 0 & 0 & 1 \end{bmatrix} \tag{2.7}$$

Load components. The generalized loads will be worked out by using the definition of external specific work per unit area.

$$\underline{F} = \begin{bmatrix} F_x \\ F_y \\ F_z \end{bmatrix} \tag{2.8}$$

The external specific work per unit area is given by:

$$\frac{\mathrm{d}W_E}{\mathrm{d}A} = \int_{-h/2}^{+h/2} F_i \delta\widehat{s}_i \,\mathrm{d}z = \underline{P}^T \delta\underline{\widehat{U}} = \int_{-h/2}^{+h/2} \delta\underline{\widehat{s}}^T \underline{F} \,\mathrm{d}z \tag{2.9}$$

where:

- $\delta\widehat{s}_i$ is the virtual displacement field;
- $\underline{P}$ is the vector of the generalized loads.

$$\frac{\mathrm{d}W_E}{\mathrm{d}A} = \delta\underline{\widehat{U}}^T \int_{-h/2}^{+h/2} \underline{\underline{n}}^T \cdot \underline{F} \,\mathrm{d}z = \underline{P}^T \delta\underline{\widehat{U}} = \delta\underline{\widehat{U}}^T \cdot \underline{P} \tag{2.10}$$

From the last equation one can read the expression that give rise to the generalized loads:

$$\underline{P} = \int_{-h/2}^{+h/2} \underline{\underline{n}}^T \cdot \underline{F} \,\mathrm{d}z \tag{2.11}$$

Substituting the expressions for $\underline{\underline{n}}$ and $\underline{F}$ one can get:

$$\underline{P} = \int_{-h/2}^{+h/2} \begin{bmatrix} 0 & 0 & 1 \\ -z & 0 & 0 \\ 0 & -z & 0 \end{bmatrix} \cdot \begin{bmatrix} F_x \\ F_y \\ F_z \end{bmatrix} \mathrm{d}z \tag{2.12}$$

$$= \int_{-h/2}^{+h/2} \begin{bmatrix} F_z \\ -zF_x \\ -zF_y \end{bmatrix} \mathrm{d}z \tag{2.13}$$

$$= \begin{bmatrix} p(x,y) \\ m_x(x,y) \\ m_y(x,y) \end{bmatrix} \tag{2.14}$$

Note that $p(x,y)$ is dimensionally a force per unit area (i.e., a surface distributed load, [F/L^2]), whilst $m_x(x,y)$ and $m_y(x,y)$ are moments per unit length (i.e., they have the dimension of a force, [F]).
It should be noted that there is no explicit information about the points where the generalized loads are acting; it is only the assumption made by the model that permits to tell that they act in the middle plane of the plate, as shown in figure 2.4.

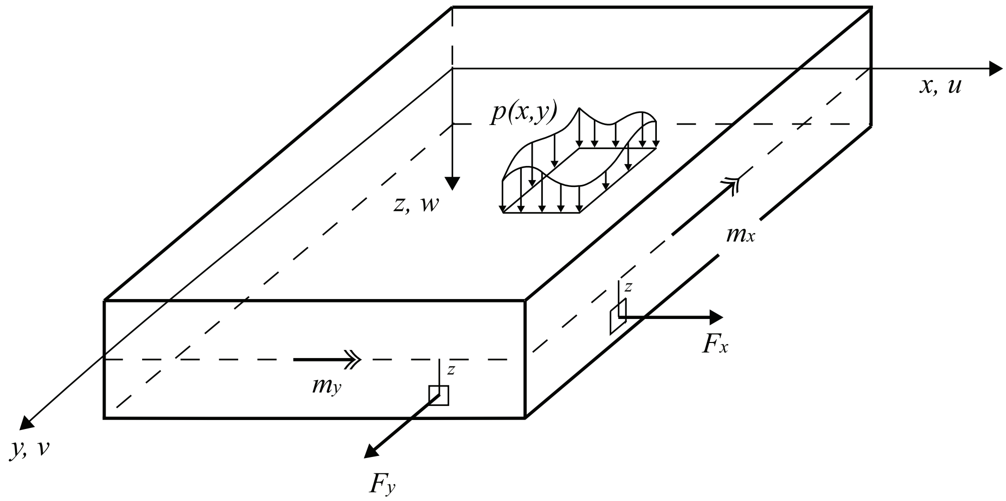

Figure 2.4: Generalized loads acting on a rectangular plate element.

Stress components. In order to work out the generalized stresses, the definition of internal specific work per unit area will be exploited:

$$\frac{\mathrm{d}W_I}{\mathrm{d}A} = \int_{-h/2}^{+h/2} \delta\underline{\hat{\varepsilon}}^T \cdot \underline{\sigma}\,\mathrm{d}z = \delta\underline{q}^T \int_{-h/2}^{+h/2} \underline{\underline{b}} \cdot \underline{\sigma}\,\mathrm{d}z = \delta\underline{q}^T \cdot \underline{Q} \tag{2.15}$$

where:

- $\delta\underline{\hat{\varepsilon}}$ are the virtual local strains;
- $\underline{\sigma}$ are the local stresses;
- $\underline{Q}$ is the vector containing the generalized stresses.

The local deformations are related to the generalized ones by means of the correlation matrix $\underline{\underline{b}}$:

$$\underline{\varepsilon} = \underline{\underline{b}} \cdot \underline{q} \tag{2.16}$$

The expression needed in order to work out the vector of the generalized stresses can be easily read from equation 2.15:

$$\underline{Q} = \int_{-h/2}^{+h/2} \underline{\underline{b}} \cdot \underline{\sigma}\,\mathrm{d}z \tag{2.17}$$

Performing the computations one can finally obtained:

$$\underline{Q} = \int_{-h/2}^{+h/2} \begin{bmatrix} z & 0 & 0 & 0 & 0 \\ 0 & z & 0 & 0 & 0 \\ 0 & 0 & z & 0 & 0 \\ 0 & 0 & 0 & 1 & 0 \\ 0 & 0 & 0 & 0 & 1 \end{bmatrix} \cdot \begin{bmatrix} \sigma_x \\ \sigma_y \\ \tau_{xy} \\ \tau_{xz} \\ \tau_{yz} \end{bmatrix} \mathrm{d}z \tag{2.18}$$

$$= \begin{bmatrix} \int_{-h/2}^{+h/2} z\sigma_x \,\mathrm{d}z \\ \int_{-h/2}^{+h/2} z\sigma_y \,\mathrm{d}z \\ \int_{-h/2}^{+h/2} z\tau_{xy} \,\mathrm{d}z \\ \int_{-h/2}^{+h/2} \tau_{xz} \,\mathrm{d}z \\ \int_{-h/2}^{+h/2} \tau_{yz} \,\mathrm{d}z \end{bmatrix} = \begin{bmatrix} M_x \\ M_y \\ M_{xy} \\ V_x \\ V_y \end{bmatrix} \tag{2.19}$$

where σ_x and σ_y are the normal stresses, whilst τ_{xy}, τ_{xz} and τ_{yz} are the tangential stresses. The distance of the point of application of such stresses from the middle plane is denoted as z, as can be seen in figure 2.5.
The generalized moments M_x, M_y and M_{xy} have the dimension of a force (i.e., they are moments per unit length, [F]), whilst the shear terms V_x and V_y have the dimensions of a force per unit length, i.e. [F/L].
All the local and generalized stresses, along with the directions in which they are acting, are graphically illustrated in figure 2.5. The moments are represented as vectors; z represents the stresses lever arm with respect to the middle plane.

2.2 Plate equilibrium problem

There are three different ways to study the problem of the plate equilibrium:

- by using the virtual work principle;
- by using the integrated equilibrium equations;
- by studying the equilibrium of a plate element.

In this section, the problem of the plate equilibrium will be studied by means of a rectangular plate element, as illustrated in figure 2.5.

Rotational equilibrium with respect to x axis.

$$V_y' \,\mathrm{d}x\mathrm{d}y - M_y' \,\mathrm{d}x + M_y \,\mathrm{d}x + M_{xy}' \,\mathrm{d}y + M_{xy} \,\mathrm{d}y + p(x,y) \,\mathrm{d}x \,\mathrm{d}y \,\frac{\mathrm{d}y}{2} + m_y \,\mathrm{d}x \,\mathrm{d}y = 0 \tag{2.20}$$

The term $p(x,y)\,\mathrm{d}x\,\mathrm{d}y\,\dfrac{\mathrm{d}y}{2}$ is dropped out since it represents an infinitesimal of higher order.

$$\left(V_y + \frac{\partial V_y}{\partial y}\mathrm{d}y\right)\mathrm{d}x\,\mathrm{d}y - \left(M_y + \frac{\partial M_y}{\partial y}\mathrm{d}y\right)\mathrm{d}x + M_y\,\mathrm{d}x - \left(M_{xy} + \frac{\partial M_{xy}}{\partial x}\mathrm{d}x\right)\mathrm{d}y + M_{xy}\,\mathrm{d}y + m_y\,\mathrm{d}x\,\mathrm{d}y = 0 \tag{2.21}$$

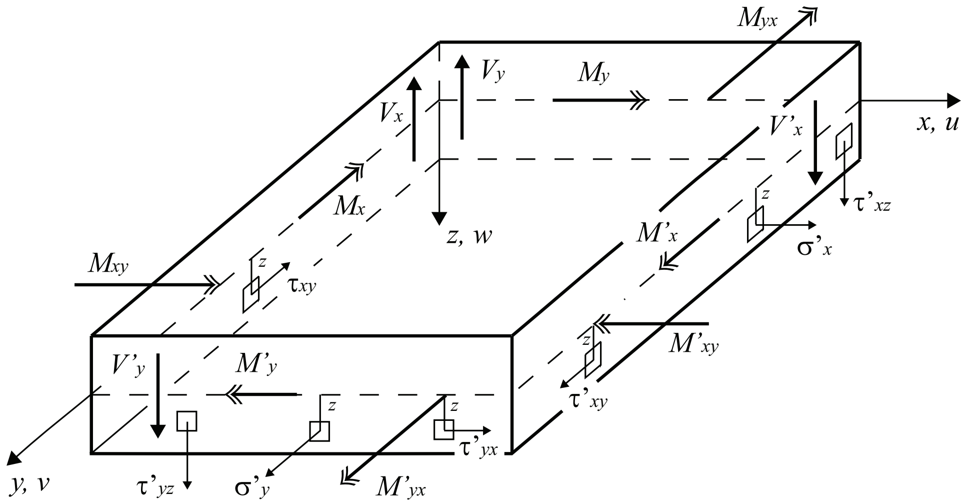

Figure 2.5: Equilibrium of a rectangular plate element.

$$V_y - \frac{\partial M_y}{\partial y} - \frac{\partial M_{xy}}{\partial x} + m_y = 0 \tag{2.22}$$

Finally:

$$V_y = \frac{\partial M_y}{\partial y} + \frac{\partial M_{xy}}{\partial x} - m_y \tag{2.23}$$

Rotational equilibrium with respect to y axis.

$$V'_x \,\mathrm{d}y\mathrm{d}x - M'_x \,\mathrm{d}y + M_x \,\mathrm{d}y - M'_{yx} \,\mathrm{d}x + M_{yx} \,\mathrm{d}x + p(x,y) \,\mathrm{d}x \,\mathrm{d}y \,\frac{\mathrm{d}x}{2} + m_x \,\mathrm{d}y \,\mathrm{d}x = 0 \tag{2.24}$$

The term $p(x,y) \,\mathrm{d}x \,\mathrm{d}y \,\frac{\mathrm{d}x}{2}$ is dropped out since it represents an infinitesimal of higher order.

$$\left(V_x + \frac{\partial V_x}{\partial x} \mathrm{d}x\right) \mathrm{d}y \,\mathrm{d}x - \left(M_x + \frac{\partial M_x}{\partial x} \, dx\right) dy + M_x \, dy$$
$$- \left(M_{yx} + \frac{\partial M_{yx}}{\partial y} \mathrm{d}y\right) \mathrm{d}x + M_{yx} \,\mathrm{d}x + m_x \,\mathrm{d}y \,\mathrm{d}x = 0 \tag{2.25}$$

$$V_x - \frac{\partial M_x}{\partial x} - \frac{\partial M_{yx}}{\partial y} + m_x = 0 \tag{2.26}$$

Finally:

$$V_x = \frac{\partial M_x}{\partial x} + \frac{\partial M_{yx}}{\partial y} - m_x \tag{2.27}$$

Translational equilibrium.

$$\frac{\partial V_x}{\partial x} \,\mathrm{d}x \,\mathrm{d}y + \frac{\partial V_y}{\partial y} \,\mathrm{d}y \,\mathrm{d}x + p(x,y) \,\mathrm{d}x \,\mathrm{d}y = 0 \tag{2.28}$$

$$\frac{\partial V_x}{\partial x} + \frac{\partial V_y}{\partial y} + p(x,y) = 0 \tag{2.29}$$

Plate equilibrium equation. Substituting equations 2.23 and 2.27 into equation 2.29 one can work out the equilibrium equation of the rectangular plate element:

$$\frac{\partial^2 M_x}{\partial x^2} + 2\frac{\partial^2 M_{xy}}{\partial x \partial y} + \frac{\partial^2 M_y}{\partial y^2} + p(x,y) - \frac{\partial m_y}{\partial y} - \frac{\partial m_x}{\partial x} = 0 \tag{2.30}$$

Generalized constitutive relationship. In order to develop the generalized constitutive relationship, the definition of elastic specific energy per unit area will be exploited. Recalling the local constitutive relationship $\underline{\sigma} = \underline{\underline{D}}\,\underline{\varepsilon}$, where $\underline{\underline{D}}$ is the stiffness matrix:

$$\underline{\underline{D}} = \frac{E}{1-\nu^2}\begin{bmatrix} 1 & \nu & 0 & 0 & 0 \\ \nu & 1 & 0 & 0 & 0 \\ 0 & 0 & \dfrac{1-\nu}{2} & 0 & 0 \\ 0 & 0 & 0 & \dfrac{1-\nu}{2} & 0 \\ 0 & 0 & 0 & 0 & \dfrac{1-\nu}{2} \end{bmatrix} \tag{2.31}$$

one can write down the elastic specific energy per unit area:

$$\frac{\mathrm{d}\Omega}{\mathrm{d}A} = \frac{1}{2}\int_{-h/2}^{+h/2} \underline{\varepsilon}^T \cdot \underline{\sigma}\,\mathrm{d}z = \frac{1}{2}\underline{q}^T \int_{-h/2}^{+h/2} \underline{\underline{b}}^T \cdot \underline{\underline{D}} \cdot \underline{\underline{b}}\,\mathrm{d}z\,\underline{q} = \frac{1}{2}\underline{q}^T \cdot \underline{\underline{D}}^* \cdot \underline{q} \tag{2.32}$$

From the last expression it is clear that the generalized stiffness matrix $\underline{\underline{D}}^*$ is equal to:

$$\underline{\underline{D}}^* = \int_{-h/2}^{+h/2} \underline{\underline{b}}^T \cdot \underline{\underline{D}} \cdot \underline{\underline{b}}\,\mathrm{d}z \tag{2.33}$$

$$= \int_{-h/2}^{+h/2} \begin{bmatrix} z & 0 & 0 & 0 & 0 \\ 0 & z & 0 & 0 & 0 \\ 0 & 0 & z & 0 & 0 \\ 0 & 0 & 0 & 1 & 0 \\ 0 & 0 & 0 & 0 & 1 \end{bmatrix} \cdot \frac{E}{1-\nu^2}\begin{bmatrix} 1 & \nu & 0 & 0 & 0 \\ \nu & 1 & 0 & 0 & 0 \\ 0 & 0 & \dfrac{1-\nu}{2} & 0 & 0 \\ 0 & 0 & 0 & \dfrac{1-\nu}{2} & 0 \\ 0 & 0 & 0 & 0 & \dfrac{1-\nu}{2} \end{bmatrix} \cdot \begin{bmatrix} z & 0 & 0 & 0 & 0 \\ 0 & z & 0 & 0 & 0 \\ 0 & 0 & z & 0 & 0 \\ 0 & 0 & 0 & 1 & 0 \\ 0 & 0 & 0 & 0 & 1 \end{bmatrix} \mathrm{d}z \tag{2.34}$$

Remembering that the moment of inertia of a unit length element is given by:

$$\int_{-h/2}^{+h/2} 1 \cdot z^2\,\mathrm{d}z = I \tag{2.35}$$

one can finally work out $\underline{\underline{D}}^*$ as follows:

$$\underline{\underline{D}}^* = \frac{EI}{1-\nu^2}\begin{bmatrix} 1 & \nu & 0 & 0 & 0 \\ \nu & 1 & 0 & 0 & 0 \\ 0 & 0 & \dfrac{1-\nu}{2} & 0 & 0 \\ 0 & 0 & 0 & \left(\dfrac{1-\nu}{2I}\right)h & 0 \\ 0 & 0 & 0 & 0 & \left(\dfrac{1-\nu}{2I}\right)h \end{bmatrix} \tag{2.36}$$

The generalized stiffness matrix $\underline{\underline{D}}^*$ just obtained relates the generalized stresses $\underline{Q}$ to the generalized strains $\underline{q}$:

$$\underline{Q} = \underline{\underline{D}}^* \cdot \underline{q} \tag{2.37}$$

where $\underline{Q}$ and $\underline{q}$ are the vectors:

$$\underline{q} = \begin{bmatrix} \chi_x \\ \chi_y \\ \chi_{xy} \\ t_x \\ t_y \end{bmatrix} \tag{2.38}$$

$$\underline{Q} = \begin{bmatrix} M_x \\ M_y \\ M_{xy} \\ V_x \\ V_y \end{bmatrix} \tag{2.39}$$

Equation 2.37 can be rewritten in expanded form, giving rise to the following relationships:

$$M_x = D(\chi_x + \nu\chi_y) \tag{2.40}$$

$$M_y = D(\chi_y + \nu\chi_x) \tag{2.41}$$

$$M_{xy} = D\frac{1-\nu}{2}\chi_{xy} = \frac{EI}{1-\nu^2}\frac{1-\nu}{2}\chi_{xy} = \frac{EI}{2(1+\nu)}\chi_{xy} = GI\chi_{xy} \tag{2.42}$$

$$V_x = G\,h\,t_x \tag{2.43}$$

$$V_y = G\,h\,t_y \tag{2.44}$$

where:

- $D = \dfrac{EI}{1-\nu^2}$ is the flexural rigidity factor, which includes all the elastic constants related to material;
- $G = \dfrac{E}{2(1+\nu)}$ is the shear modulus;
- $I = \dfrac{1 \cdot h^3}{12}$ is the moment of inertia of a unit length element.

2.3 Thin plates theory

If a plate is thin enough with respect to its height, it is possible to neglect the shear deformations. Usually it is considered that a plate falls into this hypothesis field if $h < \min(a, b)/5$, where h is the thickness, a and b are the other two dimensions. Furthermore, also the condition that the maximum displacement of the plate must be smaller than 1/5 of the thickness should be satisfied (Belluzzi, 1966). If the previous conditions are met, then the generic straight segment initially perpendicular to the middle plane remains perpendicular to it even after the deformation. This removes the possibility of having angular (i.e., shear) deformations. This hypothesis was first studied by Kirchhoff and it is usually named after him (Timoshenko and Woinowsky-Krieger, 1959). The Kirchhoff's hypothesis can be represented by the following mathematical condition:

$$\gamma_{xz} = \gamma_{yz} = 0 \tag{2.45}$$

which implies (see equation 2.6):

$$\varphi_x = \frac{\partial w}{\partial x} \qquad \varphi_y = \frac{\partial w}{\partial y} \tag{2.46}$$

Now it is clear from the previous expressions that, under the Kirchhoff's hypothesis, the rotation of the generic straight segment is exactly equal to the one of the middle plane, meaning that there are no angular deformations. Therefore the plate model can be reformulated in this simplified case, obtaining the expressions reported below.
Local displacement vector:

$$\underline{s} = \begin{bmatrix} u \\ v \\ w \end{bmatrix} = \begin{bmatrix} -z\varphi_x \\ -z\varphi_y \\ w(x,y) \end{bmatrix} = \begin{bmatrix} -zw_{,x} \\ -zw_{,y} \\ w(x,y) \end{bmatrix} \tag{2.47}$$

Generalized displacement vector:

$$\underline{U} = \begin{bmatrix} w \\ w_{,x} \\ w_{,y} \end{bmatrix} \tag{2.48}$$

Generalized strain vector:

$$\underline{q} = \begin{bmatrix} \chi_x \\ \chi_y \\ \chi_{xy} \end{bmatrix} \tag{2.49}$$

Local strain vector:

$$\underline{\varepsilon} = \begin{bmatrix} \varepsilon_x \\ \varepsilon_y \\ \gamma_{xy} \end{bmatrix} = \begin{bmatrix} z\chi_x \\ z\chi_y \\ z\chi_{xy} \end{bmatrix} = \begin{bmatrix} -zw_{,xx} \\ -zw_{,yy} \\ -2zw_{,xy} \end{bmatrix} \tag{2.50}$$

The generalized constitutive relationships give rise to the following expressions:

$$M_x = D(\chi_x + \nu\chi_y) = -D\left(\frac{\partial^2 w}{\partial x^2} + \nu\frac{\partial^2 w}{\partial y^2}\right) \tag{2.51}$$

$$M_y = D(\chi_y + \nu\chi_x) = -D\left(\frac{\partial^2 w}{\partial y^2} + \nu\frac{\partial^2 w}{\partial x^2}\right) \tag{2.52}$$

$$M_{xy} = GI\chi_{xy} = -D(1-\nu)\left(\frac{\partial^2 w}{\partial x \partial y}\right) \tag{2.53}$$

Recalling the plate equilibrium equation 2.30 and neglecting the terms related to distributed microcouples:

$$\frac{\partial^2 M_x}{\partial x^2} + 2\frac{\partial^2 M_{xy}}{\partial x \partial y} + \frac{\partial^2 M_y}{\partial y^2} + p(x,y) = 0 \tag{2.54}$$

Substituting the equations 2.51, 2.52 and 2.53 into equation 2.54 one can get:

$$\frac{\partial^4 w}{\partial x^4} + 2\frac{\partial^4 w}{\partial x^2 \partial y^2} + \frac{\partial^4 w}{\partial y^4} = -\frac{p(x,y)}{D} \tag{2.55}$$

namely:

$$\nabla^4 w(x,y) = -\frac{p(x,y)}{D} \tag{2.56}$$

which is the Sophie Germain - Lagrange equation for thin plates (i.e., plates under the Kirchhoff hypothesis). It should be noticed that this equation includes in itself the equilibrium condition, the compatibility equation and the constitutive relationship. It appears as a generalization to the bidimensional case of the unidimensional Euler-Bernoulli equation for beams (Timoshenko and Woinowsky-Krieger, 1959).
In equation 2.56 appears the symbol ∇^4 which represents the Laplacian operator of fourth order. The Laplacian of a function allows to compare the function at a point with the function at neighbouring points (Farlow, 1993). The Laplacian of fourth order can be viewed as a generalization of the unidimensional fourth derivative to higher dimension.

2.3.1 Circular plates

Since in the present work only circular plates will be analysed, it is convenient to express the governing differential equation in polar coordinates, which can be easily achieved by performing a coordinate transformation. Figure 2.6 illustrate the equilibrium of a circular plate element.
The geometrical relationships between Cartesian and polar coordinates are:

$$x = r\cos\theta \qquad y = r\sin\theta \qquad r^2 = x^2 + y^2 \qquad \theta = \arctan\left(\frac{y}{x}\right) \tag{2.57}$$

$$\frac{\partial r}{\partial x} = \frac{\partial\sqrt{x^2+y^2}}{\partial x} = \frac{2x}{2\sqrt{x^2+y^2}} = \frac{x}{r} = \cos\theta \tag{2.58}$$

$$\frac{\partial r}{\partial y} = \frac{\partial\sqrt{x^2+y^2}}{\partial y} = \frac{2y}{2\sqrt{x^2+y^2}} = \frac{y}{r} = \sin\theta \tag{2.59}$$

$$\frac{\partial\theta}{\partial x} = \frac{\arctan\left(\frac{y}{x}\right)}{\partial x} = -\frac{\frac{y}{x^2}}{1+\left(\frac{y}{x}\right)^2} = -\frac{y}{r^2} = -\frac{\sin\theta}{r} \tag{2.60}$$

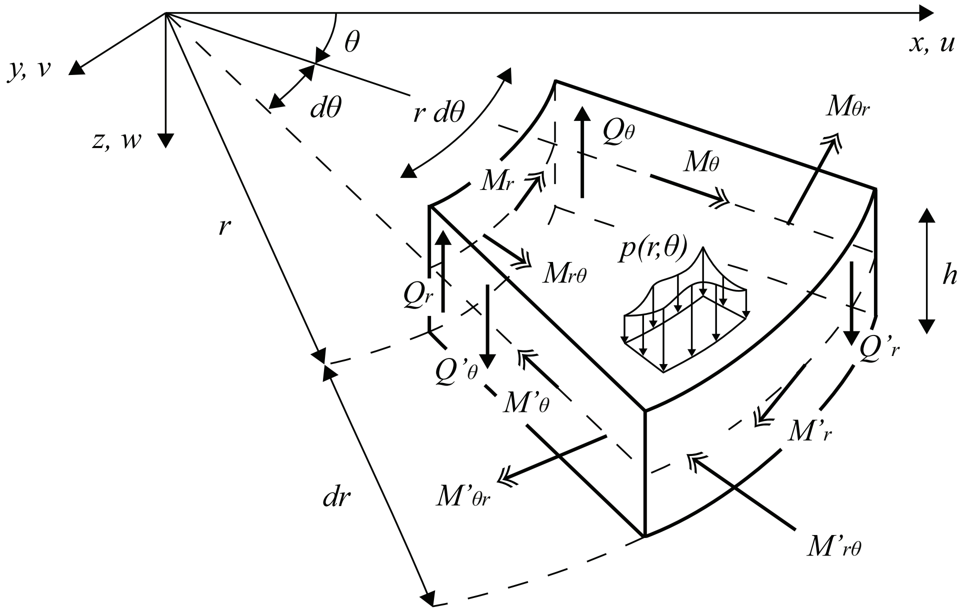

Figure 2.6: Equilibrium of a circular plate element.

$$\frac{\partial\theta}{\partial y} = \frac{\arctan\left(\frac{y}{x}\right)}{\partial y} = \frac{\frac{1}{x}}{1+\left(\frac{y}{x}\right)^2} = \frac{x}{r^2} = \frac{\cos\theta}{r} \tag{2.61}$$

Applying the chain rule:

$$\frac{\partial w}{\partial x} = \frac{\partial w}{\partial r}\frac{\partial r}{\partial x} + \frac{\partial w}{\partial \theta}\frac{\partial \theta}{\partial x} = \frac{\partial w}{\partial r}\cos\theta - \frac{1}{r}\frac{\partial w}{\partial \theta}\sin\theta \tag{2.62}$$

Now it should be noted that for an axis-symmetric problem, like all the ones that will be treated in the present work, holds:

$$\frac{\partial}{\partial\theta} = 0 \tag{2.63}$$

i.e., all the terms involving partial derivatives with respect to θ can be dropped out. Therefore the previous expression can be simplified:

$$\frac{\partial w}{\partial x} = \frac{\partial w}{\partial r}\frac{\partial r}{\partial x} = \frac{\partial w}{\partial r}\cos\theta \tag{2.64}$$

To evaluate the term $\partial^2 w/\partial x^2$ the previous operation must be repeated twice, obtaining:

$$\frac{\partial^2 w}{\partial x^2} = \frac{\partial^2 w}{\partial r^2}\cos^2\theta + \frac{\partial w}{\partial r}\frac{\sin^2\theta}{r} \tag{2.65}$$

Analogously:

$$\frac{\partial^2 w}{\partial y^2} = \frac{\partial^2 w}{\partial r^2}\sin^2\theta + \frac{\partial w}{\partial r}\frac{\cos^2\theta}{r} \tag{2.66}$$

$$\frac{\partial^2 w}{\partial x\partial y} = \frac{\partial^2 w}{\partial r^2}\frac{\sin 2\theta}{2} - \frac{\partial w}{\partial r}\frac{\sin 2\theta}{2r} \tag{2.67}$$

Adding term by term:

$$\nabla_r^2 w \equiv \frac{\partial^2 w}{\partial x^2} + \frac{\partial^2 w}{\partial y^2} = \frac{\partial^2 w}{\partial r^2} + \frac{1}{r}\frac{\partial w}{\partial r} \tag{2.68}$$

Repeating the operation twice, one can get the governing differential equation for axis-symmetric plates in polar coordinates:

$$\nabla_r^4 w(r,\theta) \equiv \left(\frac{\partial^2}{\partial r^2} + \frac{1}{r}\frac{\partial}{\partial r}\right)\left(\frac{\partial^2 w}{\partial r^2} + \frac{1}{r}\frac{\partial w}{\partial r}\right) = \frac{p(r,\theta)}{D} \tag{2.69}$$

Since the plate geometry is symmetric and also the load distribution will be assumed to be axis-symmetric throughout this work, the previous equation can be simply rewritten as:

$$\nabla_r^4 w(r) = \frac{p(r)}{D} \tag{2.70}$$

From the expressions outlined above the curvatures in polar coordinates can be worked out (assuming that x axis is taken in the direction of the radius r, at $\theta = 0$, in order to simplify the derivations):

$$\chi_x = \chi_r = -\frac{\partial^2 w}{\partial x^2} = -\frac{\partial^2 w}{\partial r^2} \tag{2.71}$$

$$\chi_y = \chi_\theta = -\frac{\partial^2 w}{\partial y^2} = -\frac{1}{r}\frac{\partial w}{\partial r} \tag{2.72}$$

$$\chi_{xy} = \chi_{r\theta} = -\frac{\partial^2 w}{\partial x \partial y} = 0 \tag{2.73}$$

Now the relationships between moment and curvatures:

$$M_r = M_x = D(\chi_x + \nu\chi_y) = -D\left(\frac{\partial^2 w}{\partial r^2} + \nu\frac{1}{r}\frac{\partial w}{\partial r}\right) \tag{2.74}$$

$$M_\theta = M_y = D(\chi_y + \nu\chi_x) = -D\left(\frac{1}{r}\frac{\partial w}{\partial r} + \nu\frac{\partial^2 w}{\partial r^2}\right) \tag{2.75}$$

$$M_{r\theta} = M_{xy} = D(1-\nu)\chi_{xy} = 0 \tag{2.76}$$

Elastic strain energy computation:

$$\begin{aligned}
U &= \frac{1}{2}\iint_S (M_x\chi_x + M_y\chi_y + 2M_{xy}\chi_{xy})\,\mathrm{d}S && (2.77)\\
&= \frac{1}{2}\iint_S (D(\chi_x + \nu\chi_y)\chi_x + D(\chi_y + \nu\chi_x)\chi_y + 2D(1-\nu)\chi_{xy}^2)\,\mathrm{d}S && (2.78)\\
&= \frac{1}{2}D\iint_S (\chi_x^2 + \chi_y^2 + 2\nu\chi_x\chi_y + 2(1-\nu)\chi_{xy}^2)\,\mathrm{d}S && (2.79)\\
&= \frac{1}{2}D\iint_S (\chi_x^2 + \chi_y^2 + 2\chi_x\chi_y - 2\chi_x\chi_y + 2\nu\chi_x\chi_y + 2(1-\nu)\chi_{xy}^2)\,\mathrm{d}S && (2.80)\\
&= \frac{1}{2}D\iint_S ((\chi_x + \chi_y)^2 - 2\chi_x\chi_y(1-\nu) + 2(1-\nu)\chi_{xy}^2)\,\mathrm{d}S && (2.81)\\
&= \frac{1}{2}D\int_0^{2\pi}\int_0^R \left[(\chi_x + \chi_y)^2 - 2(1-\nu)(\chi_x\chi_y - \chi_{xy}^2)\right] r\,\mathrm{d}\theta\,\mathrm{d}r && (2.82)
\end{aligned}$$

Finally, substituting the expressions of the curvatures into equation 2.82:

$$U = \frac{1}{2} D \int_0^{2\pi} \int_0^R \left[\left(\frac{\partial^2 w}{\partial r^2} + \frac{1}{r} \frac{\partial w}{\partial r} \right)^2 - 2(1-\nu) \left(\frac{\partial^2 w}{\partial r^2} \frac{1}{r} \frac{\partial w}{\partial r} \right) \right] r \, \mathrm{d}\theta \, \mathrm{d}r \quad (2.83)$$

This result can also be found in Clough and Penzien (1993). Since, as was previously mentioned, the plate deflection shape does not depend on θ, the plate equation 2.70 can be rewritten in terms of total derivatives:

$$\nabla_r^4 w(r) \equiv \left(\frac{\mathrm{d}^2}{\mathrm{d}r^2} + \frac{1}{r} \frac{\mathrm{d}}{\mathrm{d}r} \right) \left(\frac{\mathrm{d}^2 w}{\partial r^2} + \frac{1}{r} \frac{\mathrm{d}w}{\mathrm{d}r} \right) = \frac{p(r)}{D} \quad (2.84)$$

Introducing the identity:

$$\nabla_r^4 w(r) \equiv \frac{\mathrm{d}^2 w}{\mathrm{d}r^2} + \frac{1}{r} \frac{\mathrm{d}w}{\mathrm{d}r} = \frac{1}{r} \frac{\mathrm{d}}{\mathrm{d}r} \left(r \frac{\mathrm{d}w}{\mathrm{d}r} \right) \quad (2.85)$$

Equation 2.84 now becomes:

$$\frac{1}{r} \frac{\mathrm{d}}{\mathrm{d}r} \left\{ r \frac{\mathrm{d}}{\mathrm{d}r} \left[\frac{1}{r} \frac{\mathrm{d}}{\mathrm{d}r} \left(r \frac{\mathrm{d}w}{\mathrm{d}r} \right) \right] \right\} = \frac{p(r)}{D} \quad (2.86)$$

The solution of this equation is given by a sum of the solution of the associated homogeneous differential equation w_h and the particular solution w_p:

$$w = w_h + w_p \quad (2.87)$$

The solution of the associated homogeneous form of 2.86 is worked out:

$$w_h = C_1 \ln r + C_2 r^2 \ln r + C_3 r^2 + C_4 \quad (2.88)$$

where C_1, C_2, C_3 and C_4 are constants that can be evaluated from the boundary conditions. The particular solution w_p is obtained by successive integration of equation 2.86:

$$w_p = \int \frac{1}{r} \int r \int \frac{1}{r} \int \frac{r \, p(r)}{D} \, \mathrm{d}r \, \mathrm{d}r \, \mathrm{d}r \, \mathrm{d}r \quad (2.89)$$

If the slab is subjected to a uniform distributed load with intensity constant in the radial direction equal to $p(r) = p_0$, the particular solution is:

$$w_p = \frac{p_0 r^4}{64D} \quad (2.90)$$

Therefore the general solution of equation 2.86 is:

$$w(r) = C_1 \ln r + C_2 r^2 \ln r + C_3 r^2 + C_4 + \frac{p_0 r^4}{64D} \quad (2.91)$$

$$M_r = -D \left[C_1 \frac{1-\nu}{r^2} + 2C_2(1+\nu) \ln r + C_2(3+\nu) + 2C_3(1+\nu) + \frac{p_0 r^2}{16D}(3+\nu) \right] \quad (2.92)$$

Particular cases of boundary conditions must be considered in order to determine the four constants. This will be done in chapter 5, where two cases of practical interest will be thoroughly presented and solved.

Chapter 3

Dynamic analysis of circular plates

3.1 Generalities

An exact dynamic analysis is possible only for relatively simple structures (i.e., trusses, lumped structures, framed structures, unidimensional and some bidimensional simple structures). Rigorous analytic solutions are possible only when the load-time and resistance-displacement variations can be represented by convenient mathematical functions which can be handled quite easily (Kaplunov et al., 1998). Therefore it is useful, at least for practical design purposes, to adopt approximate methods which permit to perform analyses of even complex structures with reasonable accuracy (Biggs, 1964).
However, for many complex structural elements, it is too difficult to determine the exact modal shapes, therefore even the fundamental mode must be approximated (Biggs, 1964); generally it is very useful to adopt the elastic shape of deformation, normalized with respect to the maximum displacement.
It should be pointed out that structural dynamics problems usually involve significant uncertainties, in particular when defining the load-time function. For this reason, complex methods of analysis are often not justified, since it is a waste of time to employ methods having precision much greater than that of the input of the analysis (Biggs, 1964).

3.2 Governing differential equation

The dynamics of plates, which are systems with distributed mass and elasticity, can be modelled by using partial differential equations based on Newton's laws or by integral equations based on the principle of virtual displacements (Ventsel and Krauthammer, 2001). Within this framework, circular plates subjected to a uniform distributed load will be considered.
For design purposes only the lateral vibration is of interest, and the effects of extensional vibrations in the middle plane can be neglected. Therefore, the inertia forces, associated with the lateral translation of the plate, are considered (Ventsel and Krauthammer, 2001).

Damping effects are caused either by internal friction of the plate or by the surrounding media. Even though structural damping is theoretically present in all plate vibrations, in practice it has no effect on the natural frequencies and on the steady-state amplitudes; for this reason, it can be safely neglected in the preliminary discussion of the problem (Ventsel and Krauthammer, 2001).
The derivation of the governing differential equation of motion of plates can be obtained as an extension of the static case by adding effective forces that result from accelerations of the mass of the plate (the inertia forces).
By exploiting the D'Alambert's principle, the inertia forces can be added as reversed effective forces; moreover, even other time-varying forces (e.g., the damping forces) may be considered.
A plate can undergo a free vibration motion, which occurs in the absence of applied loads but may be initiated by applying initial conditions to the plate (Ventsel and Krauthammer, 2001). The free vibration motion is related to the plate natural characteristics, i.e. it depends only on the geometry and material of the plate. After this stage, there is a forced vibration motion, which is related to the application of a time-varying load. If the load applied to the plate has a periodicity, the forced vibration response will be harmonic; otherwise, it will give rise to a transient response.
The governing differential equation of motion will be worked out according to the thin plate theory, as presented in the previous chapter; i.e., the Kirchhoff's hypothesis will be exploited.
In order to model the undamped structural dynamics of plates, the elastic static equations derived in chapter 2 (equation 2.56 and equation 2.70) can be conveniently modified by including the time-varying variables.
If the applied dynamic loads and the inertia forces, as computed according to the D'Alambert's principle, are considered, the forcing term in the governing differential equation for the bending of thin circular plates becomes:

$$p(r,t) - f_I(r,t) = p(r,t) - \overline{m}\,\ddot{w}(r,t) = p(r,t) - \rho h\,\frac{\partial^2 w(r,t)}{\partial t^2} \tag{3.1}$$

where:

- $p(r,t)$ is the external applied load, expressed in terms of pressure distribution. Within this work the pressure will be considered to be uniformly distributed over the entire plate surface, thus the load will not be spatially variable but only function of the time, namely $p(t)$;
- $f_I(r,t)$ are the inertia forces;
- $\overline{m} = \rho\, h$ is the mass per unit area, where ρ is the concrete density.

Finally the differential equation of forced, undamped motion of thin circular plates results in:

$$D\nabla_r^4 w(r,t) = p(r,t) - \rho h\,\frac{\partial^2 w(r,t)}{\partial t^2} \tag{3.2}$$

A rigorous analytic solution of the governing differential equation 3.2 is achievable only in a limited number of simplified cases concerning plate geometry and boundary conditions (Ventsel and Krauthammer, 2001).
In this work, the dynamic analysis of plates treated as single-degree-of-freedom

(SDOF) systems will be developed, first according to the principle of virtual displacements and then according to the classical variational approach proposed by Lord Rayleigh (Chopra, 1995).

3.2.1 The equivalent SDOF method

In order to perform the dynamic analysis of a plate, which is a structural element with distributed mass and elasticity, the mass, the stiffness and the loading are replaced in the equation of motion with the equivalent values for a lumped mass-spring system (Morison, 2006). This is achieved by using either the principle of virtual displacement or the variational approach based upon energy. These approaches permit to obtain an equivalent system having kinetic energy, strain energy and external work equal to the distributed system.
The transformation coefficients which have to be applied to the distributed system in order to obtain the equivalent one are mainly a function of the assumed shape function of the deflected element. Actually, a structural element like a plate can deflect in an infinite variety of shapes, and for exact analysis it should be treated as an infinite-degree-of-freedom system (Chopra, 1995). However, it is possible to achieve approximate results with a certain degree of accuracy by restricting the deflections of the plate to a unique shape function $\psi(r)$, which can be viewed as an approximation of the fundamental mode of vibration. The shape function can be defined as the deflected shape at all points of the structural element, divided by the deflection at a chosen reference point, e.g. the point of maximum deflection; the accuracy of the approximation depends upon the particular deflected shape assumed. In general, any shape function consistent with the constraints of the supports may be assumed, but a good approximation is achieved when the static shape under the same load distribution of the blast loading is considered (Morison, 2006). Once a shape function has been hypothesized, the deflections over the entire plate area will be related only to the single displacement assumed as a reference (e.g., the midspan one), being this called the generalized SDOF. In other words, at a generic time instant t, the displacements at all locations of the plate are defined by means of the generalized coordinate $z(t)$ through the shape function $\psi(r)$, namely the plate deflections will be given by $w(r,t) = \psi(r)\, z(t)$.
One may need to assume, as will be done in this work, different shape functions according to the different stages of deformation which occur for an elastoplastic structural member; in such case there will be different transformation factors related to the corresponding shape function assumed for each different stage of the model.
In general, the equation of motion for a generalized SDOF has the following form:

$$m^* \ddot{z}(t) + c^* \dot{z}(t) + k^* z(t) = p^*(t) \tag{3.3}$$

where m^*, c^*, k^* and $p^*(t)$ are called the generalized mass, generalized damping, generalized stiffness and generalized load of the equivalent system, respectively. Within this work, only undamped motion will be studied, thus c^* will be set equal to zero, since, as was previously mentioned, it can be safely neglected in a preliminary discussion of the problem. Once obtained equation 3.3, one can apply the same procedures which can be found in literature for the dynamic

response analysis of a SDOF system.
According to Biggs (1964), it is possible to normalize the transformation factors by using the corresponding total parameters, obtaining:

$$K_M = \frac{m^*}{m_t} \tag{3.4}$$

$$K_R = \frac{k^*}{k_t} \tag{3.5}$$

$$K_L = \frac{p^*(t)}{p_t(t)} \tag{3.6}$$

where:

- K_M, K_R and K_L are called the mass factor, resistance factor and load factor, respectively;
- m_t is the total mass [M];
- k_t is the force per unit displacement [F/L];
- $p_t(t)$ is the total load [F].

Once the transformation coefficients have been normalized, the equation of motion stated above (equation 3.3) can be rewritten as:

$$K_M\, m_t\, \ddot{z}(t) + K_R\, k_t\, z(t) = K_L\, p(t) \tag{3.7}$$

Obviously, the key aspect in the procedure just explained is in the evaluation of the transformation coefficients, computed, as previously mentioned, either by means of the principle of virtual displacements or by means of the variational approach, which will be both reviewed in the following subsections.

3.2.2 The principle of virtual displacements

As was previously mentioned, to approximate the motion of a plate system with a single degree of freedom it is necessary to assume that it will deform only in a single shape. The symmetry of circular plates and the transformation to polar coordinates allow to simplify even more the problem, expressing the shape function with dependence of only the variable r. The shape function will be called $\psi(r)$, and the amplitude of the motion will be represented by the generalized coordinate $z(t)$; thus:

$$w(r,t) = \psi(r)z(t) \tag{3.8}$$

The shape function adopted is the elastic deformation shape obtained from the solution of the static case having the same load distribution as occurs in the blasting event. The equation of motion of this generalized SDOF system can be formulated conveniently only by work or energy principles, and the principle of virtual work will be used in this case (Clough and Penzien, 1993). The principle of virtual work requires the system to be conservative, namely no losses of energy take place. Then the energy present in the system is composed by the external virtual work (which is performed by external forces and inertia forces acting through virtual displacements) and the internal work. The principle of virtual displacements states that *if the system in equilibrium is subjected to virtual displacements $\delta w(r)$, the external work δW_E is equal to the internal virtual work δW_I* (Chopra, 1995):

$$\delta W_I = \delta W_E \tag{3.9}$$

The external virtual work is composed by the inertia forces $f_I(r,t)$ acting through the virtual displacement $\delta w(r)$ and the work done by the external forces. Referring to a generic circular plate one can write:

$$\delta W_E = \int_0^{2\pi}\int_0^R p(r,t)\,\delta w(r)\,r\,\mathrm{d}\theta\,\mathrm{d}r - \int_0^{2\pi}\int_0^R f_I(r,t)\,\delta w(r)\,r\,\mathrm{d}\theta\,\mathrm{d}r \tag{3.10}$$

As was previously mentioned (equation 3.1), the inertia forces can be computed by using the D'Alambert's principle and they are equal to:

$$f_I(r,t) = \overline{m}\,\ddot{w}(r,t) \tag{3.11}$$

Substituting equation 3.11 into equation 3.10 one can get:

$$\delta W_E = \int_0^{2\pi}\int_0^R p(r,t)\,\delta w(r)\,r\,\mathrm{d}\theta\,\mathrm{d}r - \int_0^{2\pi}\int_0^R \overline{m}\,\ddot{w}(r,t)\,\delta w(r)\,r\,\mathrm{d}\theta\,\mathrm{d}r \tag{3.12}$$

The internal virtual work is due to the bending moments acting through the curvatures associated with the virtual displacements:

$$\delta W_I = \int_0^{2\pi}\int_0^R (M_r\,\delta\chi_r + M_\theta\,\delta\chi_\theta + 2M_{r\theta}\,\delta\chi_{r\theta})\,r\,\mathrm{d}\theta\,\mathrm{d}r \tag{3.13}$$

The same computation was already performed in chapter 2 in order to obtain the elastic strain energy of a circular plate (see equations 2.82 and 2.83). The external and internal virtual works are then expressed in terms of the generalized coordinate $z(t)$ and the shape function $\psi(r)$, i.e. one must consider that:

$$w''(r,t) = \psi''(r)\,z(t) \qquad \ddot{w}(r,t) = \psi(r)\,\ddot{z}(t) \tag{3.14}$$

The virtual displacement is chosen to be consistent with the selected shape function, and the virtual curvature is obtained accordingly:

$$\delta w(r) = \psi(r)\,\delta z \qquad \delta[w''(r)] = \psi''(r)\,\delta z \tag{3.15}$$

Performing the needed substitutions one can obtain:

$$\delta W_E = \delta z \left[\int_0^{2\pi} \int_0^R p(r,t)\psi(r)\, r\, \mathrm{d}\theta\, \mathrm{d}r - \ddot{z} \int_0^{2\pi} \int_0^R \overline{m}\, \psi^2(r)\, r\, \mathrm{d}\theta\, \mathrm{d}r \right] \tag{3.16}$$

$$\delta W_I = \delta z \left[z(t) D \int_0^{2\pi} \int_0^R \left(\frac{\partial^2 \psi}{\partial r^2} + \frac{1}{r}\frac{\partial \psi}{\partial r} \right)^2 - 2(1-\nu) \left(\frac{\partial^2 \psi}{\partial r^2} \frac{1}{r} \frac{\partial \psi}{\partial r} \right) r\, \mathrm{d}\theta\, \mathrm{d}r \right] \tag{3.17}$$

Now the substitution of equations 3.16 and 3.17 into equation 3.9 yields:

$$\delta z \left[m^* \ddot{z} + k^* z + L^* p(t) \right] = 0 \tag{3.18}$$

with the transformation coefficients equal to:

$$m^* = \int_0^{2\pi} \int_0^R \overline{m}\, \psi^2(r)\, r\, \mathrm{d}\theta\, \mathrm{d}r \tag{3.19}$$

$$k^* = D \int_0^{2\pi} \int_0^R \left[\left(\frac{\partial^2 \psi}{\partial r^2} + \frac{1}{r}\frac{\partial \psi}{\partial r} \right)^2 - 2(1-\nu) \left(\frac{\partial^2 \psi}{\partial r^2} \frac{1}{r} \frac{\partial \psi}{\partial r} \right) \right] r\, \mathrm{d}\theta\, \mathrm{d}r \tag{3.20}$$

$$L^* = \int_0^{2\pi} \int_0^R \psi(r)\, r\, \mathrm{d}\theta\, \mathrm{d}r \tag{3.21}$$

where:

- $k^* = k_e^*$ represents the stiffness of the generalized SDOF in the elastic phase and $k^* = k_p^* = 0$ represents the plateau in the plastic phase;
- L^* is the coefficient that must be applied to the external load in order to get the generalized load.

As last remark, it is worth noting that the equations for m^* and L^* are valid for the elastic and plastic phase, just taking into account that the shape function $\psi(r)$ changes from one stage to the other.

3.2.3 The variational approach

Keeping in mind that, for design purposes, the natural fundamental frequencies are of the greatest interest, the Rayleigh's method is a variational energetic approach which permits to find the lowest natural frequency of a vibrating plate (Ventsel and Krauthammer, 2001). This principle was developed in the nineteenth century by Lord Rayleigh and it is based on the assumption that if the vibrating system is conservative (i.e., no energy is added or lost), then the maximum kinetic energy, K_{max}, must be equal to the maximum potential (strain) energy, U_{max} (Ventsel and Krauthammer, 2001).
Let's consider an elastic circular plate undergoing free vibrations as a system with one degree of freedom, where the motion of the generalized SDOF coincides with the motion of the central point in the plate. Since only free flexural vibrations are of interest, the Rayleigh's principle can be written as:

$$U_{max} = K_{max} \tag{3.22}$$

It should be noticed that this principle is essentially a restatement of the conservation of energy principle.
The strain energy of the slab, which was previously worked out, is given by equation 2.83, and it is equal to:

$$U = \frac{1}{2} D \int_0^{2\pi} \int_0^R \left[\left(\frac{\partial^2 w}{\partial r^2} + \frac{1}{r}\frac{\partial w}{\partial r} \right)^2 - 2(1-\nu) \left(\frac{\partial^2 w}{\partial r^2} \frac{1}{r} \frac{\partial w}{\partial r} \right) \right] r \, \mathrm{d}\theta \, \mathrm{d}r$$

The kinetic energy of the plate is:

$$K = \frac{1}{2} \int_0^{2\pi} \int_0^R \rho h \left(\frac{\partial w(r,t)}{\partial t} \right)^2 r \, \mathrm{d}\theta \, \mathrm{d}r \tag{3.23}$$

Hypothesizing that the plate is undergoing harmonic vibrations, its middle plane can be approximated by:

$$w(r,t) = \psi(r) \sin(\omega t) \tag{3.24}$$

where:

- $\psi(r)$ is a continuous function that approximately represents the shape of the plate's deflected middle plane and satisfies at least the kinematic boundary conditions;
- ω is the unknown natural frequency of the plate related to the assumed shape function.

Substituting expression 3.24 into equation 3.23 for the kinetic energy, one can obtain:

$$K = \frac{\omega^2}{2} \cos^2(\omega t) \int_0^{2\pi} \int_0^R \rho h \psi^2(r) \, r \, \mathrm{d}\theta \, \mathrm{d}r \tag{3.25}$$

It is apparent that the kinetic energy expression reaches a maximum when $\cos(\omega t) = 1$. Therefore:

$$K_{max} = \frac{\omega^2}{2} \int_0^{2\pi} \int_0^R \rho h \psi^2(r) \, r \, \mathrm{d}\theta \, \mathrm{d}r \tag{3.26}$$

The strain energy reaches its maximum when the deflection is at its maximum. For the deflected middle surface, U_{max} occurs when $\sin(\omega t) = 1$. It can be easily shown that under this condition the maximum strain energy of the vibrating plate is identical to that derived for the static case (Ventsel and Krauthammer, 2001).
Substituting the expressions for the maximum values of the strain and kinetic energies, respectively, into equation 3.22, one can get the fundamental frequency of the system:

$$\omega^2 = \frac{2U_{max}}{\int_0^{2\pi} \int_0^R \rho h \psi^2(r)\, r \, \mathrm{d}\theta \, \mathrm{d}r} = \frac{k_e^*}{m_e^*} \tag{3.27}$$

It is apparent that this result yields the same expressions for the generalized mass and the generalized stiffness that were worked out in the previous section by using the principle of virtual displacements.

It should be pointed out that the accuracy of determining the natural frequencies depends on the successful selection of the expression for $\psi(r)$ (Ventsel and Krauthammer, 2001). As was previously mentioned, usually the function $\psi(r)$ is chosen to be proportional to a static deflection of a plate with the same boundary conditions as for the plate of interest under a uniformly distributed surface load p_0. In other words, the plate surface corresponding to the fundamental mode is identical to that deflected by a uniform distributed load in the static case (Morison, 2006; Ventsel and Krauthammer, 2001). The approximate fundamental frequency computed from Rayleigh's principle is always higher than the exact value, since one arbitrarily stiffens the plate by assuming a modal shape, therefore increasing its frequency (Ventsel and Krauthammer, 2001).

3.3 Elastoplastic idealization

In the previous section it was shown how it is possible to reduce the plate system to a generalized SDOF system with an elastic perfectly plastic behaviour by using the elastic and plastic shape functions (which are different) respectively for each stage. Elastic and plastic parameters of the plate are reduced in such a way that the generalized SDOF could represent equivalently the overall behaviour of the system. In any case, in order to achieve the complete description of the elastoplastic behaviour, it is necessary to define the following parameters: k_e^* (the generalized elastic stiffness), w_{el} (the displacement at the elastic limit), F_{su} (the collapse load). All these parameters are illustrated in figure 3.1, in which the solid line represents the resistance function for a real elastoplastic system, whilst the dashed line represents the resistance function for an idealized elastic-perfectly plastic SDOF system.
The value of k_e^* is found in a relatively simple way by using the elastic shape function and the general elastic parameters of the plate; for the other parameters (F_{su}, w_{el}) it is necessary to study the plastic behaviour of the plate, hypothesizing the right collapse mechanism by using the upper bound approach of limit analysis theory.

The limit analysis tries to find a limit load, or collapse load, for which the plastic deformation can increase without limit under a constant limit load (Save et al., 1997; Chen and Han, 1988; Young and Budynas, 2001). The upper-bound principle states that *if there is potential failure mechanism for which the dissipation rate is smaller than the external power supplied by the given loads, the structure will collapse under such loads* (Jirasek and Bazant, 2001). Due to the fact that there are many possible failure mechanisms, the problem is how to find out which is the right one by using the upper bound principle. Actually, the right collapse load will be the minimum load able to produce the collapse. In the case of slabs, the system is a bidimensional structure where yield lines will create progressively until the collapse. The internal energy is represented by the dissipation of plastic energy performed by the yield lines. Selecting the right collapse mechanism is not simple, taking into account that there are many collapse mechanisms and that, at the same time, they depend on boundary conditions, position of the loads, slab geometry and material characteristics. In chapter 5 these concepts will be applied and developed in detail for some specific cases of interest.

From the upper bound theory, using the most probable collapse mechanism, it is feasible to obtain the maximum load resistance or collapse load F_{su}. This load represents the external charge for which the plate develops the minimum of yield lines necessary to reach an imminent collapse.

Now, assuming that a SDOF system behaves like an elastic-perfectly plastic material, it is easy to define the value of w_{el}, which is equal to $w_{el} = F_{su}/k_e^*$. Considering an elastic-perfectly plastic behaviour of a generalized SDOF has many advantages in terms of simplicity, calculation efficiency, computational performance and great usefulness in the solution of further applications like energy evaluation or pressure-impulse diagrams generation. An elastic-perfectly plastic system assumes that the total yield lines that lead to the collapse are developed at the same time (at the peak, when the system changes its stage from the elastic to the plastic one), which is not exactly real, because the yield lines in a slab are creating progressively with the increment of the load until

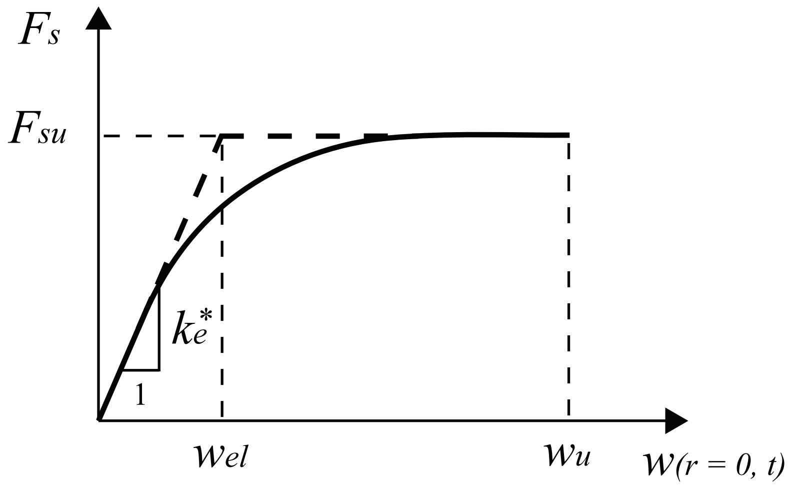

Figure 3.1: Resistance function for a SDOF system.

the system reaches the maximum resistance force and thereby the collapse. For instance, in the case of a circular clamped slab with a radial charge, the circular yield line at the border will appear first, and then they will be followed by the formation of the radial lines until the collapse. This losing of stiffness is also progressive, describing a non-linear elastoplastic behaviour, as shown in figure 3.1. However, the assumption of elastic-perfectly plastic behaviour is a good approximation, enough accurate for preliminary assessment purposes. Dealing with a more complex type of elastoplasticity is very complex and it does not represent a considerable gain of accuracy for our applications.

Figure 3.2 illustrates the SDOF idealization assumed for the circular slabs treated in this work, in both elastic and plastic stage. The mass of the equivalent system is assumed to be concentrated at the center of the slab, and the degree of freedom characterizing the system is represented by the corresponding midspan displacement, which is the maximum one over the slab area and it is time-varying, i.e. $w_{max} = w(r = 0, t)$. In the elastic stage the generalized stiffness of the SDOF system k_e^* is represented by a spring, whilst in the plastic stage the stiffness is set equal to zero, and in the sketch this is represented by a slider.

The assessment of the damage threshold $\widetilde{w}_{max}$ is more complicated since it depends on the plastic properties of the plate's material, thus a suitable damage criterion should be chosen. This procedure consists in the definition of a maximum crack opening displacement in the middle of the plate, which corresponds to the maximum deformed zone. The complete illustration of the $\widetilde{w}_{max}$ assessment procedure is developed in chapter 5 for some type of materials (R/C, FRC).

After the definition of the already mentioned parameters, it is possible to describe the behaviour of the system for the application of a monotonic load, but there is still the possibility of an eventual reversion of the load. Actually an unloading and reloading process shows the so-called *Bauschinger effect* (Chen and Han, 1988), namely the correspondence between stress and strain in a plastically deformed system is not one-to-one. This means that the strain is not only function of the stress, but depends on the previous loading history. This consideration is very important when the structure is subjected to dynamic loads, because the dynamic response for every interval of time has to be referred to the last step, taking into account the loading history. For this purpose, it is convenient to introduce the incremental displacement and the incremental resistance force. Figure 3.3 focuses on this issue. When $\dot{w} > 0$ and $\dot{F}_s > 0$ (which represent a positive increment in the displacement and in the resistance function, respectively) the elastic loading branch is followed; when $\dot{w} < 0$ and $\dot{F}_s < 0$ the elastic unloading branch is followed; when $\dot{F}_s = 0$ the plastic plateau has been reached. Obviously, when an elastic branch is followed, $\dot{F}_s$ is proportional to $\dot{w}$ through k_e^*. As last remark, please note that the inversion of the loading corresponds to the peaks in the chosen dynamic response parameter, e.g. the displacement.

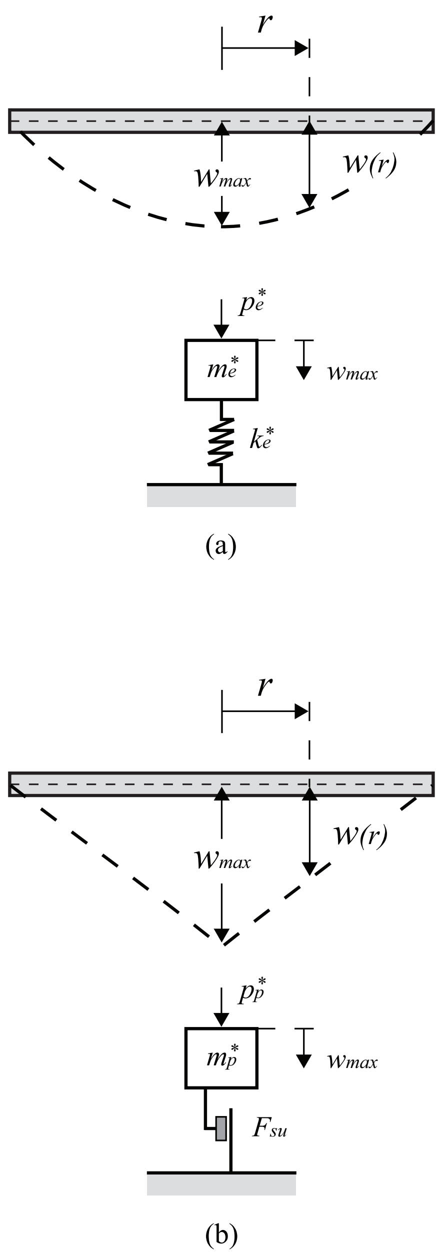

Figure 3.2: Single degree of freedom idealization: (a) elastic stage; (b) plastic stage.

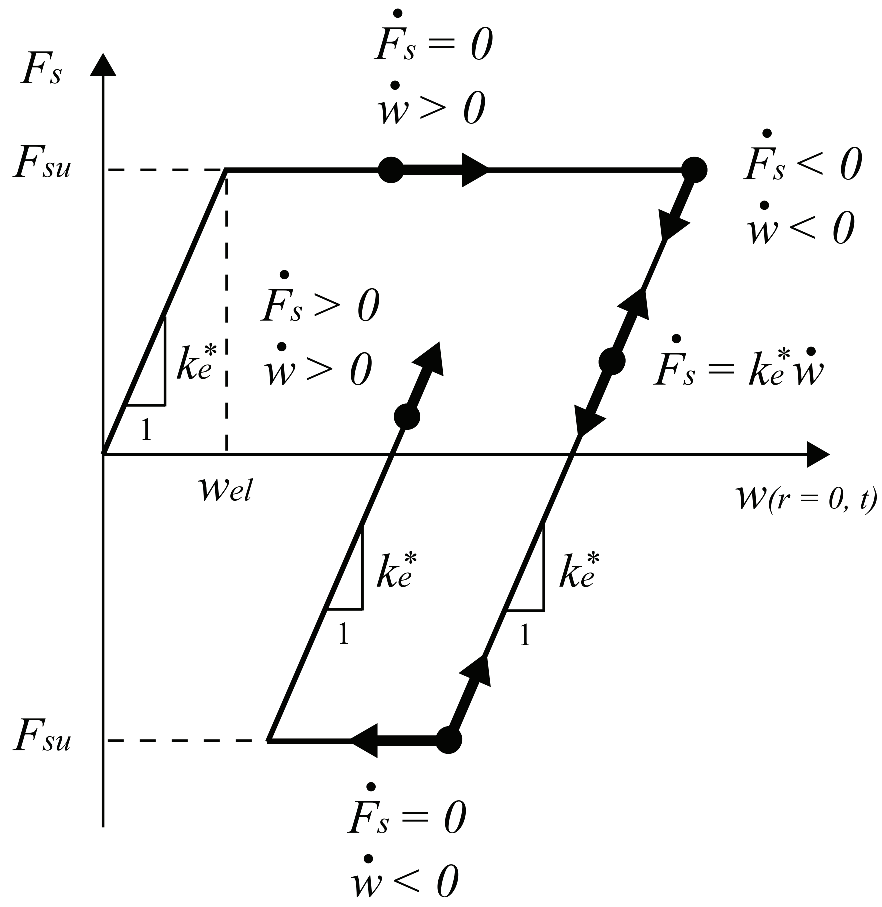

Figure 3.3: Resistance function for loading/unloading cycles.

3.4 Numerical evaluation of the dynamic response

3.4.1 Pulse shapes

In this section some pulse shapes are proposed for the dynamic analysis. These shapes represent an approximation of the real load-time excitation in a blasting event that was discussed in the first chapter. Generally the loading history shows a growing path, reaching the maximum shock pressure in a very short time; sometimes this growing path is so small that can be neglected. Then a decay path, which is usually much longer than the growing path, shows how the blasting shock is dissipated until a time t_d.
In the present work several pulse shapes will be assumed, as illustrated in figure 3.4. A rectangular shape function was also taken into account in order to analyse a very intensive shock or an idealized permanent load.

It is convenient to anticipate here some calculations that will turn to be useful in the development of the pressure-impulse diagrams. Once a pulse shape is selected, the numerical code computes the time duration of the pulse associated to the chosen shape and to the values of its peak pressure p_{max} and specific impulse i. The time duration of the load is necessary to perform the dynamic analysis by means of the generalized SDOF as will be discussed in the next sections.
The expressions to obtain the time duration of the load t_d for a certain pulse shape from a generic pair of $(i; p_{max})$ values are listed in the following, along with the analytical expressions of the pulses.

(a) General triangular pulse. The analytical expression of the pressure-time curve for this case is:

$$p(t) = \begin{cases} p_{max}\dfrac{t}{t_r} & \text{if } 0 \le t \le t_r, \\ p_{max}\left(1 - \dfrac{t-t_r}{t_d-t_r}\right) & \text{if } t_r < t \le t_d, \\ 0 & \text{if } t > t_d. \end{cases} \tag{3.28}$$

where t_r is the rise time to reach the peak load p_{max}.
In this case the time duration of the load is obviously given by:

$$t_d = \frac{2i}{p_{max}} \tag{3.29}$$

(b) Right-angle triangular pulse. The analytical expression of the pressure-time curve for this case is:

$$p(t) = \begin{cases} p_{max}\left(1 - \dfrac{t}{t_d}\right) & \text{if } 0 \le t \le t_d, \\ 0 & \text{if } t > t_d. \end{cases} \tag{3.30}$$

In this case the time duration of the load is obviously given by:

$$t_d = \frac{2i}{p_{max}} \tag{3.31}$$

(c) Rectangular pulse. The analytical expression of the pressure-time curve for this case is:

$$p(t) = \begin{cases} p_{max} & \text{if } 0 \leq t \leq t_d, \\ 0 & \text{if } t > t_d. \end{cases} \tag{3.32}$$

In this case the time duration of the load is obviously given by:

$$t_d = \frac{i}{p_{max}} \tag{3.33}$$

(d) Half sine pulse. The analytical expression of the pressure-time curve for this case is:

$$p(t) = \begin{cases} p_{max} \sin\left(\pi \dfrac{t}{t_d}\right) & \text{if } 0 \leq t \leq t_d, \\ 0 & \text{if } t > t_d. \end{cases} \tag{3.34}$$

The general expression to compute the specific impulse is:

$$i = \int_0^{t_d} p(t)\mathrm{d}t \tag{3.35}$$

Hence:

$$i = \int_0^{t_d} p_{max} \sin\left(\pi \frac{t}{t_d}\right) \mathrm{d}t = \frac{2p_{max}}{\pi}\, t_d \tag{3.36}$$

Therefore, for a generic point of coordinates $(i; p_{max})$ in the pressure-impulse plane, the time duration of the load in the case of a half-sine pulse shape can be determined as follows:

$$t_d = \frac{\pi\, i}{2p_{max}} \tag{3.37}$$

(e) Exponential pulse. The analytical expression of the pressure-time curve for this case is:

$$p(t) = \begin{cases} p_{max} \dfrac{e^{\lambda(t_d - t)}}{e^{\lambda\, t_d} - 1} & \text{if } 0 \leq t \leq t_d, \\ 0 & \text{if } t > t_d. \end{cases} \tag{3.38}$$

The specific impulse is given by:

$$i = \int_0^{t_d} p(t)\mathrm{d}t = p_{max} \int_0^{t_d} \frac{e^{\lambda(t_d - t)}}{e^{\lambda\, t_d} - 1} \mathrm{d}t \tag{3.39}$$

Finally:

$$i = \left(\frac{1}{\lambda} - \frac{t_d}{e^{\lambda\, t_d} - 1}\right) p_{max} \tag{3.40}$$

For a generic point of coordinates $(i; p_{max})$ in the p-i plane, equation 3.40 can be solved numerically to get the time duration of the load. It should be pointed out that the value of the exponential coefficient λ plays a very important role in the definition of the shape of the exponential pulse. In particular, if $\lambda \to 0$, one gets the right-angle triangular pulse; if $\lambda << 0$, the pulse shape is convex, and at the limit $\lambda \to -\infty$ it coincides with the rectangular pulse; finally, if $\lambda >> 0$, the pulse shape is concave, and at the limit $\lambda \to +\infty$ it becomes an ideal pulse.

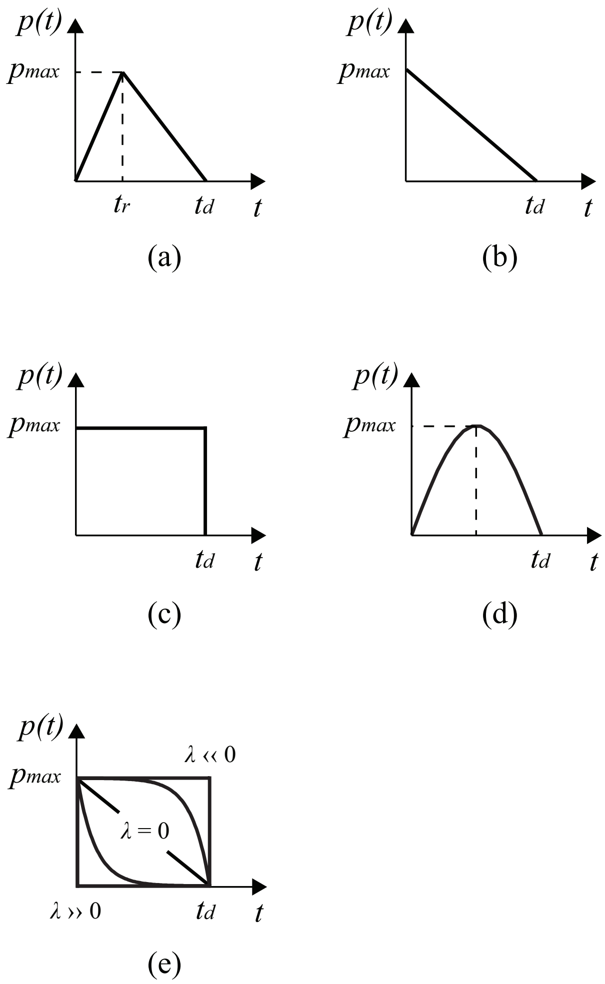

Figure 3.4: The different pulse shapes that were used in the present work: (a) general triangular pulse, with rise time t_r to reach the peak load p_{max}; (b) right-angle triangular pulse; (c) rectangular pulse; (d) half-sine pulse; (e) exponential pulse, with exponential coefficient λ.

3.4.2 Average acceleration method

In order to perform the dynamic analysis, a numerical approach will be used, which goes under the name of *average acceleration method*. The basic assumption under this procedure is that the value of the acceleration remains constant all over the time-step of interest. The numerical nature of this method allows to take into account also for complex loading functions and non-linear behaviours. In the following, a detailed description of the procedure will be carried out, along with the formulae implemented in the numerical code.

Initial time step calculations. Under the hypothesis that the loading history starts being the system on the elastic branch, the initial values of the generalized parameters are set equal to the elastic ones:

$$m_0^* = m_e^* \qquad k_0^* = k_e^* \qquad L_0^* = L_e^* \tag{3.41}$$

Moreover, the initial values of displacement and velocity are set equal to zero:

$$z_0 = 0 \qquad v_0 = 0 \tag{3.42}$$

The evaluation of p_0 (the initial value of the load function) is carried out according to the selected load shape. In the case of general triangular pulse and half sine pulse, the value of p_0 will be set equal to zero, while in the other three cases, it will be equal to $p_{max}\, L_0^*$.

The initial value of the resistance function is given by:

$$F_{s,0} = k_0^*\, z_0 \tag{3.43}$$

With these parameters computed, it is now possible to derive the acceleration as follows:

$$a_0 = \frac{p_0^* - F_{s,0}}{m_0^*} \tag{3.44}$$

i-th time step. It is useful to define a vector called $z_{vel,change}$ which takes into account the values of displacement for which a velocity sign inversion occurs. Analogously, a vector called $t_{vel,change}$ is defined, which takes into account the values of time for which a velocity sign inversion occurs. It has also been introduced a counter for the velocity sign inversion points. This was done in order to obtain a certain number of peaks (n_{peaks}) in the dynamic response of the system before the dynamic analysis stops; i.e., the analysis will continue until a certain number of peaks (defined by the user) will be computed.

Evaluation of p_{i+1}^* according to the selected load shape. The evaluation of the load function at the $i+1$-th time-step must be carried out according to the selected pulse shape. In the following, the formulae used in the numerical procedure are outlined in detail. These formulae were obtained simply by performing a discretization process of the corresponding analytical expressions presented in the preceding section about pulse shapes.

(a) General triangular pulse.

$$p^*_{i+1} = \begin{cases} L^*_i\, p_{max} \dfrac{i\triangle t}{t_r} & \text{if } i\triangle t \leq t_r, \\ L^*_i\, p_{max} \left(1 - \dfrac{\triangle t - t_r}{t_d - t_r}\right) & \text{if } i\triangle t \leq t_d, \\ 0 & \text{if } i\triangle t > t_d. \end{cases} \tag{3.45}$$

where t_r is the rise time to reach the peak load p_{max}.

(b) Right-angle triangular pulse.

$$p^*_{i+1} = \begin{cases} L^*_i\, p_{max} \left(1 - \dfrac{i\triangle t}{t_d}\right) & \text{if } i\triangle t \leq t_d, \\ 0 & \text{if } i\triangle t > t_d. \end{cases} \tag{3.46}$$

(c) Rectangular pulse.

$$p^*_{i+1} = \begin{cases} L^*_i\, p_{max} & \text{if } i\triangle t \leq t_d, \\ 0 & \text{if } i\triangle t > t_d. \end{cases} \tag{3.47}$$

(d) Half sine pulse.

$$p^*_{i+1} = \begin{cases} L^*_i\, p_{max} \sin\left(\pi\, \dfrac{i\triangle t}{t_d}\right) & \text{if } i\triangle t \leq t_d, \\ 0 & \text{if } i\triangle t > t_d. \end{cases} \tag{3.48}$$

(e) Exponential pulse.

$$p^*_{i+1} = \begin{cases} L^*_i\, p_{max} \dfrac{e^{\lambda(t_d - i\triangle t)}}{e^{\lambda\, t_d} - 1} & \text{if } i\triangle t \leq t_d, \\ 0 & \text{if } i\triangle t > t_d. \end{cases} \tag{3.49}$$

Other quantities at the i-th time step. In order to compute the increment in the displacement function $\triangle z_i$ and the increment in the velocity $\triangle v_i$ at the i-th time-step, it is convenient to define the quantities $\triangle\widetilde{p}_i$ and $\widetilde{k}^*_i$ as follows:

$$\triangle\widetilde{p}_i = p^*_{i+1} - p^*_i + m^*_i \left(4\frac{v_i}{\triangle t} + 2a_i\right) \tag{3.50}$$

$$\widetilde{k}^*_i = k^*_i + \frac{4}{\triangle t^2}\, m^*_i \tag{3.51}$$

Finally the increment in displacement and in velocity at the i-th time-step are given by:

$$\triangle z_i = \frac{\triangle\widetilde{p}_i}{\widetilde{k}^*_i} \tag{3.52}$$

$$\triangle v_i = \frac{2}{\triangle t}\, \triangle z_i - 2v_i \tag{3.53}$$

Evaluation of displacement and velocity at the subsequent time step. With the increments previously computed, it is now possible to work out the values of displacement and velocity at the $i+1$-th time-step:

$$z_{i+1} = z_i + \triangle z_i \tag{3.54}$$

$$v_{i+1} = v_i + \triangle v_i \tag{3.55}$$

Generalized parameters evaluation. For the calculation of the transformation coefficients, it is necessary to know whether the system is following the elastic or the plastic branch, and this is easily achieved by studying the sign of the velocity in two successive time-steps.
This issue is clearly illustrated in figure 3.5, which can be viewed as the numerical counterpart of figure 3.3. In this figure, the squares represent the points in which the ultimate resistance F_{su} force is reached. The circular crowns represent the points in which an inversion of the velocity sign occurs. If the velocity sign reverses, the path switches from the loading to the unloading branch, or vice-versa. If then the reloading/unloading branch is followed, the generalized properties of the system (mass, stiffness and load) to be used in the subsequent computations are the elastic ones, until the limit resistance F_{su} is reached again. The mathematical form of the issue just outlined is given in the following. If the sign of the velocity does not change between a certain time step and the subsequent one, namely:

$$\frac{v_i}{v_{i+1}} \geq 0 \tag{3.56}$$

then

$$F_{s,i+1} = F_{s,i} + k_i^* \triangle z_i \tag{3.57}$$

If the value of F_{i+1} given by equation 3.57 is greater than the ultimate resistance force F_{su}, then the system has reached the plastic stage. In this case the value of F_{i+1} is brought back by the numerical code to the ultimate resistance F_{su} and the generalized characteristics of the system at the $i+1$-th time step are set equal to the plastic ones. Otherwise, if the elastic branch is still followed, F_{i+1} is computed as:

$$F_{s,i+1} = F_{s,i} + k_e^* \triangle z_i \tag{3.58}$$

and the generalized characteristics of the system at the $i+1$-th time step are set equal to the plastic ones.

Evaluation of the acceleration at the subsequent time step. The final step of the average acceleration procedure provides the value of the acceleration at the $i+1$-th time-step:

$$a_{i+1} = \frac{1}{m_i} \left(p_{i+1}^* - F_{s,i+1} \right) \tag{3.59}$$

Once this computation is performed, the procedure just outlined is iterated until the desired number of peaks in the response parameter is obtained.

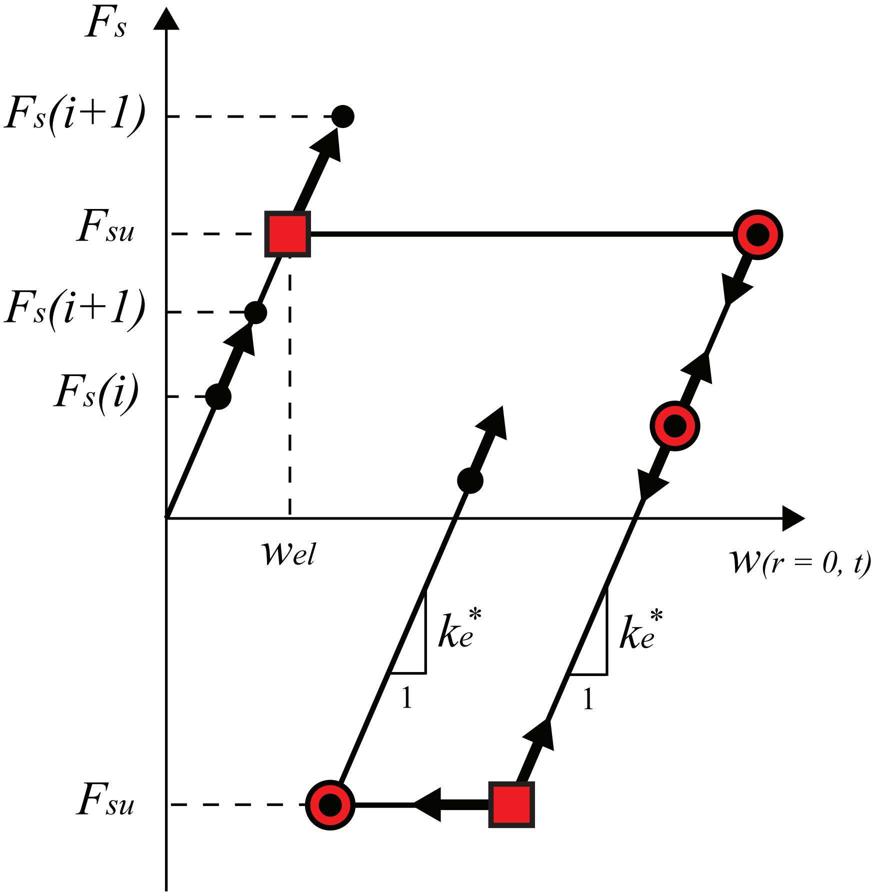

Figure 3.5: Resistance function for loading/unloading cycles: numerical development.

3.5 Flow charts of the MATLAB® codes

In order to illustrate the procedures which were implemented as numerical codes using the MATLAB® program (Magrab et al., 2010), many flow charts were created, which present in a scheme form all the algorithms that were written for the dynamic analysis and, later, for the pressure-impulse diagrams development. The notation in which the flowcharts herein presented were developed is based upon the Unified Modelling Language (UML) contained in the book *UML Distilled Third Edition* (Fowler, 2003), amongst the other authors.
The flowcharts representing the dynamic analysis main code along with its subfunctions are given in the following pages. These can be prove useful to understand and manage the numerical codes that were developed within the framework of this thesis.

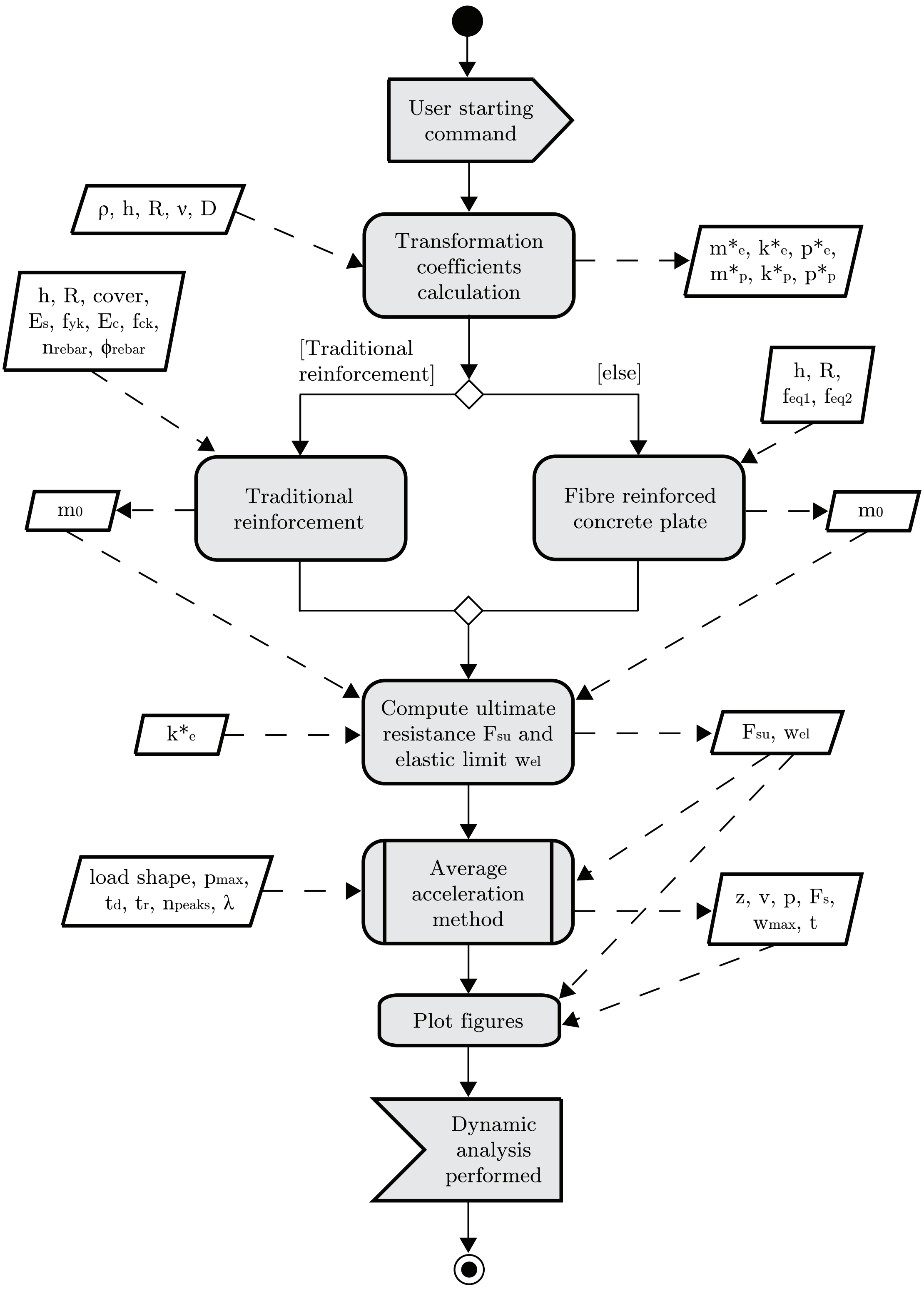

Figure 3.6: Flow chart of the dynamic analysis main code.

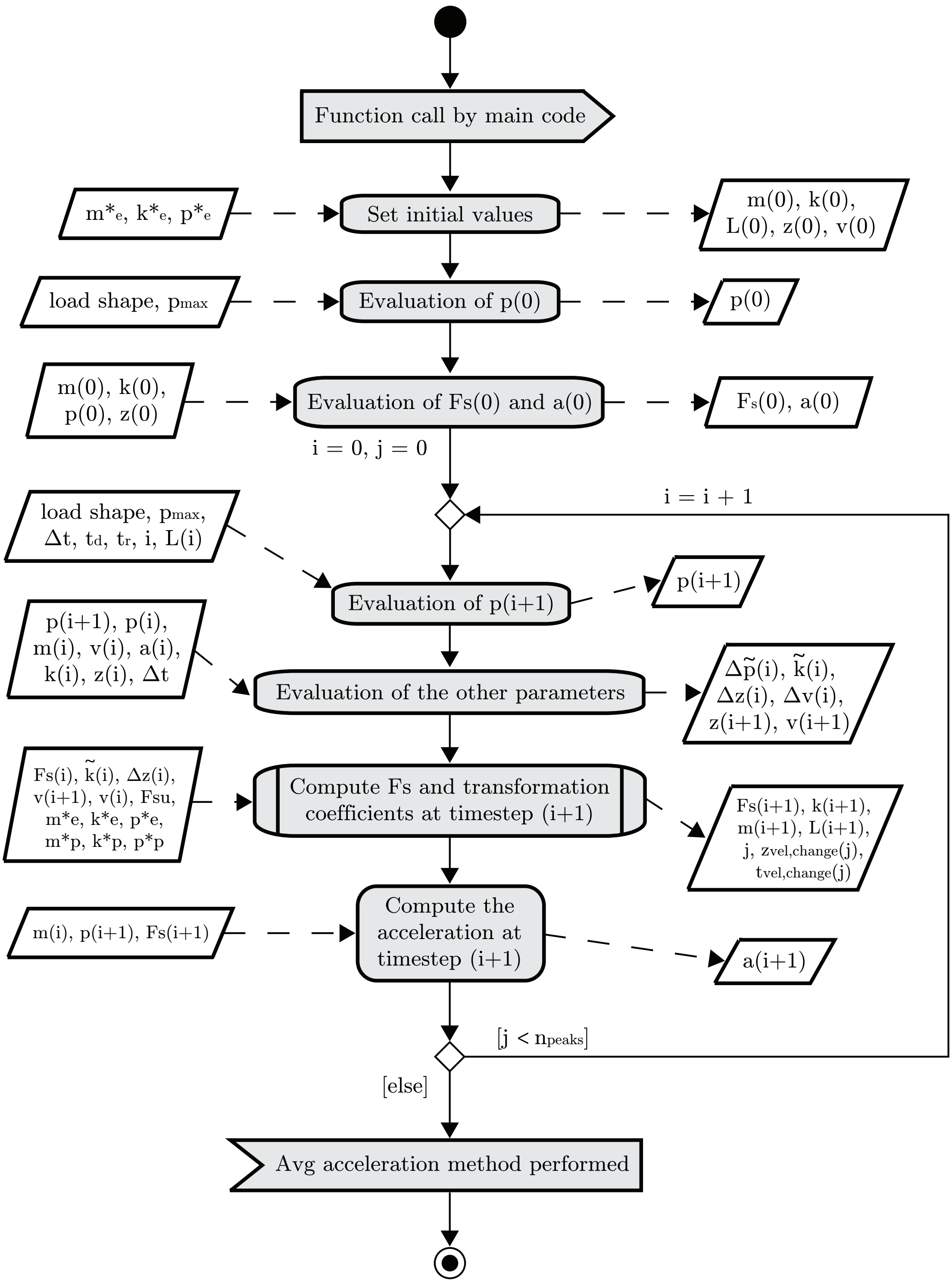

Figure 3.7: Flow chart of the average acceleration method subfunction.

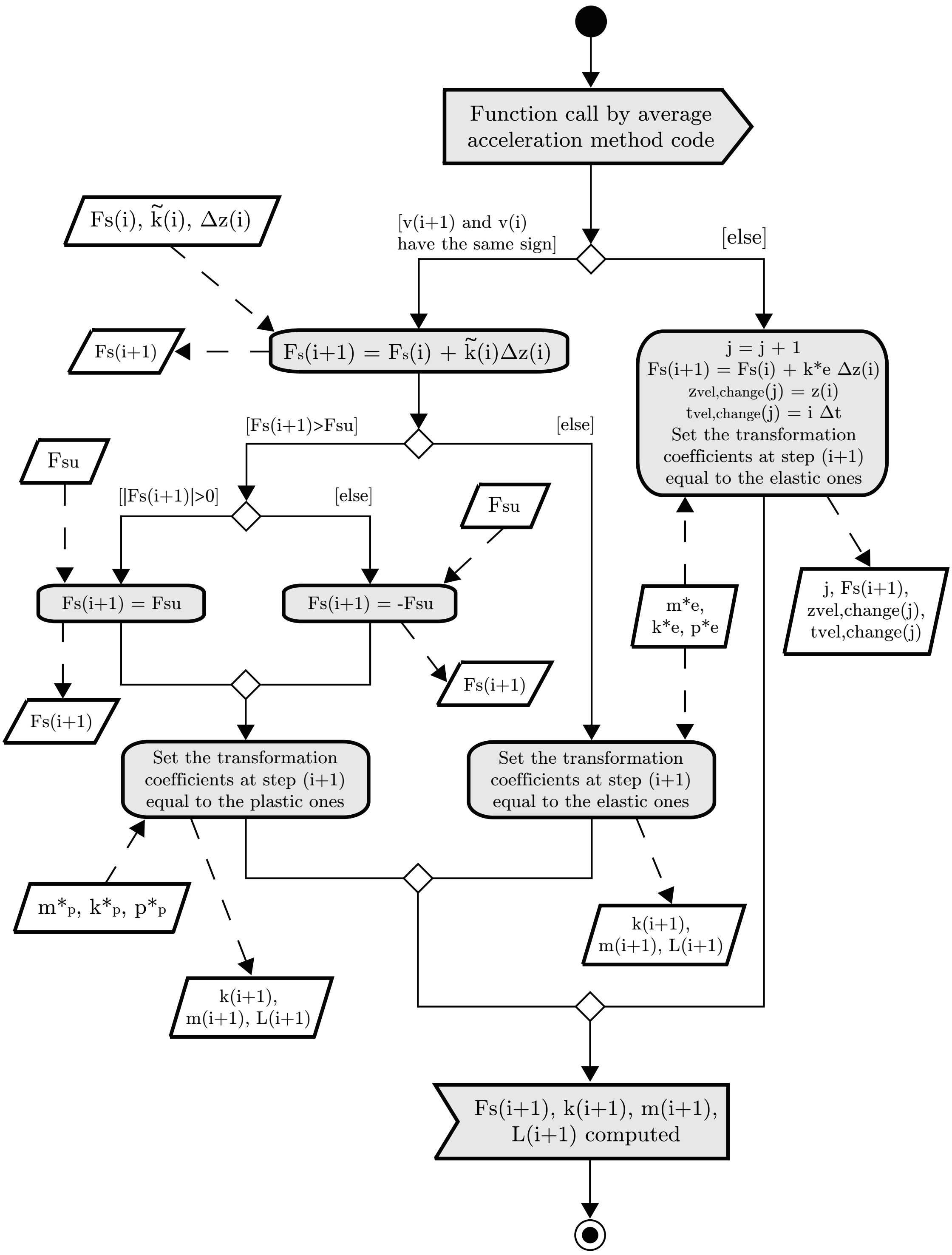

Figure 3.8: Flow chart of the subfunction to compute F_s and the transformation coefficients at the $i+1$-th time-step.

Chapter 4

Pressure-impulse diagrams

4.1 Generalities

A pressure-impulse diagram (p-i diagram) is a design tool that allows a simplified assessment of the response of a structural component subjected to a specified load (e.g., blast load). When the designer defines a maximum value of a certain response parameter, the diagram indicates the combinations of pressure and impulse that will cause the same damage level in the structural element considered (Krauthammer, 2008). Pressure-impulse diagrams were first developed during the Second World War in the study of buildings damaged by bombs in the United Kingdom, and then these p-i diagrams have been applied to predict structural damage as well as human injuries induced by a blast explosion (Shi et al., 2008).
Usually p-i diagrams for structural elements have been derived from the analysis of SDOF systems, assuming a flexural mode of response without any consideration of damage due to shear failure. Moreover, analytical p-i curves were often developed hypothesizing idealized perfectly elastic or elastic-perfectly plastic materials (Krauthammer et al., 2008).
Many authors have been using the SDOF approach (Fischer and Hring, 2009; Li and Meng, 2002a; Morison, 2006), while others have tried to introduce some improvements, using both analytical and numerical procedures. Campidelli and Viola (2007) proposed an analytical method to analyse SDOF models, whilst Fallah and Louca (2007) studied the elastic-plastic-hardening and softening of SDOF system subjected to blast loading, and other constitutive models were considered by Ma et al. (2007). Furthermore, Park and Krauthammer (2009) developed a two-degree-of-freedom model for roof frame under airblast loading, and many more complex method were introduced, either by using numerical simulation (Zhou et al., 2008) or by assuming different failure modes (Ngo and Mendis, 2009). Scherbatiuk et al. (2008) developed p-i diagrams for a temporary soil wall using an analytical rigid-body rotation model, whilst Gong et al. (2009) carried out a validation study on numerical simulation of RC response to close-in blast with a fully coupled model. Concerns in blast-resistant design by means of pressure-impulse diagrams have also been tackled by Alaoui and Oswald (2007) considering precast and prestressed structures; El-Dakhakhni et al. (2009) focused on the capacity assessment of RC columns subjected to blast;

Lan et al. (2005) and Li et al. (2009) studied composite structural elements subjected to explosive loadings, whilst Lan et al. (2005) considered fibre reinforced plastic slabs tackling the problem of the retrofitting of blast damaged structures.
Figure 4.1 shows a sketch of a generic p-i diagram. The two asymptotes define limiting values for each parameter. Loads with very short duration with respect to structure's natural frequency are called impulsive loading and in this case the structure is sensitive only to the related impulse and not to the peak pressure (Shi et al., 2008). Therefore the impulsive asymptote represents the minimum impulse required to reach a certain damage level, and it is approached asymptotically by the p-i curve at high pressures. When the load duration is longer than the structure's natural frequency, a so-called quasi static loading occurs, meaning that the response parameter becomes insensitive to impulse (i.e., to the dynamic nature of the loading) but very sensitive to peak pressure (Shi et al., 2008). Thus the quasi-static asymptote defines the minimum peak pressure required to reach a specified damage level.
In recent years a great progress has been made in developing p-i diagrams of structural members. It appeared that there is a noticeable loading shape influence on the p-i curve when both pressure and impulse are important for the dynamic structural response (Shi et al., 2008), and this occurs in the dynamic loading regime, as can be seen in figure 4.1. Moreover, the influence of the pulse shape effects have been analysed (Florek and Benaroya, 2005), also with particular reference to pressure-impulse diagrams (Li and Meng, 2002b).

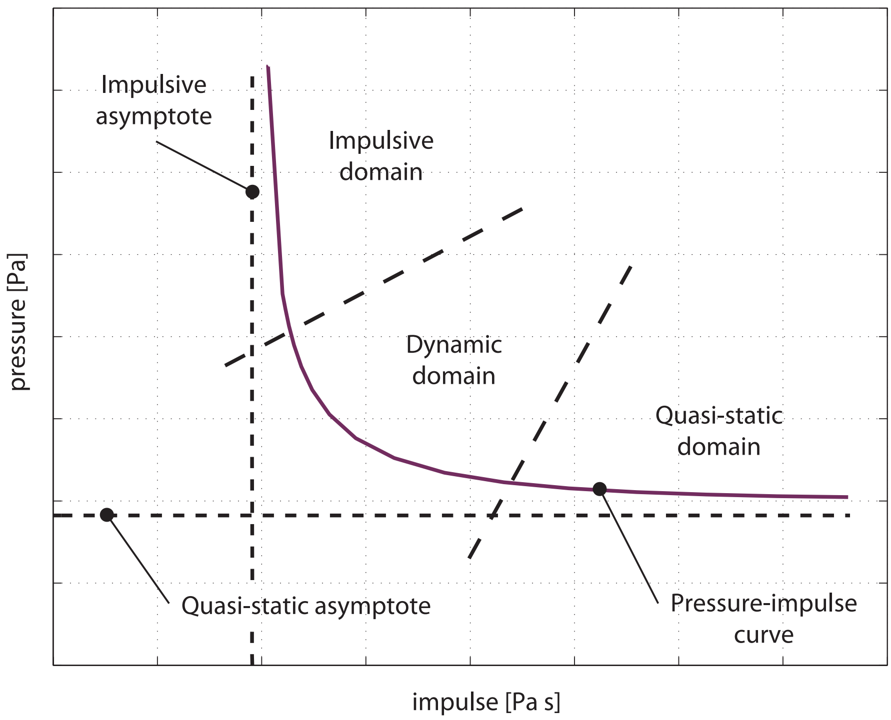

Figure 4.1: A scheme of a typical pressure-impulse diagram.

4.2 Background

In the design of protective structures, non-periodic or non-harmonic loads that act for a finite duration are often encountered. The transient loads are commonly generated in blast or impact events and these loads are usually defined in terms of peak load (pressure or force) and impulse (instead of duration) (Krauthammer, 2008).
The impulse i of the load is defined as the area enclosed by the pressure-time curve (termed generically by $p(t)$), as illustrated in figure 4.2, and its magnitude is given by the following expression:

$$i = \int_0^{t_d} p(t)\mathrm{d}t \tag{4.1}$$

where $p(t)$ is the load-time curve and t_d is the time duration of the load pulse. If $p(t)$ is expressed in term of pressure, specific impulse becomes an appropriate term.

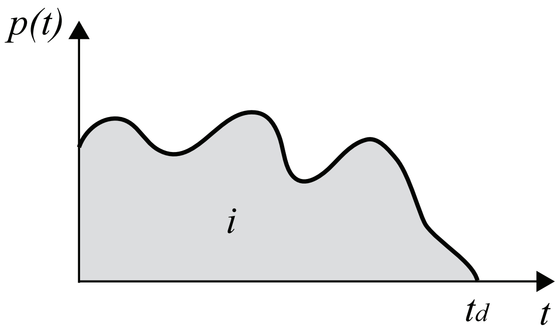

Figure 4.2: The impulse is defined as the area under the pressure-time curve.

When dealing with the preliminary assessment of structural components, a designer is mainly interested in the maximum responses (displacement and stresses), rather than in a detailed knowledge of the response histories (Krauthammer, 2008). Response spectra are plots of the maximum peak response versus the ratio between the load duration and the natural period of the system, and usually they are are used to simplify the design of a dynamic system for a given loading.
By defining different sets of axes, the same response spectra for the given dynamic system can be represented in different ways (Krauthammer et al., 2008). The p-i diagram is one of this alternative representations and it is widely used for structural component damage assessment. By changing the axes one can obtain several forms of shock spectra which may look different; however, all of them describe the relationship between the maximum value of a response parameter and a dynamic characteristic of the system under consideration (Krauthammer, 2008).
The British performed the first applications of p-i diagrams using empirically derived diagrams for brick houses which were bombed during the Second World War in order to determine damage criteria for other houses, small office buildings, and light framed industrial buildings (Krauthammer, 2008). Currently, the

results of such investigations are used as the bases for explosive safe stand-off criteria in the United Kingdom (Baker et al., 1983). Pressure-impulse diagrams were also developed to assess human responses to blast loading and to establish damage criteria to specific organs (eardrum, lungs, etc.) of the human body. This is possible because the body responds to blast loading as a complex mechanical system (Baker et al., 1983).
Pressure-impulse diagrams have been used widely to perform preliminary damage assessments of protective structures subjected to blast loading. It should be noticed that the p-i diagram should be more correctly referred to as a load-impulse diagram, because the ordinate can be defined either in terms of pressure or force; in the latter case, the force-impulse term becomes appropriate (Krauthammer et al., 2008). Traditionally, in specific applications for blast-loaded structures, these load-impulse diagrams appear often with pressure (rather than force) as the ordinate because usually the (blast) load is defined in term of pressure distribution (Krauthammer, 2008).
Pressure-impulse diagrams are also becoming widely used in the homeland security and civil protection fields, and more generally in all those fields in which risk analyses are involved. Asprone et al. (2010) proposed a probabilistic model for the risk assessment of structures in seismic zones subjected to blast; Low and Hao (2001) performed reliability analysis of reinforced concrete slabs under explosive loading; Stewart and Netherton (2008) assessed the risk of glazing subjected to blast loads, whilst Talaslidis et al. (2004) tackled the risk analysis of industrial structures under extreme transient loads. Among these studies, also stochastic techniques were proposed (Wang and Tan, 1995), and in some of them also the effects related to the shear force were taken into account (Low and Hao, 2002).

4.3 Characteristics of p-i diagrams

A p-i diagram emphasizes the combination of peak load and impulse (or equivalent dimensionless quantity) for a given response (or damage level) (Baker et al., 1983). A p-i diagram, also called an iso-damage curve, allows the easy assessment of the response of a structural element to a specified load. With a maximum displacement or damage level defined, a p-i curve indicates the combinations of load or pressure and impulse that will cause the specified failure or damage level (Krauthammer, 2008). Actually the threshold curve divides the p-i diagram into two distinct regions. Combinations of pressure and impulse that fall to the left and below the curve will not induce failure, while those falling to the right and above the graph will produce damage exceeding the allowable limit (i.e., the selected damage threshold). It is well known from structural dynamics that a strong relationship exists between the natural frequency (which directly influences the response time) of a structural element and the duration of the forcing or load function (Biggs, 1964; Clough and Penzien, 1993). This relationship is normally categorized into three regimes: impulsive, quasi-static, and dynamic (Baker et al., 1983). With respect to the response spectrum, the p-i representation better allows to tell the difference between the impulsive and quasi-static domains (Krauthammer et al., 2008). These domains will be discussed in more detail in the following section, since they are important in the development of p-i diagrams by means of the energetic approach.

4.4 Loading regimes

In the impulsive loading regime, the load duration is short relative to the response of the system (which is influenced by the system natural frequency). Actually, the load is applied to the structure and removed before the structure can undergo any significant deformation, as shown in figure 4.3.a. Therefore the maximum response (reached at time t_m) can be assumed to be independent of the load time history, meaning that the maximum response is mainly affected by the impulse.
For the quasi-static regime, the loading duration is significantly longer than the response time. The load dissipates very little before the maximum deformation or resistance is achieved at time t_m (figure 4.3.b). Unlike the impulsive regime, the response in the quasi-static regime depends only upon the peak load and structural stiffness. However, as with the impulsive regime, the maximum response is not affected by the loading history.
A third transition regime, known as the dynamic regime, exists between the impulsive and quasi-static regions. In this domain, the loading duration and the time to reach the maximum response of the system are approximately the same or of the same magnitude, as shown in figure 4.3.c. The response analysis in this loading regime is more complex and it is significantly influenced by the load history.

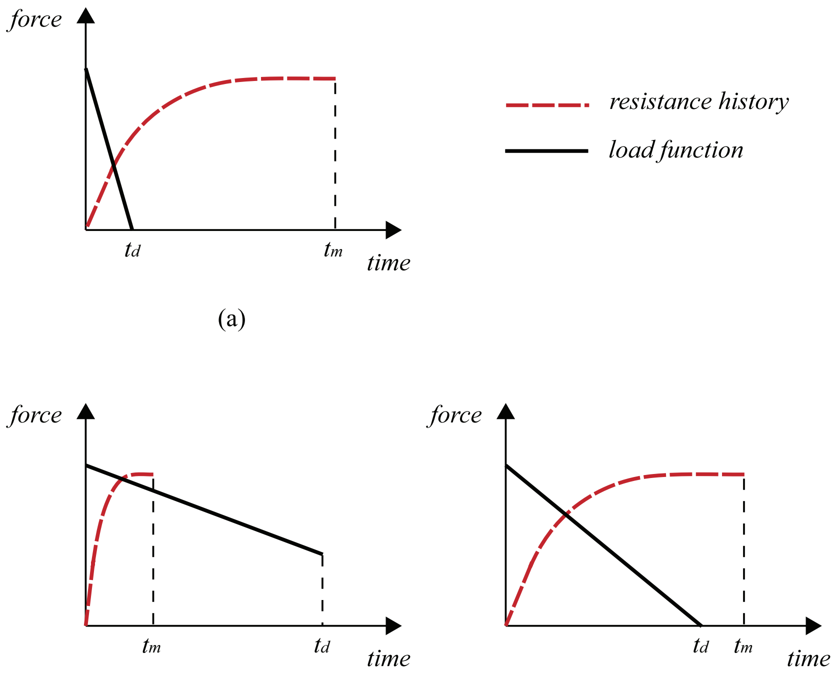

Figure 4.3: Typical response domains: (a) impulsive; (b) quasi-static and (c) dynamic regimes.

4.5 Asymptotes: an energetic approach

A widely used approach for obtaining the asymptotes is the energy balance method (Krauthammer, 2008). This approach, based on the principle of conservation of mechanical energy, is convenient to apply because two distinct energy formulations always exist that separate the impulsive loading regime from the quasi-static loading regime.
To obtain the impulsive asymptote, it can be assumed that due to inertia effects the initial total energy imparted to the system is in the form of kinetic energy only (Krauthammer, 2008). Equating this to the total strain energy stored in the system at its final state (maximum response), one obtains an expression for the impulsive asymptote:

$$K.E. = S.E. \tag{4.2}$$

where $K.E.$ is the kinetic energy of the system at time zero, $S.E.$ is the strain energy of the system at maximum displacement.
For the quasi-static loading regime, the load can be assumed to be constant before the maximum deformation is achieved. By equating the work done by load to the total strain energy gained by the system, the expression for the quasi-static asymptote is obtained (Krauthammer et al., 2008):

$$W.E. = S.E. \tag{4.3}$$

where $W.E.$ is the maximum work done by the load to displace the system from rest to the maximum displacement.
The formulae related to circular plates and in particular to the cases under study will be worked out in chapter 5.

4.6 Pressure-impulse diagram development algorithm

Pressure-impulse diagrams can be worked out numerically by generating a sufficient number of computed points to allow curve fitting (Krauthammer, 2008). Each point represents the result from a single dynamic analysis and indicates that the structure has reached a specific response (usually a displacement) relative to a certain combination of pressure and impulse. Since running all possible pressure and impulse combinations is computationally very expensive, a search algorithm must be employed to locate the threshold points that define the transition from safe to damaged states. Unlike analytical solutions, numerical approaches allow complex non-linear resistance functions and complex loading functions to be used (Krauthammer et al., 2008). Furthermore, the numerical approach can describe the behaviour of the p-i curve in the dynamic response domain accurately (Krauthammer, 2008).

Blasko et al. (2004) used a polar coordinate system and the bisection method to obtain p-i diagrams. The numerical procedure starts with locating a pivot point of coordinates $(i_0; p_0)$ in the failure zone, which is set as the origin of the polar coordinate system. Iterations using the bisection method are carried out to find the threshold point for each angle ϕ_i. This method is smart because, by exploiting polar coordinates instead of rectangular coordinates, allows to use only a single search direction.

It should be noticed that the derivation of the p-i curve, which is performed in a numerical way, is independent from the computation of the asymptotes, which is done, on the contrary, in an analytical way by means of the energetic approach. However, the asymptotes can give rise to a convenient starting point for the numerical procedure. In fact, although the calculation of the asymptotes is not necessary for the numerical method to work, one can automate the procedure for selecting the location of the pivot point by utilizing the asymptotes (Krauthammer et al., 2008). The best choice for locating the pivot point is to consider it as an homothetical dilation of the point of intersection between the two asymptotes, since the points along this line are expected to be equally distanced from both the asymptotes (see figure 4.4). A randomly selected point might be close to one asymptote or too far from the threshold curve, reducing the resolution of the results. This approach can be applied effectively to any structural system for which a resistance function can be obtained (Krauthammer et al., 2008).

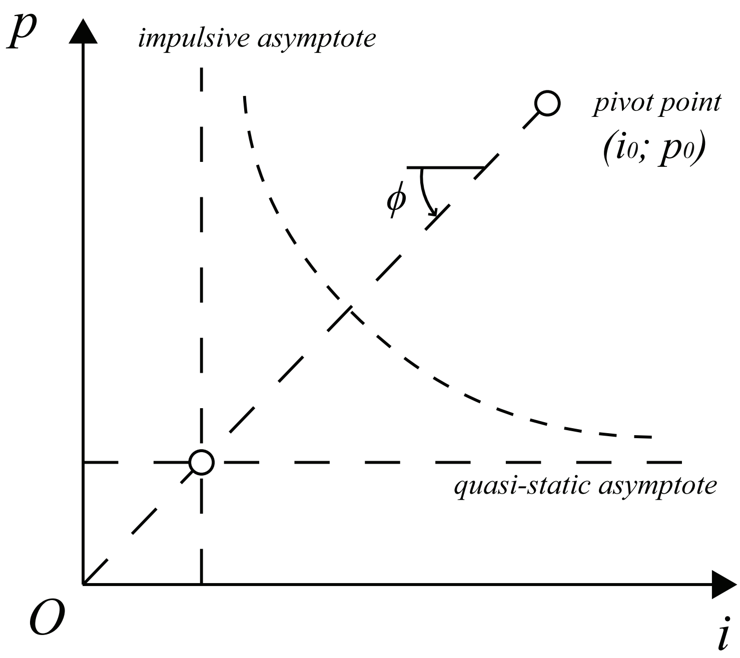

Figure 4.4: Location of the pivot point.

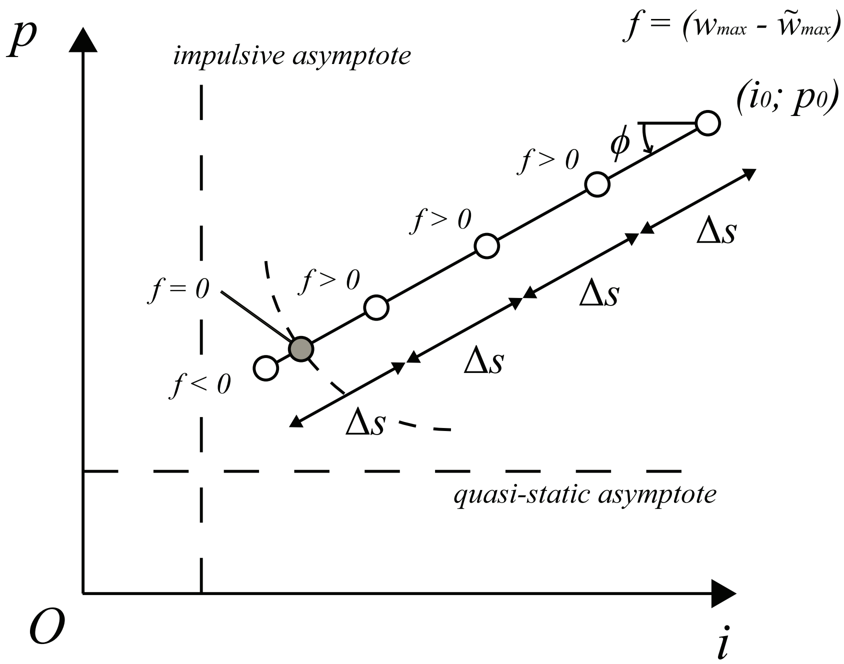

Figure 4.5: Scheme of the p-i diagram development algorithm.

4.6.1 Outline of the procedure

In order to generate the p-i curve, for every direction ϕ_i arising from the pivot point $(i_0; p_0)$ the following procedure is carried out:

- the algorithm moves downward along the direction ϕ_i with a chosen spatial step Δs evaluating the sign of the function $f = (w_{max} - \widetilde{w}_{max})$ in each point of the discretization. In this expression, w_{max} represents the maximum displacement in the time history obtained from a dynamic analysis performed under the combination of pressure and impulse given by the coordinates of the current point; while $\widetilde{w}_{max}$ represent the damage threshold computed according to the criterion that will be discussed in the following chapter. This searching procedure stops when the sign of f becomes negative, meaning that an interval suitable for the application of the bisection method is found, because the damage threshold falls inside such interval (see figures 4.5 and 4.6);
- from now on, the bisection method is applied and iterated until the desired level of precision is achieved according to a certain convergence criterion (see figure 4.7).

For the j-th iteration, the point $M = (i_M; p_M)$ represented in figure 4.7 (which is the middle point of the segment $\overline{AB}$) is computed, and a dynamic analysis is performed in order to find $w_{max,M}$. Therefore one can compute $f_M = (w_{max,M} - \widetilde{w}_{max})$. For the subsequent iteration, the algorithm must choose the interval which repeats the same sign configuration as the previous one, i.e., if the value given by the product $f_M \cdot f_A$ has a negative sign, then one must take the $\overline{MA}$ interval, otherwise the $\overline{MB}$ interval must be chosen. Then the same procedure is iterated until the desired convergence is reached.
A suitable convergence criterion may be based on the evaluation of the following discrepancy at every j-th iteration:

$$\varepsilon_j = \frac{w_{max,j} - \widetilde{w}_{max}}{\widetilde{w}_{max}} \tag{4.4}$$

with ε_j being the error of convergence at the j-th iteration and $w_{max,j}$ the maximum displacement provided by the dynamic analysis performed at the j-th iteration. When ε_j is minor than a certain value assumed as the precision of the numerical computation (e.g., when $< 1\%$) the desired level of convergence is reached and the iterative procedure stops.

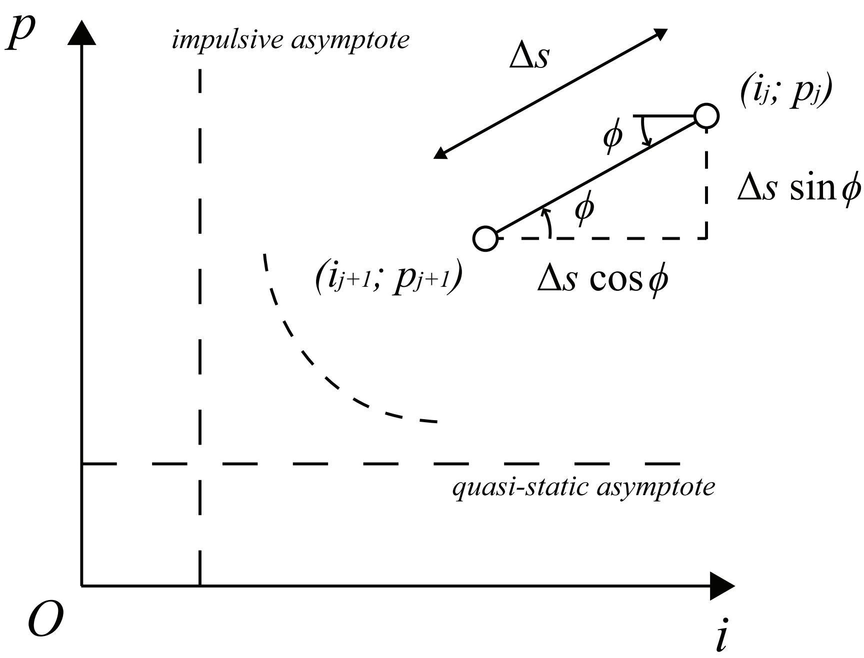

Figure 4.6: Scheme of the p-i search method.

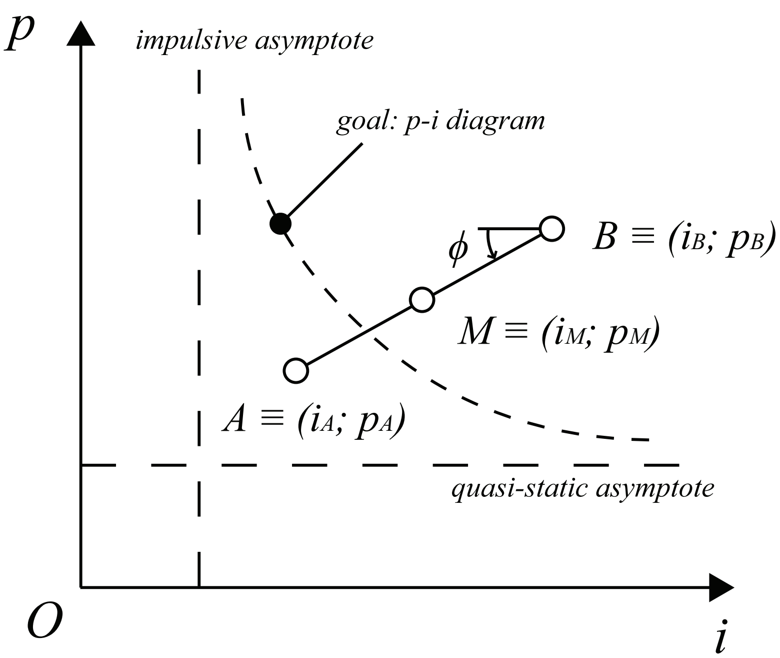

Figure 4.7: Scheme of the bisection method.

While performing the numerical simulations during this work, it was encountered a problem in the graphical resolution of the p-i curves. In fact, too many points appeared to interpolate the upper part of the curve, while the resolution of the lower part, mainly in correspondence with the dynamic loading regime, looked very poor.
In order to address this issue, it was decided to compute two different sectors of the diagram in a separate way: the upper left sector, in which there will be the part of the p-i curve closest to the the impulsive asymptote, and the lower right sector, in which there will be the part of the p-i curve closest to the quasi-static asymptote. In this way, the user may choose to compute the first sector with a lower number of points, and the second sector with a higher number of points, or vice-versa, according to the level of resolution desired. This gives rise to the possibility to speed up the computational procedure reducing the numerical effort, and it has proven to be very efficient.
In order to automate the procedure, the angle which separates the two sectors (called α) was chosen to be equal to the one obtained by joining the pivot point and the midpoint of the segment lying on the impulsive asymptote which has as endpoints the point of intersection between the asymptotes and the point with the same ordinate as the pivot point, as illustrated in figure 4.8.
The mathematical form of angle α is the following:

$$\alpha = \arctan\left(\frac{p_0 - \dfrac{p_0 - q.s.a.}{2}}{i_0 - i.a.}\right) \tag{4.5}$$

$$= \arctan\left(\frac{q.s.a. + p_0}{2(i_0 - i.a.)}\right) \tag{4.6}$$

where $i.a.$ is the level of impulse at which the impulsive asymptote is located, while $q.s.a.$ is the level of pressure at which the quasi-static asymptote is located. Recalling that the pivot point $(i_0; p_0)$ is given by the homothetic transformation of the point of intersection between the asymptotes $(i.a.; q.s.a.)$ through the expansion factor k (which is > 1), expression 4.6 can be finally rewritten as:

$$\alpha = \arctan\left(\frac{q.s.a.\,(1+k)}{2\,i.a.\,(k-1)}\right) \tag{4.7}$$

It should be noticed that the p-i diagrams plotted in this work have dimensional axes, while usually p-i diagrams performed in other works are plotted with non-dimensional axes in order to obtain comparable scales. Plotting dimensional p-i diagrams has its advantage, because the user can apply these diagrams in a direct way, just placing a point representing the desired conditions of pressure and impulse inside the p-i diagram. However, since the ratio between the vertical and the horizontal axis is very big, traditional algorithms cannot trace the complete curve. Therefore this work proposed a modification of the traditional algorithms in order to achieve a complete and well defined curve. This improvement makes the results more useful in practice.

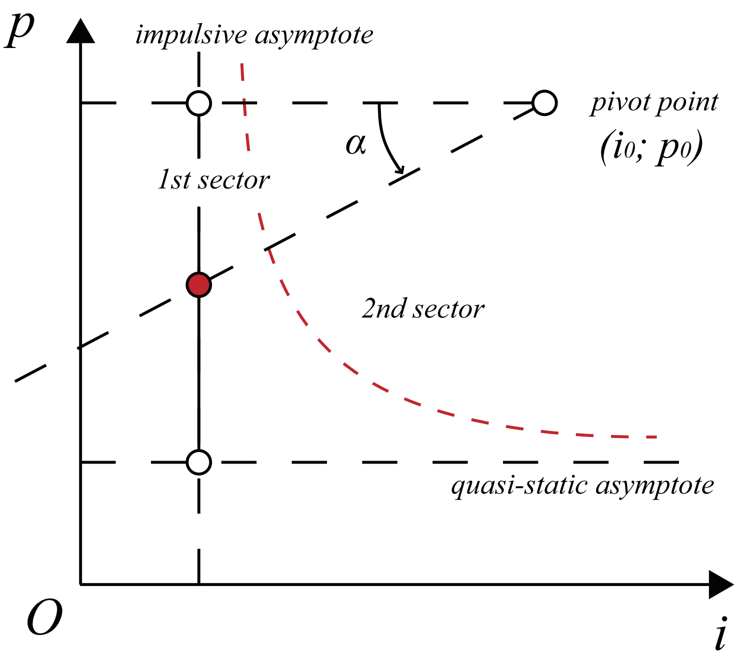

Figure 4.8: Sketch of the angle α between the two sectors of computation.

4.7 Flow charts of the MATLAB® code

In these pages the schematic flow charts of the numerical codes developed to obtain the p-i curves will be presented. The notation in which the flowcharts herein reported were developed is based upon the Unified Modelling Language (UML) contained in the book *UML Distilled Third Edition* (Fowler, 2003), amongst the other authors.

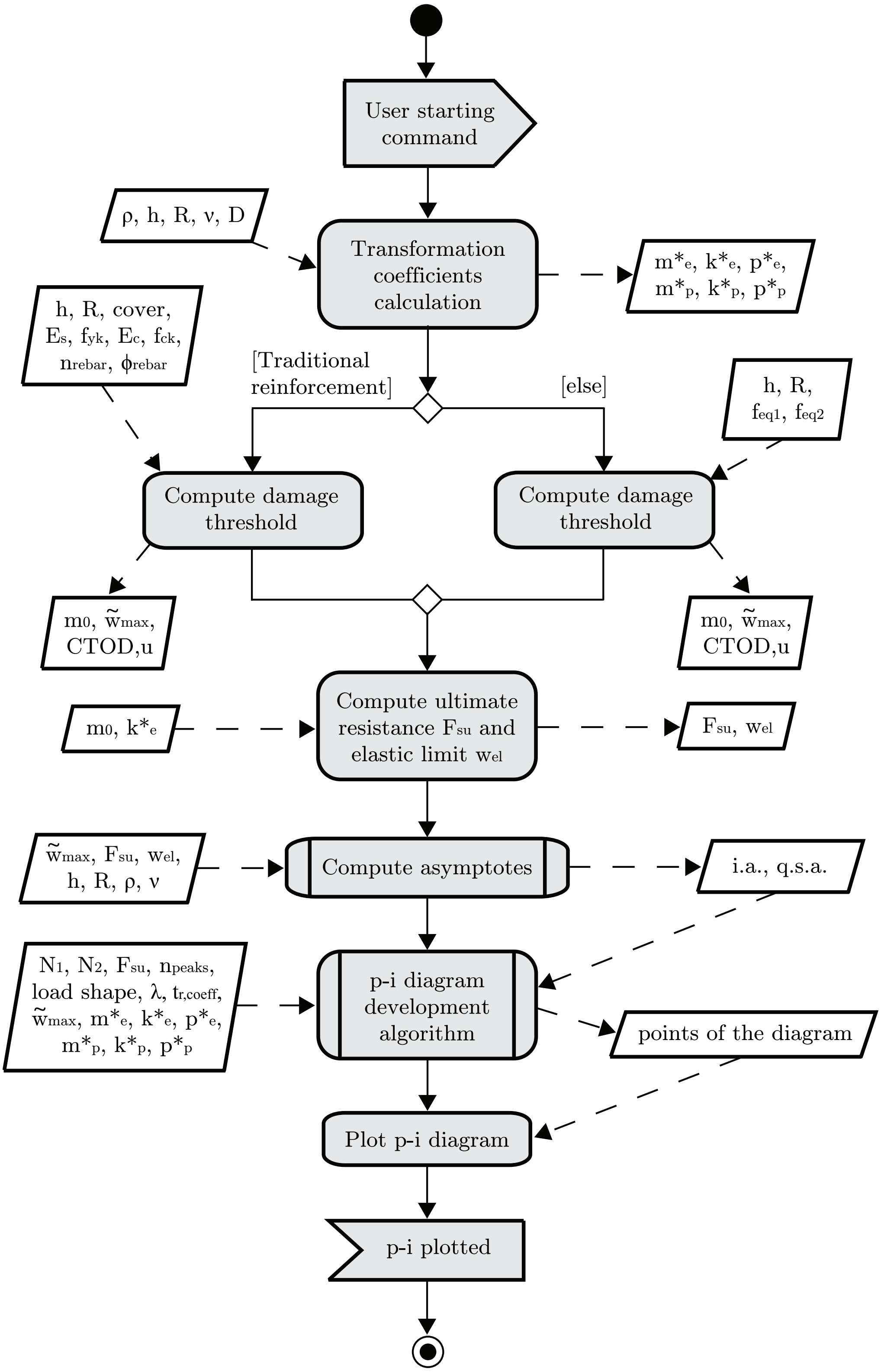

Figure 4.9: Flow chart of the p-i diagram main code.

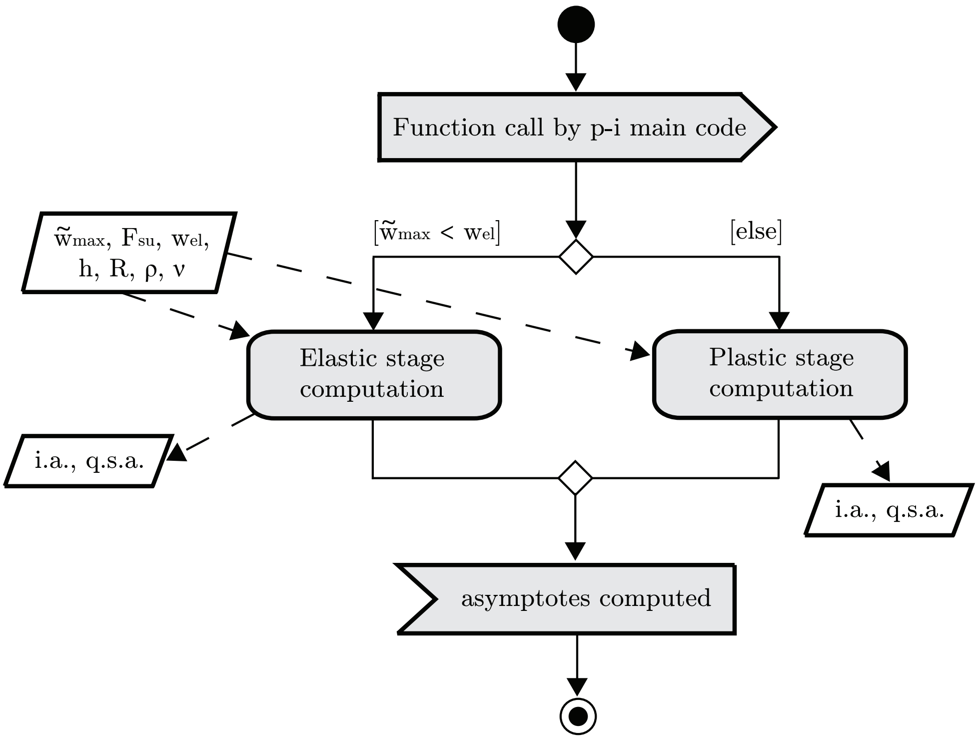

Figure 4.10: Flow chart of the asymptotes code.

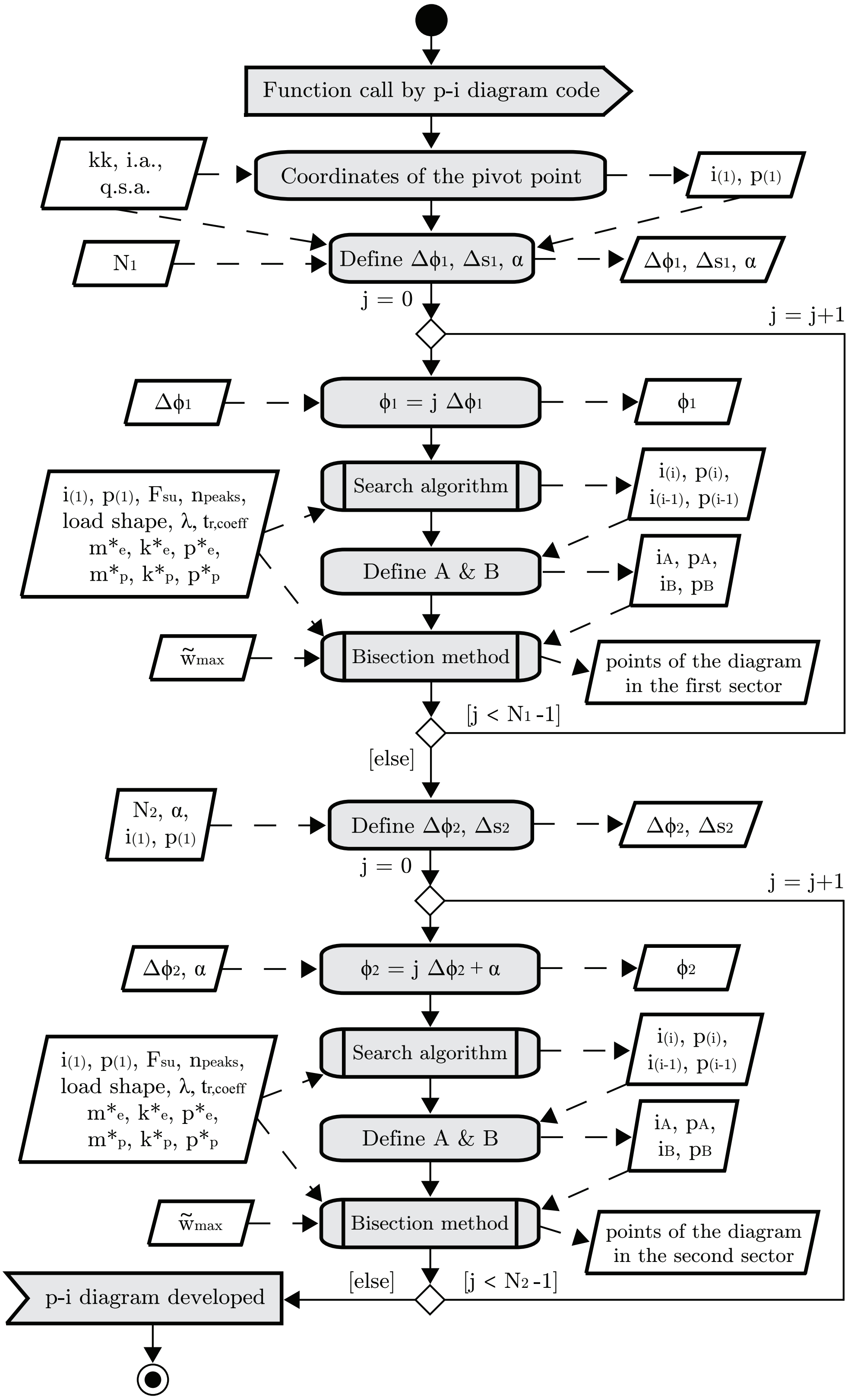

Figure 4.11: Flow chart of the p-i diagram development code.

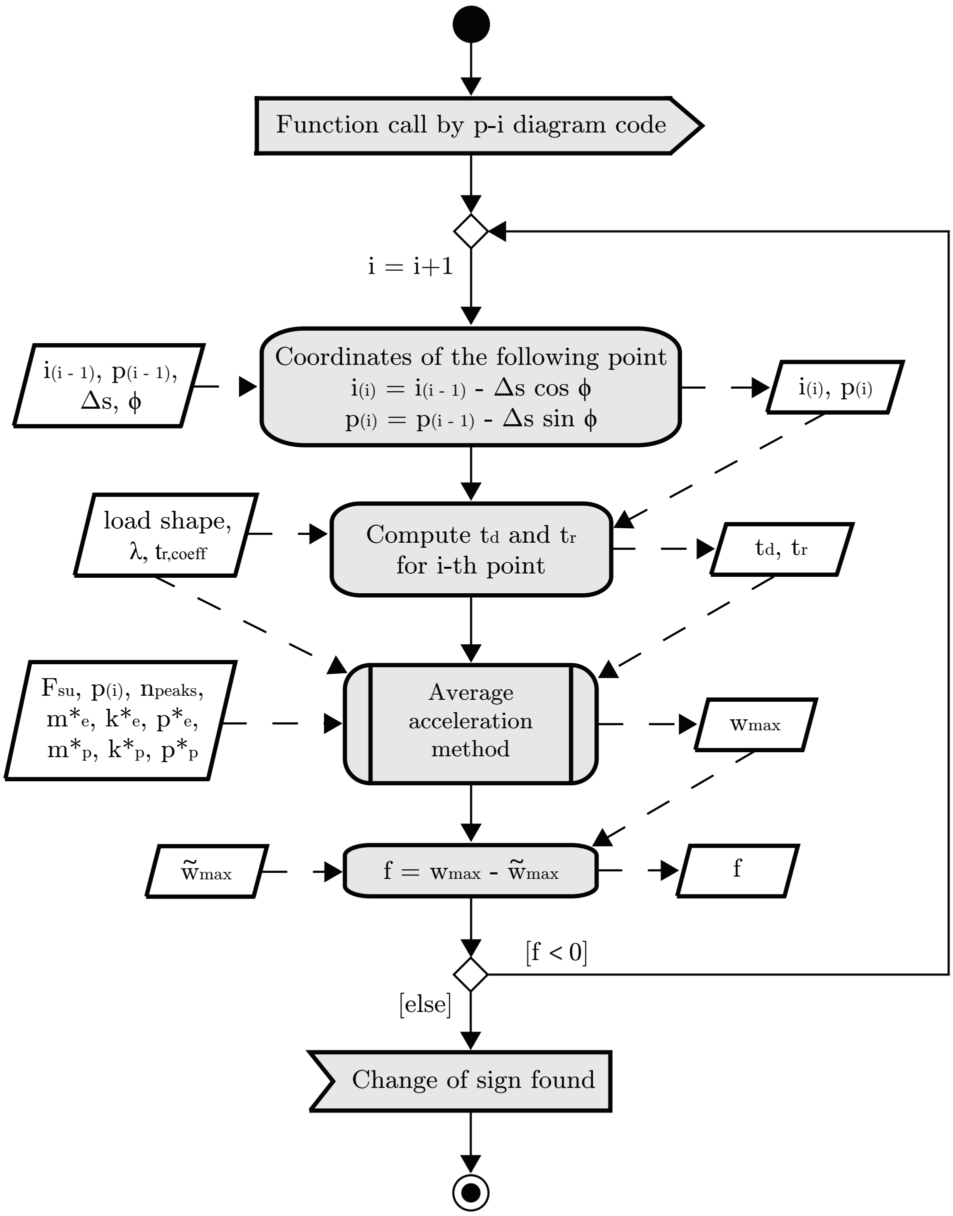

Figure 4.12: Flow chart of the p-i search algorithm code.

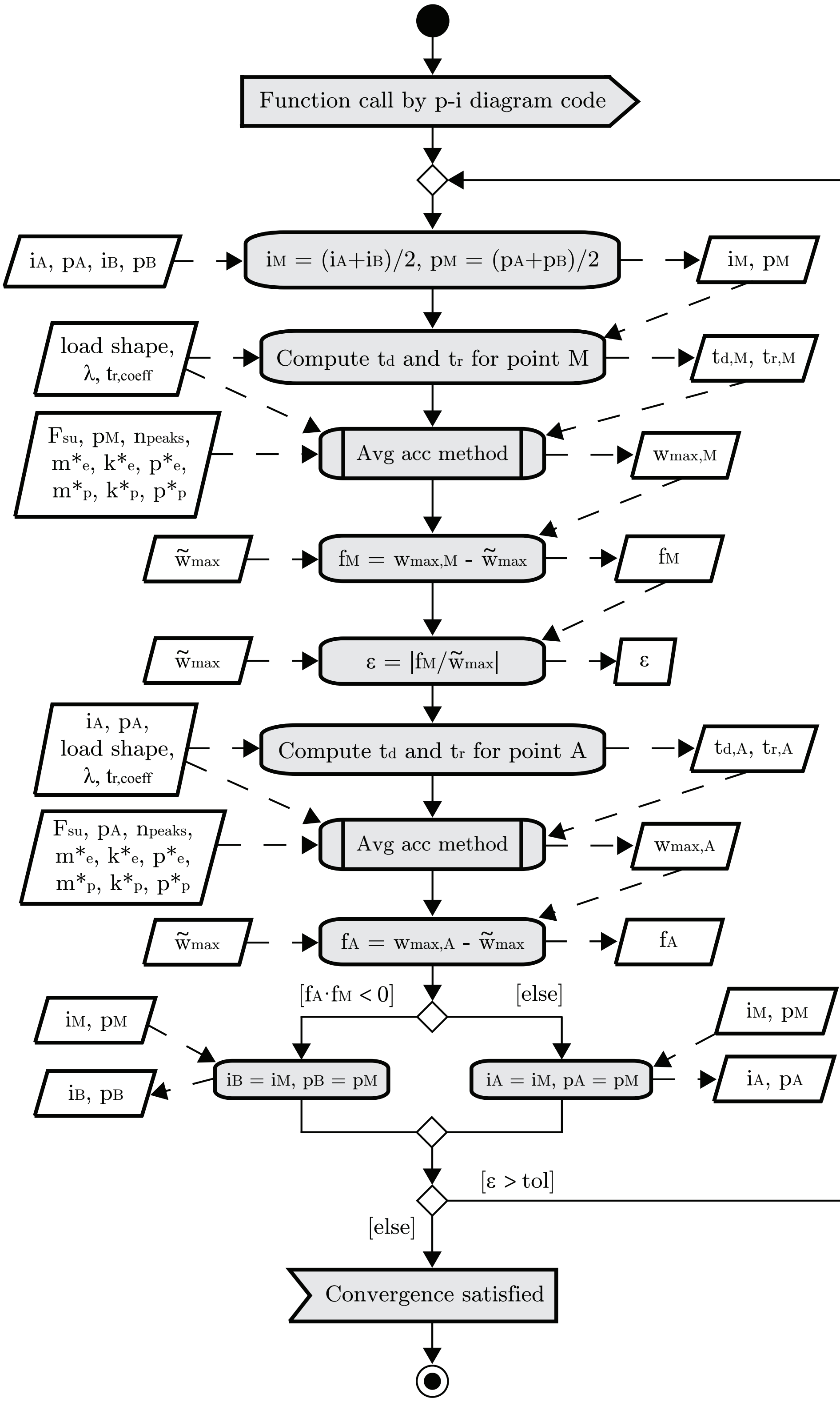

Figure 4.13: Flow chart of the p-i bisection method.

Chapter 5

Applications

The algorithms developed in this paper can be used for general applications of dynamic analysis and p-i diagrams. However, there are some specific applications of interest to achieve the scope of this project. In this chapter circular plates are considered in order to forecast the experimental results of the shock tube test. Of course, shock tube samples should have certain geometrical characteristics of thickness h and radius R and that is why the examples and the results worked out in this chapter correspond to the shock tube plate samples. Many kinds of material could be considered in the analysis, but just two wide known materials were selected, reinforced concrete (RC) and fibre-reinforced concrete (FRC). Civil engineers are very familiar with these materials and the results will be clearer if these materials are involved instead of others like layered structure, which is left for further research.
Not only different materials are taken into account, but also different boundary conditions, like plates simply supported or supported on grade. Thereby, the application's field of the work developed herein becomes wider, including a lot of possible circumstances in terms of materials and boundary conditions.

5.1 Materials adopted

Two kinds of material will be considered in the applications which will be later presented in this chapter: high strength concrete reinforced with traditional steel bars and a fibre-reinforced concrete (Colombo et al., 2010).
In this section the two kinds of reinforcement will be briefly reviewed, along with the ultimate bending moment and the damage threshold calculations which will turn to be necessary for the subsequent applicative examples.

5.1.1 Traditional reinforcement

Ultimate bending moment resistance

The design yielding strength of steel is given by the characteristic yielding strength divided by a safety factor equal to 1.15:

$$f_{yd} = \frac{f_{yk}}{1.15} \tag{5.1}$$

The design yielding strain of steel is given by the Hooke's law:

$$\varepsilon_{yd} = \frac{f_{yd}}{E_s} \tag{5.2}$$

The design ultimate strain of steel is conventionally set equal to:

$$\varepsilon_{sd} = 1\% \tag{5.3}$$

The design ultimate strength of concrete is given by the characteristic cylindrical compressive strength divided by a safety factor equal to 1.5:

$$f_{cd} = \frac{f_{ck}}{1.5} \tag{5.4}$$

The ultimate stress of concrete must be further reduced by means of a coefficient which takes into account the long term load fatigue effects:

$$f_{cu} = 0.85\, f_{cd} \tag{5.5}$$

Even though within this work the discussion is mainly concerned about short duration load, the coefficient for fatigue effects was taken into account because it was thought that the plate is not designed only to resist explosive loads, but also to carry all the actions which occur more frequently.
High strength concrete will be considered in this work, namely concrete having a cylindrical compressive strength greater than 50 MPa. According to the Eurocode 2 (VV.AA., 2004), the ultimate strain of high strength concrete is given by:

$$\varepsilon_{cu} = 0.26\% + 3.5\% \left(\frac{f_{ck} - 90}{100}\right)^4 \tag{5.6}$$

As can be seen in this formula, when f_{ck} increases, the value of ε_{cu} decreases, meaning that the plastic plateau is reduced, thus highlighting the brittle behaviour of a high strength concrete.
The specific steel area per unit length is given by:

$$A_s = n_{rebar} \left(\frac{\pi}{4}\, \phi^2\right) \tag{5.7}$$

with n_{rebar} being the number of reinforcement bars in a unit length base ($b = 1$ m), and ϕ being their diameter.
The geometrical steel ratio is denoted by ρ_s:

$$\rho_s = \frac{A_s}{b\, d} \tag{5.8}$$

where $d = h - c$ is the effective distance (with c being the concrete cover of the reinforcement and h the plate thickness) and $b = 1$ m. The ductility ratio can be computed as follows:

$$\chi_b = \frac{\varepsilon_{cu}}{\varepsilon_{cu} + \varepsilon_{yd}}\, d \tag{5.9}$$

In order to meet the condition of balanced rupture, which ideally represents the best exploitation of the characteristics of both the materials, the following requirement must be satisfied:

$$\rho_s < \frac{0.8\, f_{cu}\, \chi_b}{f_{yd}\, d} \tag{5.10}$$

If this condition is enforced, it is sure that the concrete has reached its ultimate strength at the extreme fibre and that the steel has achieved the yielding condition, which implies $\varepsilon_s \geq \varepsilon_{yd}$ and $\sigma_s = f_{yd}$. In addition to this, also the requirement of a minimum geometrical steel ratio (which is fixed in $\rho_{s,min} = 0.6\%$ by the codes) must be satisfied. If these two conditions are met, one can compute the neutral axis position as follows:

$$x = \frac{f_{yd}\, A_s}{0.8\, f_{cu}\, b} \tag{5.11}$$

Finally the ultimate bending moment resistance per unit length [F·L/L], making reference to figure 5.1, can be computed as follows:

$$m_0 = f_{yd}\, A_s\, (d - x) + 0.8\, f_{cu}\, b\, x\, (0.6\, x) \tag{5.12}$$

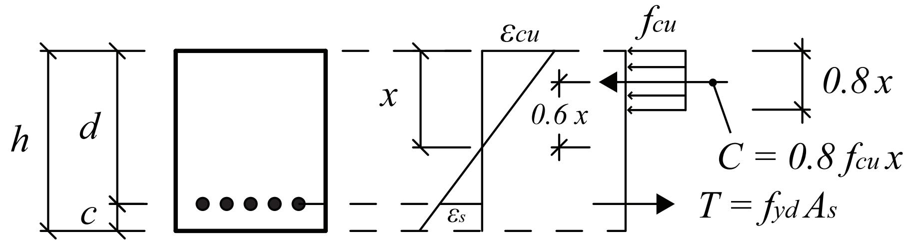

Figure 5.1: RC element undergoing a balanced rupture.

Damage threshold

The threshold displacement criterion is imposed in relation with the crack tip opening displacement ($CTOD$) at midspan. Performing a triangle relation between the rotation at the border with the rotation at midspan, it is possible to obtain the equation 5.13, which relates the crack opening with the ultimate allowable displacement ($\widetilde{w}_{max}$). This geometrical relation is illustrated in figure 5.2. The geometrical relation is valid for RC and FRC, but the definition of $CTOD$ is taken in consideration in a different way, as it is going to be presented along this section.
For RC the selected $CTOD$ corresponds to the post-yielding deformation of the steel bars when the concrete reaches its maximum compressive strength at the extreme fibres.

The damage threshold $\widetilde{w}_{max}$ in the case of traditional reinforcement can be computed as:

$$\widetilde{w}_{max} = R\, \frac{CTOD_u}{2d} \tag{5.13}$$

The corresponding crack opening $CTOD_u$ is given by:

$$CTOD_u = \varepsilon_s\, l_{cs} \tag{5.14}$$

with ε_s being the steel deformation after yielding and l_{cs} the characteristic length, as defined in the following.

The steel deformation ε_s after yielding is given by:

$$\varepsilon_s = \varepsilon_{cu} \left(\frac{d}{x} - 1 \right) \tag{5.15}$$

where $\varepsilon_s \geq \varepsilon_{yd}$, once the ductility condition stated by equation 5.10 has been satisfied.
In presence of traditional reinforcement, the characteristic length l_{cs} can be computed as:

$$l_{cs} = \min(s_{rm}, y) \tag{5.16}$$

where y is the distance between the lower reinforcement and the neutral axis in elastic cracked phase, and s_{rm} is the average distance between cracks, computed as follows (Eurocode 2, VV.AA. (2004); CNR-DT 204/2006):

$$s_{rm} = \xi \left(50 + 0.25\, k_1\, k_2\, \frac{\phi}{\rho} \right) \tag{5.17}$$

where:

- ξ is an adimensional coefficient equal to 1.0;
- k_1 is a coefficient equal to 0.8 for ribbed bars and equal to 1.6 for smooth bars;
- k_2 is a coefficient equal to 0.5 for simple or compound bending with $y \leq h$ and equal to 1.0 for tension or compound bending with $y > h$;
- h is the height of the section;
- ϕ is the steel rebar diameter;
- $\rho = \dfrac{A_s}{b\, y}$ is the geometrical ratio between the steel area A_s and the section area in tension identified by the distance y.

The neutral axis position x in elastic cracked phase is given by:

$$x = m \frac{A_s}{b} \left(-1 + \sqrt{1 + \frac{2\, b\, h}{m\, A_s}} \right) \tag{5.18}$$

where $b = 1$ m, $m = \dfrac{E_s}{E_c}$, with E_s being the steel Young modulus and E_c the concrete Young modulus. For a high strength concrete, the Young modulus can computed with the formula given in Model Code 1990 (CEB-FIP, 1993):

$$E_{ci} = E_{c0} \left[\frac{f_{ck} + \Delta f}{f_{ck0}} \right]^{1/3} \tag{5.19}$$

where:

- $E_{c0} = 21.5$ MPa;
- $\Delta f = 8$ MPa;
- $f_{ck0} = 10$ MPa.

Hence the distance y between the lower reinforcement and the neutral axis in elastic cracked phase is simply equal to:

$$y = d - x \tag{5.20}$$

being d the effective distance and x the neutral axis position as provided by equation 5.18.

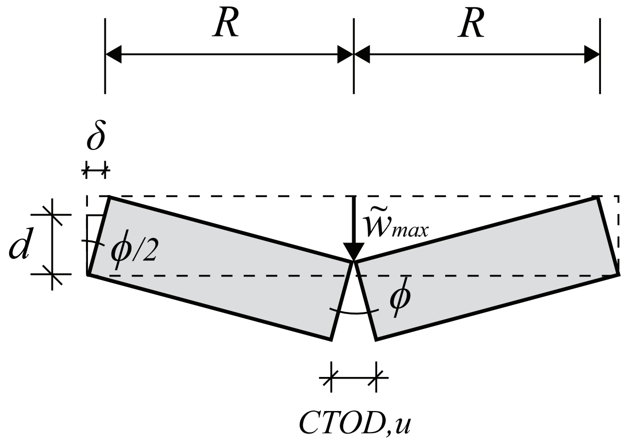

Figure 5.2: Damage criterion for a RC plate.

5.1.2 FRC plate

Ultimate bending moment resistance

The model herein used was illustrated in the document *Istruzioni per la Progettazione, Esecuzione ed il Controllo di Strutture di Calcestruzzo Fibrorinforzato*, VV.AA. (2006) (CNR-DT 204/2006), and it was developed according to Ferrara et al. (2004).

This model assumes that the strength in the post-cracking phase can be de-

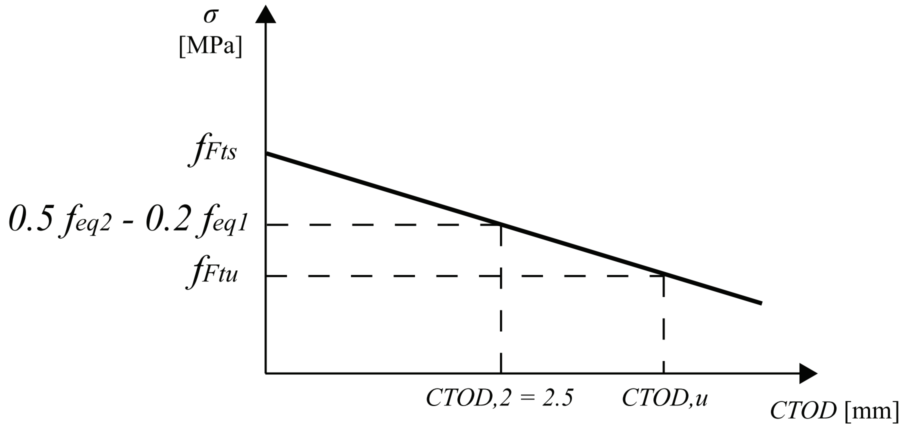

Figure 5.3: FRC constitutive model as proposed in CNR-DT 204/2006.

fined either on the basis of point values corresponding to given nominal values of crack opening or on the basis of mean values $f_{eq,i}$ computed in a given interval of crack opening (see figure 5.3). In the case of a notched specimen, the crack opening can be conventionally assumed to be equal to the displacement between two points at the tip of the notch, $CTOD$ (CNR-DT 204/2006).
In the following applications, the average nominal strengths $f_{eq,i}$ were assumed to be equal to: $f_{eq,1} = 5.34$ MPa and $f_{eq,2} = 3.91$ MPa, according to Colombo et al. (2010).
The crack opening $CTOD_u$ in the case of an FRC plate is given by:

$$CTOD_u = \min(3 \text{ mm}, \varepsilon_{Ftu}\, l_{cs}) \tag{5.21}$$

In the case of a FRC plate the characteristic length l_{cs} is equal to the slab thickness:

$$l_{cs} = h \tag{5.22}$$

The ultimate tensile strain of the FRC is equal to:

$$\varepsilon_{Ftu} = 2\% \tag{5.23}$$

The residual characteristic tensile strength at serviceability limit state is:

$$f_{Ftsk} = 0.45\, f_{eq1} \tag{5.24}$$

The ultimate characteristic tensile strength of the FRC is:

$$f_{Ftuk} = f_{Ftsk} - \frac{CTOD_u}{CTOD_2}\,(f_{Ftsk} - 0.5\, f_{eq2} + 0.2\, f_{eq1}) \tag{5.25}$$

with $CTOD_2 = 2.5$ mm.
The design ultimate tensile strength is obtained as a reduction of the characteristic value by means of a safety factor which is equal to 1.3 for a displacement controlled test:

$$f_{Ftud} = \frac{f_{Ftuk}}{1.3} \tag{5.26}$$

The residual design tensile strength at serviceability limit state is given by:

$$f_{Ftsd} = \frac{f_{Ftsk}}{1.3} \tag{5.27}$$

Finally the ultimate bending moment resistance [F·L/L], making reference to figure 5.4, can be computed as follows:

$$m_0 = f_{Ftud}\,\frac{h^2}{2} + (f_{Ftsd} - f_{Ftud})\,\frac{h^2}{6} \tag{5.28}$$

As last remark, it should be noticed that also the value of the FRC elastic modulus is needed, in order to calculate the flexural rigidity D. For a fibre reinforced concrete, the value of the Young modulus is generally little influenced by the fibres, thus it can be set equal to the one of the concrete matrix (CNR-DT 204/2006). In the applications of this chapter it will be assumed for the characteristic cylindrical compressive strength of the concrete matrix a value of 75 MPa, meaning high strength concrete, thus the Young modulus will be computed according to equation 5.19.

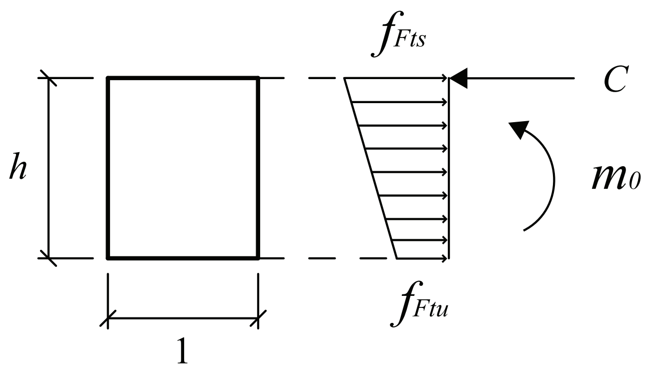

Figure 5.4: FRC reinforcement: calculation of the ultimate bending moment m_0.

Damage threshold

The same procedure, already explained for RC damage threshold, is applied in this case, defining $CTOD$ with equation 5.21. With reference to figure 5.5, the damage threshold $\widetilde{w}_{max}$ in the case of a plate made in fibre reinforced concrete can be computed as:

$$\widetilde{w}_{max} = R\,\frac{CTOD_u}{2h} \tag{5.29}$$

This equation originates from the same geometrical relation that was discussed for the RC damage threshold.

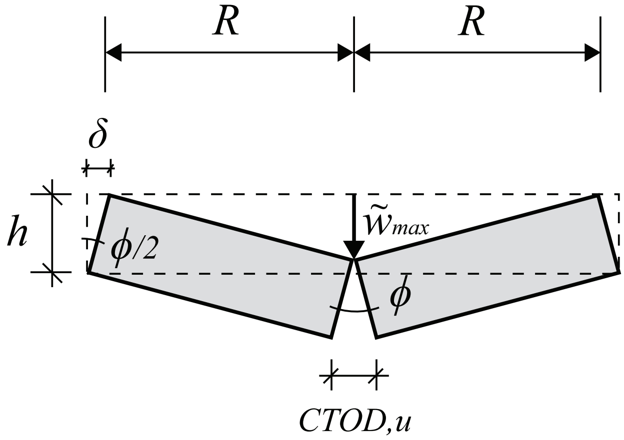

Figure 5.5: Damage criterion for a FRC plate.

5.2 Case 1: simply supported circular slab

Consider a simply supported circular slab of radius R subjected to an axis-symmetric load p_0 distributed over the entire slab area, as illustrated in figure 5.6. The origin of the reference system is taken at the slab center, thus the abscissa r varies from 0 to R, as can be seen in figure 5.7. The elastic deflected shape is denoted as $w(r)$, and w_{max} is the maximum displacement, which is reached at the plate center and represents the generalized SDOF considered.

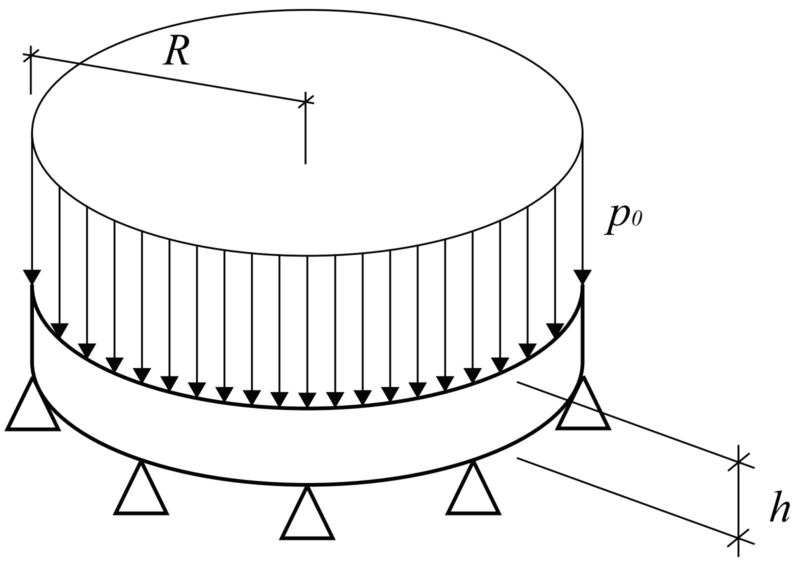

Figure 5.6: Three dimensional picture representing a simply supported circular slab, subjected to a uniformly distributed circular load acting over the entire plate area with intensity p_0.

5.2.1 Elastic theory

The solution of the governing differential equation 2.86 is given by expression 2.91. It is easy to see that the logarithm terms in this solution leads to an infinite displacement when $r = 0$, so the constants C_1 and C_2 must be equal to zero. Therefore the solution becomes:

$$w(r) = C_3 r^2 + C_4 + \frac{p_0 r^4}{64D} \tag{5.30}$$

The constants C_3 and C_4 are now worked out from the boundary conditions:

$$w(r = R) = 0 \qquad M_r(r = R) = 0 \tag{5.31}$$

Considering $C_1 = 0$ and $C_2 = 0$ one can get from expression 2.92:

$$M_r = -D \left[2C_3(1 + \nu) + \frac{p_0 r^2}{16D}(3 + \nu) \right] \tag{5.32}$$

Finally the constants are:

$$C_3 = -\frac{p_0 R^2}{32D}\frac{(3+\nu)}{(1+\nu)} \qquad C_4 = \frac{p_0 R^4}{64D}\frac{(5+\nu)}{(1+\nu)} \tag{5.33}$$

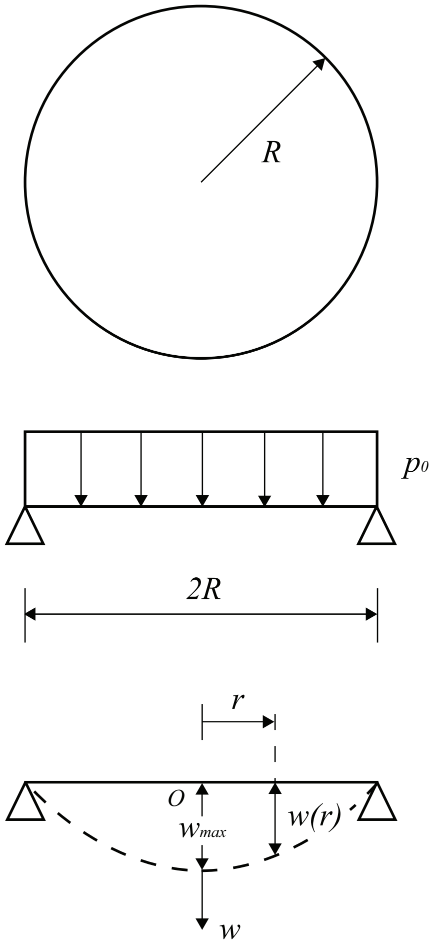

Figure 5.7: A simply supported circular slab under uniform load.

Substituting the expressions of the constants into equation 5.30 one can finally obtain the deflection equation of the simply supported circular slab under uniform load:

$$w(r) = \frac{p_0(R^2 - r^2)}{64D}\left(\frac{\nu+5}{\nu+1}R^2 - r^2\right) \tag{5.34}$$

The maximum deflection w_{max} is found for $r = 0$:

$$w_{max} = \frac{p_0 R^4}{64D}\left(\frac{\nu+5}{\nu+1}\right) \tag{5.35}$$

Elastic stage coefficients

In this section the transformation coefficients to obtain a SDOF system are developed according to the variational approach that was presented in chapter 3.

Firstly, on the basis of the elastic solution just reviewed above, the shape function is assumed as the ratio of the deflection function with respect to the maximum displacement:

$$\psi(r) = \frac{w(r)}{w_{max}} = \frac{R^2 - r^2}{R^4}\left(\frac{\nu+1}{\nu+5}\right)\left(\frac{\nu+5}{\nu+1}R^2 - r^2\right) \tag{5.36}$$

The transformation coefficients for the elastic stage are then worked out as was explained in chapter 3 talking about the vibration analysis of circular plates:

$$m_e^* = \int_0^{2\pi}\int_0^R \rho h \psi^2(r)\, r\, \mathrm{d}\theta\, \mathrm{d}r \tag{5.37}$$

$$= \frac{\pi R^2 \rho h (3\nu^2 + 36\nu + 113)}{15(\nu+5)^2} \tag{5.38}$$

$$k_e^* = D\int_0^{2\pi}\int_0^R \left[\left(\frac{\partial^2\psi}{\partial r^2} + \frac{1}{r}\frac{\partial\psi}{\partial r}\right)^2 - 2(1-\nu)\left(\frac{\partial^2\psi}{\partial r^2}\frac{1}{r}\frac{\partial\psi}{\partial r}\right)\right] r\, \mathrm{d}\theta\, \mathrm{d}r \tag{5.39}$$

$$= \frac{64\pi D(\nu+1)(\nu+7)}{3R^2(\nu+5)^2} \tag{5.40}$$

$$p_e^* = p(t)\int_0^{2\pi}\int_0^R \psi(r)\, r\, \mathrm{d}\theta\, \mathrm{d}r \tag{5.41}$$

$$= p(t)\frac{\pi R^2(\nu+7)}{3(\nu+5)} \tag{5.42}$$

$$= p(t)\, L_e^* \tag{5.43}$$

As was seen in chapter 3 (equation 3.7), it is possible to normalize the transformation factors by using the corresponding total parameters (Biggs, 1964), obtaining:

$$K_M^e = \frac{m_e^*}{m_t} \tag{5.44}$$

$$K_R^e = \frac{k_e^*}{k_t} \tag{5.45}$$

$$K_L^e = \frac{p_e^*(t)}{p_t(t)} \tag{5.46}$$

where m_t is the total mass [M]:

$$m_t = \rho h \pi R^2 \tag{5.47}$$

k_t is the force per unit displacement [F/L]:

$$k_t = \frac{64\pi D}{R^2}\left(\frac{\nu+1}{\nu+5}\right) \tag{5.48}$$

$p_t(t)$ is the total load [F]:

$$p_t(t) = p(t)\pi R^2 \tag{5.49}$$

Therefore by substitution the following expressions can be obtained:

$$K_M^e = \frac{3\nu^2 + 36\nu + 113}{15(\nu + 5)^2} \tag{5.50}$$

$$K_R^e = \frac{1}{3}\left(\frac{\nu + 7}{\nu + 5}\right) \tag{5.51}$$

$$K_L^e = \frac{1}{3}\left(\frac{\nu + 7}{\nu + 5}\right) \tag{5.52}$$

As can be seen $K_R^e = K_L^e$. This is due to the fact that the elastic shape of deflection was assumed to be equal to the elastic one in the static case. The resistance of an element can be defined as the internal force which tends to restore the element in its unloaded static position. If the resistance is defined in terms of the load distribution for which the analysis is performed, as a consequence the maximum resistance will be equal to the total load which the element could support statically. The stiffness is equal to the total load which would cause a unit deflection at the point where the mass, according to the idealization, has been concentrated.

5.2.2 Plastic mechanism and ultimate resistance

In this section the plastic shape is assumed according to the *yield line theory* (Johansen, 1972) and moreover the ultimate resistance is computed according to the upper bound (kinematic) theorem (Chen and Han, 1988). It will be assumed a conical failure mechanism as illustrated in figure 5.9, giving rise to the corresponding plastic shape function (shown in figure 5.8):

$$\psi_{pl}(r) = 1 - \frac{r}{R} \tag{5.53}$$

The external work rate is given by:

$$W_E = \frac{1}{3}\, p_0(\pi R^2)\, \delta \tag{5.54}$$

With given deflection, the rotation about the radial yield line in the θ direction ϕ_θ is easy to obtain as $\phi_\theta = \delta/(rR)$ (Chen and Han, 1988). Therefore, the rate of internal energy dissipation per unit area is $m_0\delta/(rR)$. Integrating over the slab area, one can get the total rate of internal energy dissipation:

$$W_I = 2\pi \int_0^R m_0 \frac{\delta}{rR}\, \mathrm{d}r = 2\pi m_0 \delta \tag{5.55}$$

The virtual work theorem states that:

$$W_E = W_I \tag{5.56}$$

Hence by substituting the previous expressions one can get:

$$\frac{1}{3}\, p_0(\pi R^2)\, \delta = 2\pi m_0 \delta \tag{5.57}$$

where $p_0(\pi R^2) = F_{su}$, being F_{su} the collapse load.
Therefore the ultimate resistance force [N] is given by:

$$F_{su} = 6\pi m_0 \tag{5.58}$$

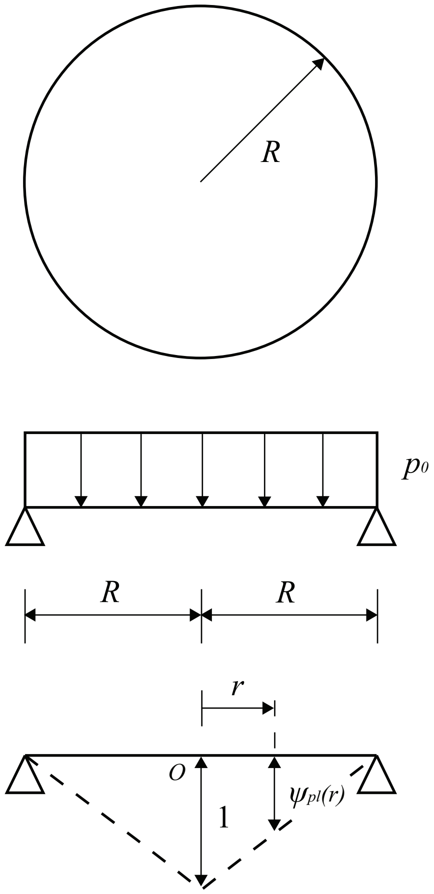

Figure 5.8: Case 1: the plastic shape of deformation.

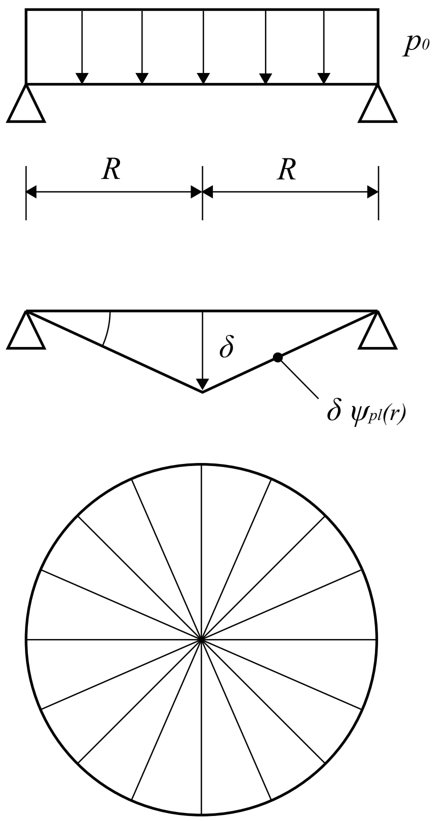

Figure 5.9: Case 1: failure mechanism of a simply supported circular slab under uniform load p_0.

Plastic stage coefficients

The transformation coefficients for the plastic stage are equal to:

$$m_p^* = \int_0^{2\pi} \int_0^R \rho h \psi^2(r)\, r \,\mathrm{d}\theta \,\mathrm{d}r \tag{5.59}$$

$$= \frac{\rho h \pi R^2}{6} \tag{5.60}$$

$$k_p^* = 0 \tag{5.61}$$

$$p_p^* = p(t) \int_0^{2\pi} \int_0^R \psi(r)\, r \,\mathrm{d}\theta \,\mathrm{d}r \tag{5.62}$$

$$= p(t) \frac{\pi R^2}{3} \tag{5.63}$$

$$= p(t)\, L_p^* \tag{5.64}$$

By using the same approach that was previously illustrated (Biggs, 1964), the following expressions for the normalized transformation coefficients can be obtained:

$$K_M^p = \frac{m_p^*}{m_t} = \frac{1}{6} \tag{5.65}$$

$$K_L^p = \frac{p_p^*(t)}{p_t(t)} = \frac{1}{3} \tag{5.66}$$

5.2.3 Example of dynamic analysis

In this section the graphical outputs of a dynamic analysis of example, performed using the algorithms proposed in this work, will be presented.
In order to simulate a shock tube specimen, the data assumed to perform this analysis are the following ones:

Slab geometry:

- slab thickness $h = 0.10$ m;
- slab radius $R = 0.29$ m.

Traditional reinforcement characteristics:

- concrete cover $c = 0.02$ m;
- characteristic yielding stress of steel $f_{yk} = 430$ MPa;
- steel elastic Young modulus $E_s = 206$ GPa;
- rebar diameter $\phi = 12$ mm;
- number of rebars $n_{rebar} = 5$.

Concrete characteristics:

- characteristic resistance of concrete $f_{ck} = 70$ MPa;
- concrete elastic Young modulus $E_c = 42.6$ GPa;
- Poisson modulus $\nu = 0.2$;
- concrete density $\rho = 2500$ kg/m^3.

Load characteristics:

- peak pressure $p_{max} = 2.6$ MPa;
- total load time duration $t_d = 10$ ms;
- shape of the pulse: right-angle triangle.

The dynamic analysis was run considering to reach eight peaks in the displacement response before the analysis stopped (i.e., $n_{peaks} = 8$), as can be seen in figure 5.12.

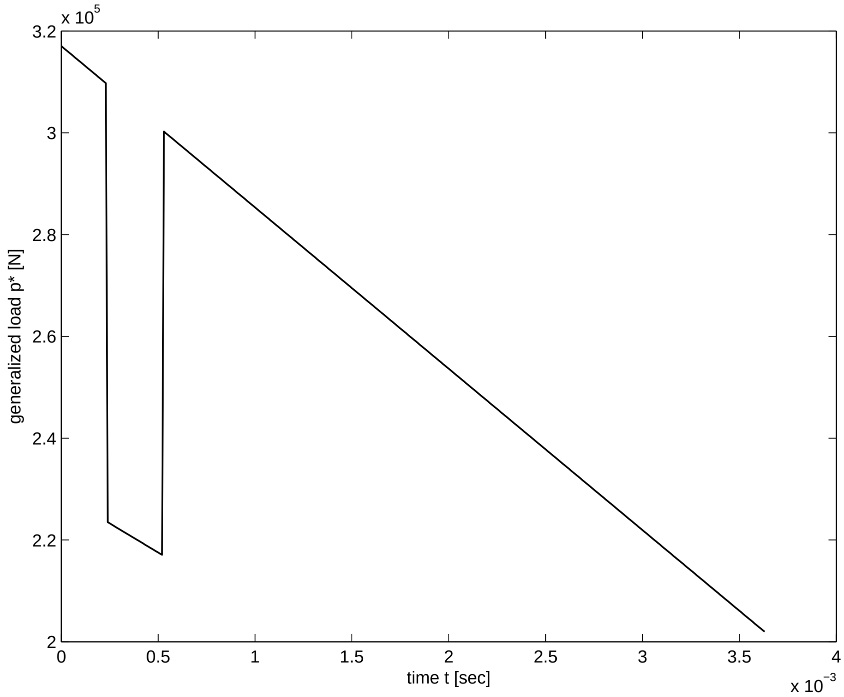

Figure 5.10: Case 1, example: generalized load vs time.

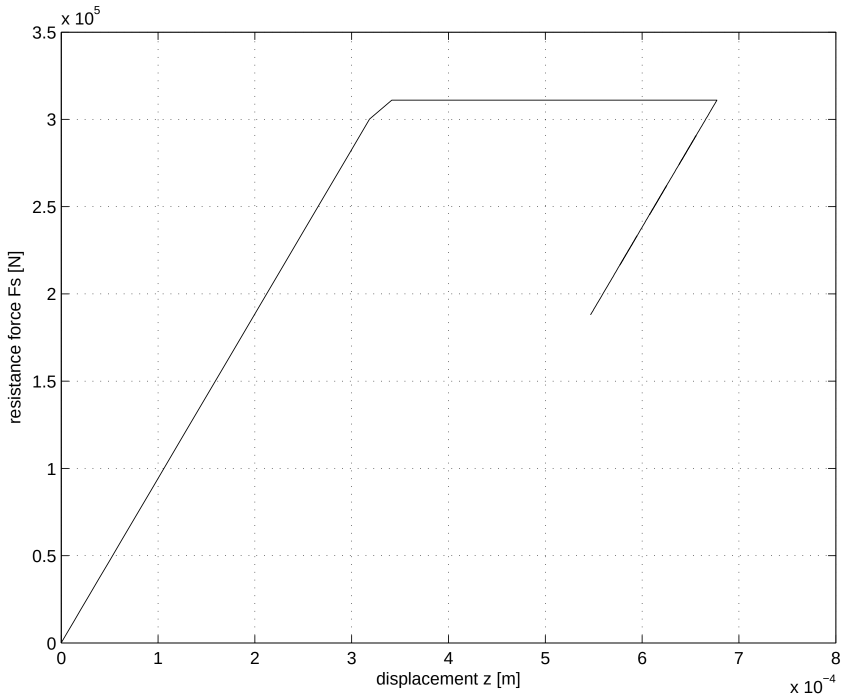

Figure 5.11: Case 1, example: mid-span displacement versus resistance force.

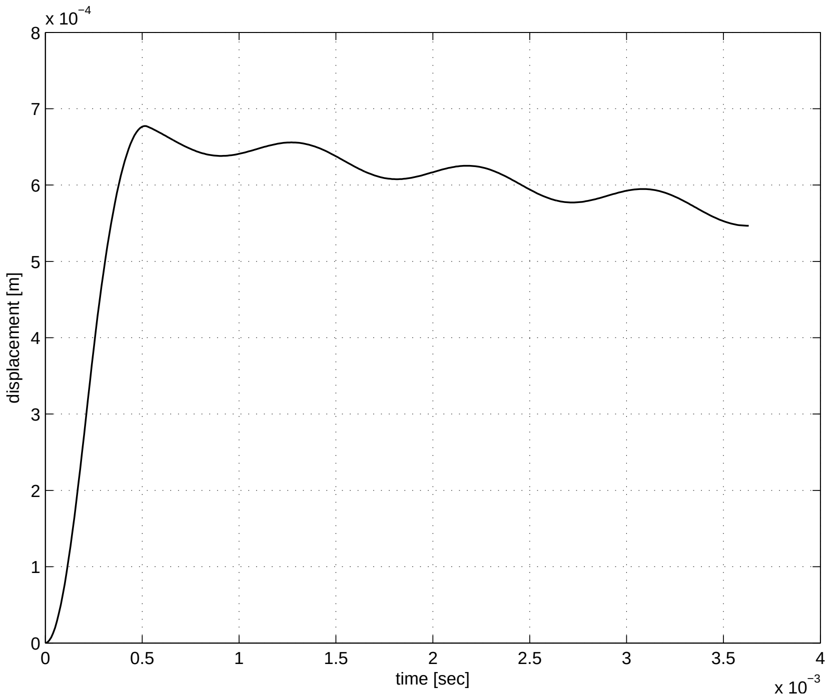

Figure 5.12: Case 1, example: mid-span displacement versus time.

Figure 5.11 clearly shows the achievement of the collapse load F_{su}, and figure 5.13 evidences how the system reaches its plasticization from 0.225 to 0.515 ms in the positive phase. Within this interval the system works with the plastic shape function, meaning that all the generalized parameters (k^*, p^*, m^*) change. This is highlighted in figure 5.10, in which can be seen that during the plastic interval the behaviour of the generalized load p^* changes in a sudden way, and when the system turns back to the elastic phase another sudden change to elastic behaviour occurs.
It has been observed that the positive plasticization is reached in the first cycle and in the subsequent cycles the plastic branch is not reached any more due to the decreasing trend of the excitation pulse. Therefore, for decreasing pulse shapes, the highest structure damage is expected in the first cycles.

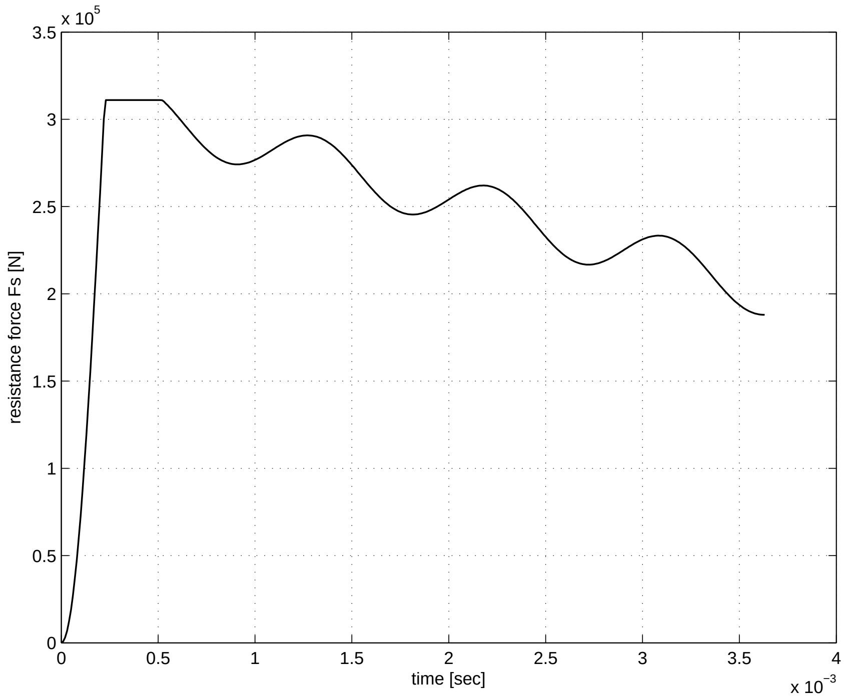

Figure 5.13: Case 1, example: resistance force versus time.

5.2.4 Pressure-impulse diagrams

Putting into practice the concepts already seen in chapter 4, this section develops all the calculations in order to derive the p-i diagrams.
The calculation of the asymptotes takes advantage of the energetic approach described in the previous chapter, for which it is necessary to compute the maximum external energy, the maximum kinetic energy and the maximum internal energy dissipated by the system.
It will be found that there are two cases for computing the maximum internal energy depending on the allowable threshold displacement $\widetilde{w}_{max}$, because this value may lie in the elastic phase or in the plastic one according to the characteristics of the generalized system.
After the asymptotes calculation, the p-i curve is derived with the algorithms proposed in chapter 4, namely by means of iterative calculations.

Kinetic energy. Referring to the generic plate element as represented in figure 5.14, one can compute the kinetic energy as follows:

$$K = \int\int_S \frac{1}{2}\,\overline{m}\,v_0^2\,\mathrm{d}S = \int_0^{2\pi}\int_0^R \frac{1}{2}\,\rho\,h\,v_0^2\,r\,\mathrm{d}\theta\,\mathrm{d}r \tag{5.67}$$

where v_0 is the initial velocity, which can be defined exploiting the momentum definition according to the impulse theorem:

$$v_0 = \frac{I}{m} = \frac{i\,r\,\mathrm{d}\theta\,\mathrm{d}r}{\rho\,h\,r\,\mathrm{d}\theta\,\mathrm{d}r} = \frac{i}{\rho\,h} \tag{5.68}$$

being I the total impulse [F·T], i the specific impulse [F·T/L^2] and $m = \rho\,h\,r\,\mathrm{d}\theta\,\mathrm{d}r$ the total mass of the plate element [M].
Finally the expression of the kinetic energy can be rewritten as:

$$K = 2\pi\rho h\frac{1}{2}\int_0^R \frac{i^2}{\rho^2\,h^2}\,r\,\mathrm{d}r = \frac{i^2\pi R^2}{2\rho h} \tag{5.69}$$

A) Case in which $\widetilde{w}_{max} < w_{el}$

As was mentioned in the introduction to this section, under certain geometrical and stiffness conditions it is possible to obtain a damage threshold $\widetilde{w}_{max}$ smaller than the displacement at the elastic limit w_{el}, leading to different formulations for the strain energy computation. In order to prove this statement, the case of a simply supported circular slab made in FRC has been considered. Since it is necessary to compare the values of w_{el} and $\widetilde{w}_{max}$, one should remember from the previous computations that:

$$w_{el} = \frac{F_{su}}{k_e^*} \tag{5.70}$$

and from equation 5.40:

$$k_e^* = \frac{D}{R^2}\,\frac{64\pi(\nu+1)(\nu+7)}{3(\nu+5)^2} = \frac{D}{R^2}\,C_{\nu,1} \tag{5.71}$$

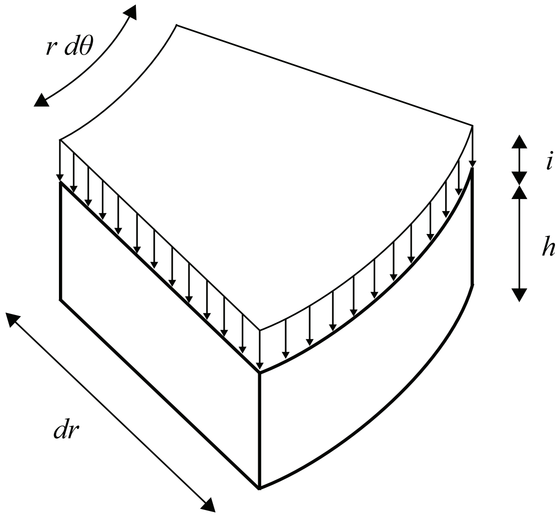

Figure 5.14: A generic circular plate element subjected to a specific impulse of intensity i.

where the coefficient $C_{\nu,1}$ has been introduced in order to obtain a compact expression. Note that this coefficient varies little with varying ν, thus can be practically considered as a constant.
Recalling the expression for the constant D which appears in the Germain-Lagrange equation for plates (equation 2.56):

$$D = \frac{E\,h^3}{12(1-\nu)^2} = E\,h^3\,C_{\nu,2} \tag{5.72}$$

where the coefficient $C_{\nu,2}$ has been introduced in order to obtain a compact expression. Note that also this coefficient varies little with varying ν.
Substituting equation 5.72 into equation 5.71 one can get:

$$k_e^* = \frac{E\,h^3}{R^2}\,C_{\nu,1}\,C_{\nu,2} = \frac{E\,h^3}{R^2}\,C_\nu \tag{5.73}$$

where the coefficient C_ν collects all the dependency on the Poisson coefficient ν. Now recalling equation 5.58:

$$F_{su} = 6\pi m_0 \tag{5.74}$$

and substituting into it equation 5.28:

$$m_0 = f_{Ftud}\,\frac{h^2}{2} + (f_{Ftsd} - f_{Ftud})\,\frac{h^2}{6} \tag{5.75}$$

$$= \frac{h^2}{2}\left[f_{Ftud} + \frac{1}{3}\,(f_{Ftsd} - f_{Ftud})\right] \tag{5.76}$$

one can obtain:

$$F_{su} = 3\pi\left[f_{Ftud} + \frac{1}{3}\,(f_{Ftsd} - f_{Ftud})\right]\,h^2 = C_f\,h^2 \tag{5.77}$$

where the coefficient C_f collects all the dependency on the strength parameters of the FRC. Now substituting equation 5.73 and equation 5.77 into equation 5.70, one can finally work out:

$$w_{el} = \frac{F_{su}}{k_e^*} = \frac{C_f\, h^2}{\dfrac{E\, h^3}{R^2}\, C_\nu} = \frac{R^2}{E\, h}\left(\frac{C_f}{C_\nu}\right) = \frac{R^2}{E\, h}\, C_{f,\nu} \tag{5.78}$$

where the coefficient $C_{f,\nu}$ collects all the factors related to the strength and to the Poisson modulus.
Recalling equation 5.29:

$$\widetilde{w}_{max} = R\, \frac{CTOD_u}{2h} \tag{5.79}$$

and comparing it to equation 5.78:

$$w_{el} \lesseqgtr \widetilde{w}_{max} \tag{5.80}$$

one can finally obtain:

$$\frac{R^2}{E\, h}\, C_{f,\nu} \lesseqgtr R\, \frac{CTOD_u}{2h} \tag{5.81}$$

$$\frac{R}{E}\, C_{f,\nu} \lesseqgtr \frac{CTOD_u}{2} \tag{5.82}$$

The analysis performed above shows that, according to the selected damage criterion, it is possible to obtain values of $\widetilde{w}_{max}$ smaller than w_{el} when the ratio R/E tends to be very large; in addition, from a practical point of view, E could be considered as a constant, because we are talking about a plate made of the same material. Therefore, when R is large enough, the threshold value might lay in the elastic stage, thereby it is a matter of geometrical nature. Physically this issue makes sense because the value of $CTOD_u$ has been chosen in order to limit the crack opening displacement at midspan, which is not directly related with the achievement of the plasticization of the whole structure. For a very large slab the value of $CTOD_u$ is reached before obtaining the complete plasticization of the structure. That is why the threshold displacement might lay in the idealized elastic phase, but actually the structure has already started to plasticize. The same procedure outlined above may be applied to R/C, leading to the same conclusions.

Figure 5.15 demonstrates that the plate radius R influences directly the damage threshold. The decreasing path explains how the plastic contribute to the total energy decreases as R increases. Therefore plates with small values of R will be allowed to dissipate more energy in the plastic phase with respect to plates with greater values of R. It is worth noting that within the framework of shock tube experimental tests only small plate radii are of interest.

Elastic strain energy. When the selected damage threshold is smaller than the displacement at the elastic limit (i.e. $\widetilde{w}_{max} < w_{el}$), the strain energy is simply represented by the elastic one, as can be seen in figure 5.16.

$$U_{el} = \frac{1}{2}\, k_e^*\, \widetilde{w}_{max}^2 \tag{5.83}$$

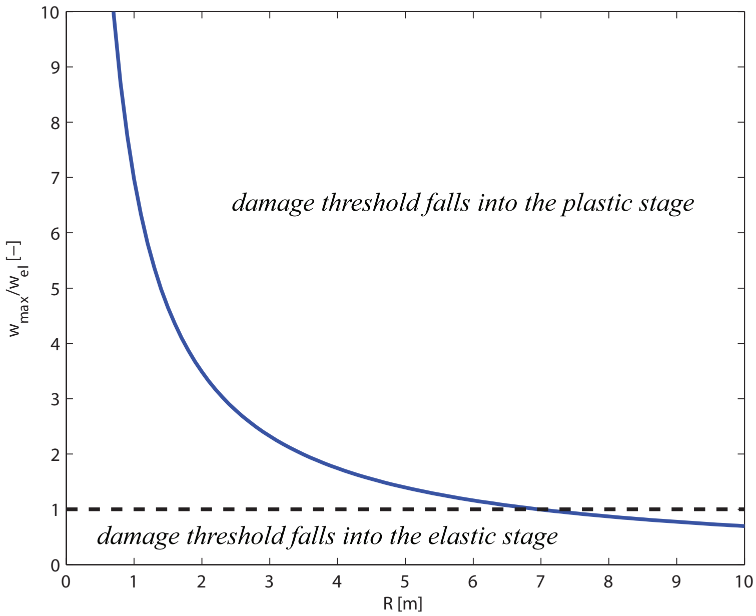

Figure 5.15: Variation of $\widetilde{w}_{max}/w_{el}$ as a function of R (case 1).

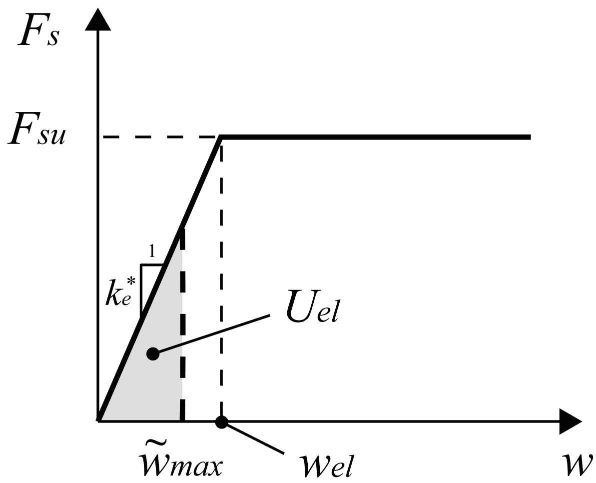

Figure 5.16: Elastic strain energy.

Maximum possible work. When $\widetilde{w}_{max} < w_{el}$ the shape function to assume in the computation of the maximum possible work is the elastic one:

$$W^{el}_{max} = \int\int_S p(r)w(r)\mathrm{S} = \int_0^{2\pi}\int_0^R p_0 w(r)\, r\, \mathrm{d}\theta\, \mathrm{d}r \tag{5.84}$$

Recalling the elastic shape function that was chosen for case 1:

$$w(r) = \widetilde{w}_{max}\left[\frac{R^2 - r^2}{R^4}\left(\frac{\nu+1}{\nu+5}\right)\left(\frac{\nu+5}{\nu+1}R^2 - r^2\right)\right] \tag{5.85}$$

and substituting it into equation 5.84 one can finally obtain the expression for the maximum work:

$$W^{el}_{max} = \widetilde{w}_{max}\,\frac{p_0\,\pi\,R^2(\nu+7)}{3(\nu+5)} \tag{5.86}$$

Quasi-static asymptote. By exploiting the definition that permits to work out the quasi-static asymptote as it was presented in the previous chapter:

$$U_{el} = W^{el}_{max} \tag{5.87}$$

and performing the needed substitutions one can get:

$$\frac{1}{2}\,k^*_e\,\widetilde{w}^2_{max} = \widetilde{w}_{max}\,\frac{p_0\,\pi\,R^2(\nu+7)}{3(\nu+5)} \tag{5.88}$$

Finally the quasi-static asymptote has the following expression:

$$q.s.a. = p_0 = \frac{3k^*_e(\nu+5)}{2\pi R^2(\nu+7)}\,\widetilde{w}_{max} \tag{5.89}$$

Recalling that:

$$L^*_e = \frac{\pi R^2(\nu+7)}{3(\nu+5)} \tag{5.90}$$

(which is the multiplier coefficient to get the generalized load in the elastic stage), equation 5.89 can be rewritten in a compact form as follows:

$$q.s.a. = \frac{k^*_e}{2L^*_e}\,\widetilde{w}_{max} \tag{5.91}$$

from which it is clear that the quasi-static asymptote is dependent of stiffness and geometric characteristics.

Impulsive asymptote. As was discussed in chapter 4, the impulsive asymptote can be worked out by exploiting the following equation:

$$K = U_{el} \tag{5.92}$$

Substituting equations 5.69 and 5.83 into the previous expression:

$$\frac{i^2\pi R^2}{2\rho h} = \frac{1}{2}\,k^*_e\,\widetilde{w}^2_{max} \tag{5.93}$$

Equation 5.93 can be rewritten in compact form as follows, highlighting the impulsive asymptote:

$$i.a. = \sqrt{\frac{2\overline{m}\,U_{el}}{A_{load}}} \tag{5.94}$$

where $\overline{m} = \rho\, h$ is the specific mass per unit area and $A_{load} = \pi R^2$ is the plate area occupied by the load.

B) Case in which $\widetilde{w}_{max} > w_{el}$

Elastoplastic strain energy. When the selected damage threshold is greater than the displacement at the elastic limit (i.e. $\widetilde{w}_{max} > w_{el}$), the strain energy is represented by the sum of the elastic and plastic energy, as can be seen in figure 5.17. In the calculation of the maximum possible work both the elastic and plastic contributes will be considered. The energy will be computed assuming that the damage threshold $\widetilde{w}_{max}$ is reached during the first cycle, namely in the loading branch and not in the unloading one, thus excluding the possibility of obtaining a negative work contribute.
Under this hypothesis, the elastoplastic strain energy is equal to:

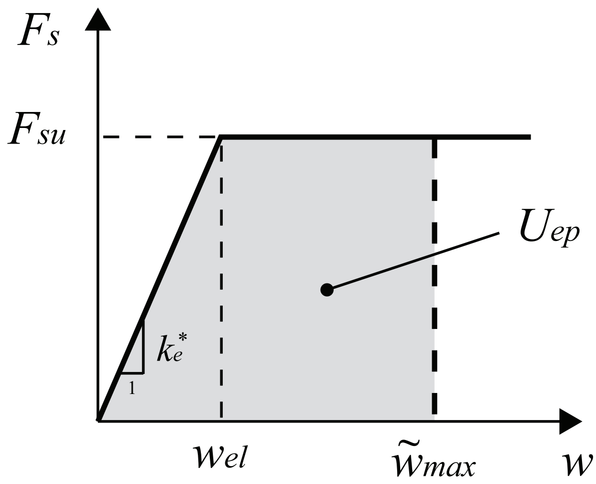

Figure 5.17: Elastoplastic strain energy.

$$U_{ep} = U_{el} + U_{pl} = \frac{w_{el} \cdot F_{su}}{2} + (\widetilde{w}_{max} - w_{el})F_{su} = F_{su}\left(\widetilde{w}_{max} - \frac{w_{el}}{2}\right) \quad (5.95)$$

Maximum possible work. When $\widetilde{w}_{max} > w_{el}$, both the contributes of the elastic and plastic stages to the total work must be considered.

$$W_{max}^{ep} = p_{max}^{*el}\, w_{el} + p_{max}^{*pl}\, (\widetilde{w}_{max} - w_{el}) \quad (5.96)$$

$$= L_e^* \, p_0 \, w_{el} + L_p^* \, p_0 \, (\widetilde{w}_{max} - w_{el}) \quad (5.97)$$

$$= \frac{p_0 \, \pi R^2 \, (\nu + 7)}{3(\nu + 5)} \, w_{el} + \frac{p_0 \, \pi R^2}{3} \, (\widetilde{w}_{max} - w_{el}) \quad (5.98)$$

where L_e^* and L_p^* are the multiplier coefficients to get the generalized load in the elastic and plastic stage, respectively.

Quasi-static asymptote. As was done previously, the expression for the quasi-static asymptote is exploited:

$$U_{ep} = W_{max}^{ep} \quad (5.99)$$

which yields, together with equations 5.95 and 5.98:

$$F_{su}\left(\widetilde{w}_{max} - \frac{w_{el}}{2}\right) = w_{el}\,\frac{p_0\,\pi R^2\,(\nu+7)}{3(\nu+5)} + (\widetilde{w}_{max} - w_{el})\,\frac{p_0\,\pi R^2}{3} \tag{5.100}$$

The last equality provides the expression for the quasi-static asymptote:

$$q.s.a. = p_0 = \frac{U_{ep}}{\dfrac{\pi R^2}{3}\left[w_{el}\,\dfrac{(\nu+7)}{(\nu+5)} + \widetilde{w}_{max} - w_{el}\right]} \tag{5.101}$$

Recalling that:

$$L_p^* = \frac{\pi R^2}{3} \tag{5.102}$$

(which is the multiplier coefficient to get the generalized load in the plastic stage), equation 5.101 can be rewritten in a more compact form as follows:

$$q.s.a. = \frac{U_{ep}}{L_p^*\left[w_{el}\,\dfrac{(\nu+7)}{(\nu+5)} + \widetilde{w}_{max} - w_{el}\right]} \tag{5.103}$$

Impulsive asymptote. Also here the procedure is the same that was previously followed, namely by making use of the equation:

$$K = U_{ep} \tag{5.104}$$

and recalling equation 5.69 and 5.95, one can get:

$$\frac{i^2\pi R^2}{2\rho h} = F_{su}\left(\widetilde{w}_{max} - \frac{w_{el}}{2}\right) \tag{5.105}$$

Rearranging the last equation one can finally achieve the expression for computing the impulsive asymptote:

$$i.a. = i = \sqrt{\frac{2\rho\,h\,F_{su}\left(\widetilde{w}_{max} - \dfrac{w_{el}}{2}\right)}{\pi\,R^2}} \tag{5.106}$$

In addition, equation 5.106 can be rewritten in compact form as follows:

$$i.a. = \sqrt{\frac{2\overline{m}\,U_{ep}}{A_{load}}} \tag{5.107}$$

where $\overline{m} = \rho\,h$ is the specific mass per unit area and $A_{load} = \pi R^2$ is the plate area occupied by the load.

Plotted diagrams

In this section some results will be presented. The results illustrated as follows correspond to circular plates made in RC and FRC. The geometrical and material properties are assumed as the same values taken from the dynamic analysis example; however these data are written inside the figures. The chosen excitation pulse shape is a decreasing exponential function, with the parameter λ set equal to 5, in order to get a more realistic representation of a blast loading shape. The value of w_{max} is recorded in the figures and corresponds to the damage threshold computed according to the selected criterion.

RC. The following example (figure 5.18) shows the p-i curve generated by using the algorithms proposed in this work. The geometrical dimensions and the RC material properties were adopted in order to represent a sample for the shock tube test.

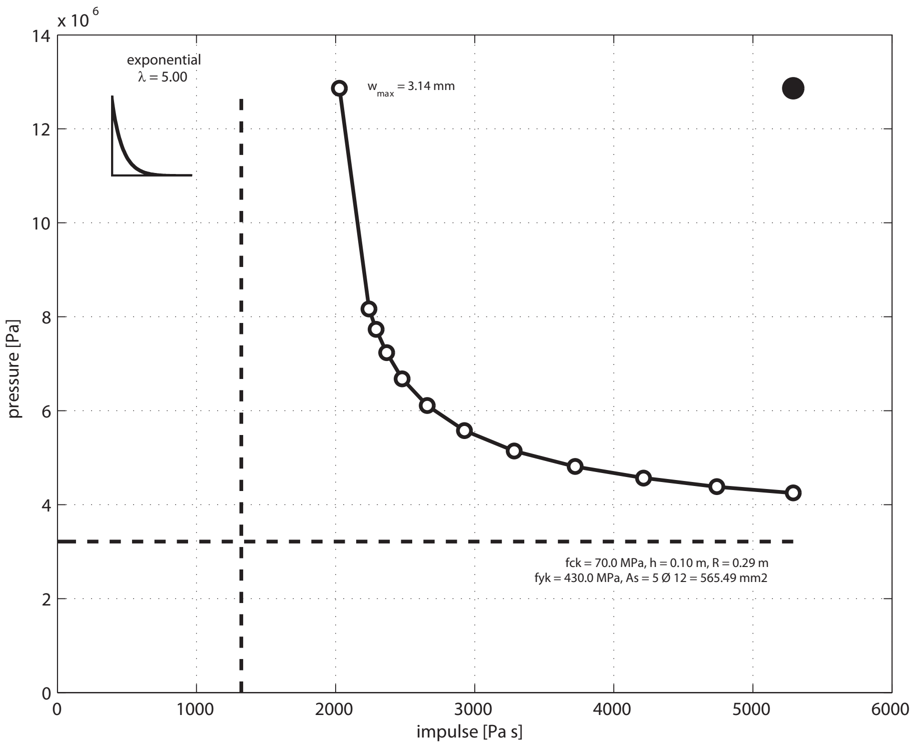

Figure 5.18: Case 1: example of p-i diagram for a reinforced concrete plate.

FRC. As follows, an example of the algorithms' application is performed for special plate's characteristics (figure 5.19), which correspond to a possible shock tube's specimen. The FRC material properties adopted are taken from experimental results recorded in the paper *Mechanical properties of steel fibre reinforced concrete exposed to high temperatures* (Colombo et al., 2010).

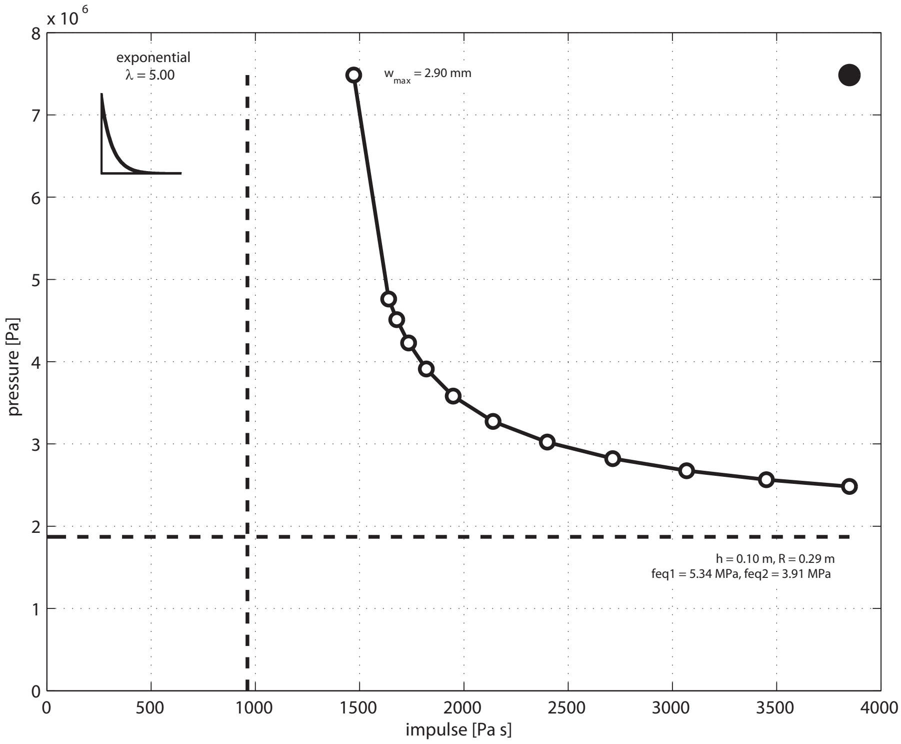

Figure 5.19: Case 1: example of p-i diagram for a fibre reinforced plate.

5.3 Case 2: circular slab on grade

Consider here the bending of a circular slab of radius R, with free edge, subjected to a uniform circular load of intensity p_0 and radius b, as shown in figure 5.20. In order to simplify the soil-structure interaction, whose analysis is very complex, soil is modelled as a Winkler's soil. Winkler's soil represents a bed of independent springs under the structure having purely elastic behaviour. The reaction provided by these springs is equal to the displacement in a certain point times the elastic constant k_s, which corresponds to a given type of soil as reported in table 5.1.

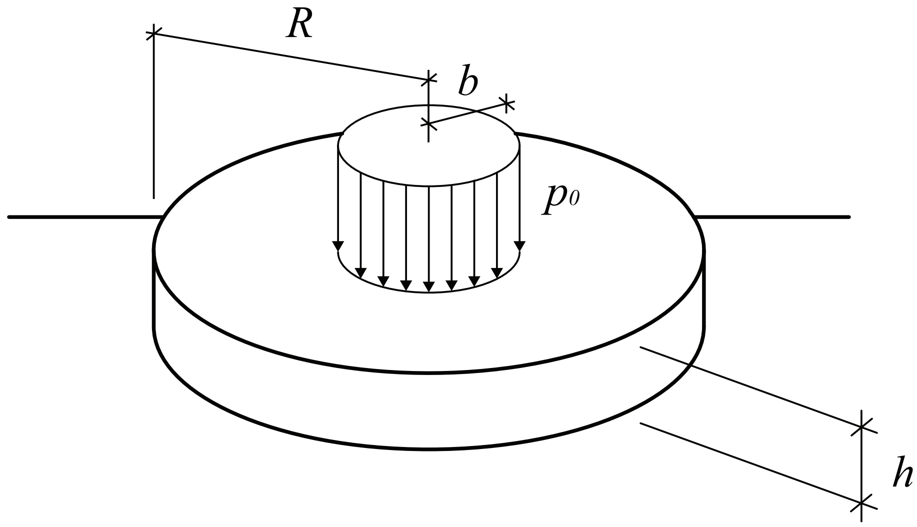

Figure 5.20: Three dimensional picture representing a circular slab resting on a Winkler-type soil, subjected to a uniformly distributed circular load of radius b with intensity p_0.

5.3.1 Elastic theory

The deflection of the slab within the loaded region is denoted as $w_1(r)$, whilst $w_2(r)$ is the deflection of the slab within the unloaded region, as shown in figure 5.21. Note that outside the region occupied by the slab ($r > R$) there are no surface displacements, though in the reality there would be soil motion even outside that region. This is due to the discontinuous behaviour of the Winkler medium.
In mathematical form, the subgrade reaction can be described by:

$$q(r) = k_s w(r) \tag{5.108}$$

where k_s is the modulus of the foundation.
Starting from the plate equilibrium equation of Sophie Germain - Lagrange (equation 2.84):

$$\nabla_r^4 w(r) = \frac{p(r)}{D} \tag{5.109}$$

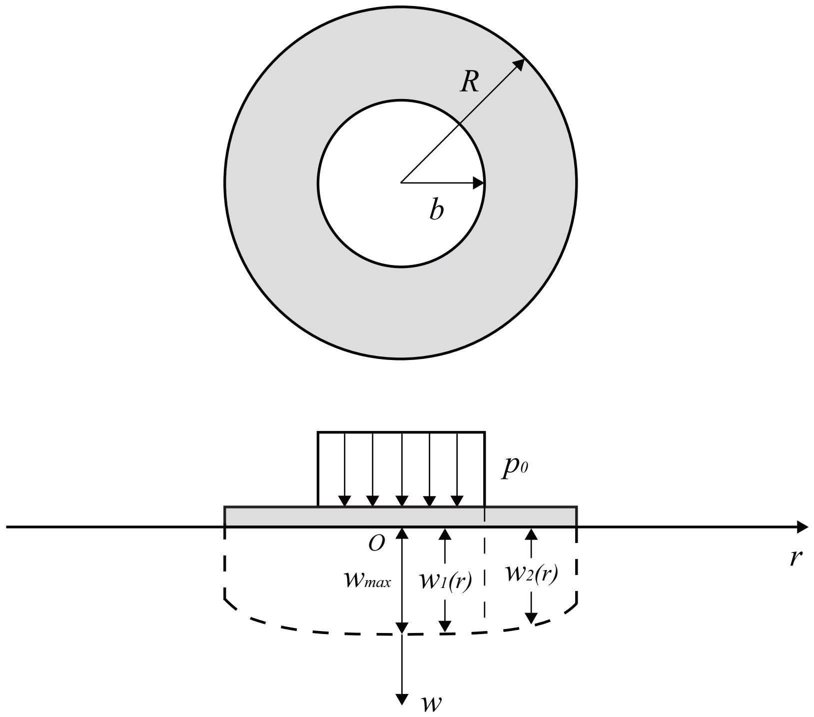

Figure 5.21: A circular slab resting on a Winkler-type soil, subjected to a uniform circular load of intensity p_0.

Table 5.1: Range of modulus of subgrade reaction k_s according to Bowles (1968)

Soil	k_s [kN/m^3]
Loose sand	4800-16000
Medium dense sand	9600-80000
Dense sand	64000-128000
Clayey medium dense sand	32000-80000
Silty medium dense sand	24000-48000
Clayey soil:	
$q_a \leq 200$ kPa	12000-24000
$200 < q_a \leq 800$ kPa	24000-48000
$q_a > 200$ kPa	>48000

and adding the term due to the soil reaction, one can get the governing differential equation for this case:

$$D\nabla_r^4 w(r) + k_s w(r) = p(r) \tag{5.110}$$

Equation 5.110 can be rewritten as follows:

$$\left(\frac{\mathrm{d}^2}{\mathrm{d}r^2} + \frac{1}{r}\frac{\mathrm{d}}{\mathrm{d}r}\right)\left(\frac{\mathrm{d}^2 w}{\mathrm{d}r^2} + \frac{1}{r}\frac{\mathrm{d}w}{\mathrm{d}r}\right) = \frac{1}{D}(p - k_s w) \tag{5.111}$$

By introducing the characteristic length l:

$$l = \sqrt[4]{\frac{D}{k_s}} \tag{5.112}$$

and the dimensionless coordinate $\zeta = r/l$, equation5.111 can be rewritten as:

$$\left(\frac{\mathrm{d}^2}{\mathrm{d}\zeta^2} + \frac{1}{\zeta}\frac{\mathrm{d}}{\mathrm{d}\zeta}\right)^2 w + w = \frac{pl^4}{D} \tag{5.113}$$

Introducing the notation:

$$\nabla_\zeta^2 = \frac{\mathrm{d}^2}{\mathrm{d}\zeta^2} + \frac{1}{\zeta}\frac{\mathrm{d}}{\mathrm{d}\zeta} \tag{5.114}$$

finally one can get:

$$\nabla_\zeta^4 w(r) + w(r) = \frac{pl^4}{D} \tag{5.115}$$

which is the compact form of the governing differential equation of bending of a circular slab resting on a Winkler-type elastic medium.
It is convenient to consider the loaded and the unloaded regions separately. The deflection of the slab in the loaded and in the unloaded regions are denoted by $w_1(r)$ and $w_2(r)$, respectively. Thus two governing differential equation must be solved:

- In the loaded region ($0 \leq r \leq b$):

$$\nabla_\zeta^4 w_1(r) + w_1(r) = \frac{p_0 l^4}{D} \tag{5.116}$$

- In the unloaded region ($b < r \leq R$):

$$\nabla_\zeta^4 w_2(r) + w_2(r) = 0 \tag{5.117}$$

The solutions of these equations can be found in Selvadurai (1979), amongst the other authors.

- In the loaded region ($0 \leq r \leq b$) the solution is given by:

$$w_1(r) = \frac{p_0}{k_s} + C_1 Z_1(r/l) + C_2 Z_2(r/l) + C_3 Z_3(r/l) + C_4 Z_4(r/l) \tag{5.118}$$

- In the unloaded region ($b < r \leq R$) the solution is given by:

$$w_2(r) = C_5 Z_1(r/l) + C_6 Z_2(r/l) + C_7 Z_3(r/l) + C_8 Z_4(r/l) \tag{5.119}$$

where the Z_n ($n = 1, 2, 3, 4$) functions are defined as follows:

$$Z_1(\zeta) = \text{Re } J_0\left(\zeta\sqrt{i}\right) \tag{5.120}$$

$$Z_2(\zeta) = \text{Im } J_0\left(\zeta\sqrt{i}\right) \tag{5.121}$$

$$Z_3(\zeta) = \text{Re } H_0^{(1)}\left(\zeta\sqrt{i}\right) \tag{5.122}$$

$$Z_4(\zeta) = \text{Im } H_0^{(1)}\left(\zeta\sqrt{i}\right) \tag{5.123}$$

where $J_0\left(\zeta\sqrt{i}\right)$ is the Bessel function of the first kind of zero order and $H_0^{(1)}\left(\zeta\sqrt{i}\right)$ is the Hankel function of the first kind of zero order (Abramowitz and Stegun, 1965).
The general definition of the Hankel function is:

$$H_\nu^{(1)}(z) := J_\nu(z) + iY_\nu(z) \tag{5.124}$$

where $Y_\nu(z)$ is the Bessel function of the first kind of ν order.
There are also derivation formulae for the Bessel and the Hankel functions, which will be exploited in the following computations in order to derive the Z functions previously defined, working out $Z_1'(\zeta)$, $Z_2'(\zeta)$, $Z_3'(\zeta)$ and $Z_4'(\zeta)$ (Jahnke and Emde, 1945).
These identities are:

$$\frac{d}{dz} J_\nu(z) := \frac{1}{2}\left(J_{\nu-1}(z) - J_{\nu+1}(z)\right) \tag{5.125}$$

$$\frac{d}{dz} H_\nu^{(1)}(z) := \frac{\nu H_\nu^{(1)}(z)}{z} - H_{\nu+1}^{(1)}(z) \tag{5.126}$$

Going back to the analysis of the circular slab, it can be shown that the slope $\mathrm{d}w/\mathrm{d}r$, the bending moments M_r and M_θ and the shear force Q_r are given by the following expressions:

$$\frac{\mathrm{d}w}{\mathrm{d}r} = \frac{1}{l}\left[C_1 Z_1'(r/l) + C_2 Z_2'(r/l) + C_3 Z_3'(r/l) + C_4 Z_4'(r/l)\right] \tag{5.127}$$

$$
\begin{aligned}
M_r \quad = \quad & -\frac{D}{l^2}\,\{C_1 Z_2(r/l) - C_2 Z_1(r/l) + C_3 Z_4(r/l) \\
& - C_4 Z_3(r/l) - \frac{l}{r}(1-\nu)\,[C_1 Z_1'(r/l) + C_2 Z_2'(r/l) \\
& + \; C_3 Z_3'(r/l) + C_4 Z_4'(r/l)]\;\}
\end{aligned}
\tag{5.128}
$$

$$
\begin{aligned}
M_\theta \quad = \quad & -\frac{D}{l^2}\,\{\nu\,[C_1 Z_2(r/l) - C_2 Z_1(r/l) + C_3 Z_4(r/l) \\
& - \; C_4 Z_3(r/l)] + \frac{l}{r}(1-\nu)\,[C_1 Z_1'(r/l) + C_2 Z_2'(r/l) \\
& + \; C_3 Z_3'(r/l) + C_4 Z_4'(r/l)]\;\}
\end{aligned}
\tag{5.129}
$$

$$
Q_r = -\frac{D}{l^3}\,[C_1 Z_2'(r/l) - C_2 Z_1'(r/l) + C_3 Z_4'(r/l) - C_4 Z_3'(r/l)]
\tag{5.130}
$$

Furthermore, it is apparent from equation 5.118 and equation 5.119 that eight arbitrary constants must be calculated in order to determine the shape of deflection of the elastic system. This task can be accomplished by imposing the suitable boundary conditions.
The first two boundary conditions can be imposed by considering the symmetry of the circular slab problem:

$$
\begin{cases}
(1) \quad \left.\left(\dfrac{\mathrm{d}w}{\mathrm{d}r}\right)\right|_{r=0} = 0 \\
(2) \quad Q_r(0) = 0
\end{cases}
\tag{5.131}
$$

These conditions, together with equations 5.127 and 5.130, yield $C_3 = C_4 = 0$. The six remaining constants can be determined by using the four continuity conditions at $r = b$ and the two free edge boundary conditions at $r = R$:

$$
\begin{cases}
(1) \quad w_1(b) = w_2(b) \\
(2) \quad \left.\left(\dfrac{\mathrm{d}w_1}{\mathrm{d}r}\right)\right|_{r=b} = \left.\left(\dfrac{\mathrm{d}w_2}{\mathrm{d}r}\right)\right|_{r=b} \\
(3) \quad M_{r1}(b) = M_{r2}(b) \\
(4) \quad Q_{r1}(b) = Q_{r2}(b) \\
(5) \quad M_{r2}(R) = 0 \\
(6) \quad Q_{r2}(R) = 0
\end{cases}
\tag{5.132}
$$

where M_{r1}, Q_{r1} are, respectively, the expressions for the bending moment and the shear force obtained from $w_1(r)$; analogously M_{r2}, Q_{r2} are obtained from $w_2(r)$.
The six conditions in equation 5.132 result in a system from which the six

constants C_1, C_2, C_5, C_6, C_7 and C_8 can be uniquely worked out:

$$\begin{cases} (1) \quad C_1 Z_{1b} + C_2 Z_{2b} - C_5 Z_{1b} - C_6 Z_{2b} - C_7 Z_{3b} - C_8 Z_{4b} = -\dfrac{p_0}{k_s} \\ (2) \quad C_1 Z'_{1b} + C_2 Z'_{2b} - C_5 Z'_{1b} - C_6 Z'_{2b} - C_7 Z'_{3b} - C_8 Z'_{4b} = 0 \\ (3) \quad C_1 \left[Z_{2b} - \dfrac{l}{b}(1-\nu) Z'_{1b} \right] - C_2 \left[Z_{1b} + \dfrac{l}{b}(1-\nu) Z'_{2b} \right] \\ \qquad -C_5 \left[Z_{2b} - \dfrac{l}{b}(1-\nu) Z'_{1b} \right] + C_6 \left[Z_{1b} + \dfrac{l}{b}(1-\nu) Z'_{2b} \right] \\ \qquad -C_7 \left[Z_{4b} - \dfrac{l}{b}(1-\nu) Z'_{3b} \right] + C_8 \left[Z_{3b} + \dfrac{l}{b}(1-\nu) Z'_{4b} \right] = 0 \\ (4) \quad C_1 Z'_{2b} - C_2 Z'_{1b} - C_5 Z'_{2b} + C_6 Z'_{1b} - C_7 Z'_{4b} + C_8 Z'_{3b} = 0 \\ (5) \quad C_5 \left[Z_{2R} - \dfrac{l}{R}(1-\nu) Z'_{1R} \right] - C_6 \left[Z_{1R} + \dfrac{l}{R}(1-\nu) Z'_{2R} \right] \\ \qquad +C_7 \left[Z_{4R} - \dfrac{l}{R}(1-\nu) Z'_{3R} \right] - C_8 \left[Z_{3R} + \dfrac{l}{R}(1-\nu) Z'_{4R} \right] = 0 \\ (6) \quad C_5 Z'_{2R} - C_6 Z'_{1R} + C_7 Z'_{4R} - C_8 Z'_{3R} = 0 \end{cases} \tag{5.133}$$

In this system, Z_{nb}, Z'_{nb}, Z_{nR} and Z'_{nR} (with $n = 1, 2, 3, 4$) have been used to denote the values assumed by the Z_n and Z'_n functions when $r = b$ and $r = R$, respectively.
The system in equation 5.133 can be rewritten in compact form as follows:

$$\mathbf{Z} \cdot \mathbf{C} = \mathbf{L} \tag{5.134}$$

where $\mathbf{Z}$ is the matrix containing all the multiplier coefficients of the unknown constants C_n (with $n = 1, 2, 5, 6, 7, 8$), which are contained in the vector $\mathbf{C}$. The vector $\mathbf{L}$ includes the effects of the external load and the constant of the Winkler medium. Obviously the solution is now given by the inversion of $\mathbf{Z}$ matrix:

$$\mathbf{C} = \mathbf{Z^{-1}} \cdot \mathbf{L} \tag{5.135}$$

Elastic stage coefficients

In this section the transformation coefficients to obtain a SDOF system are developed according to the variational approach.
Firstly, on the basis of the elastic solution just outlined above, the elastic shape function is assumed as the ratio of the normalized deflection with respect to the maximum one:

$$\psi_{el}(r) = \frac{w(r)}{w_{max}} \tag{5.136}$$

Given the complexity of the expressions arising from an analytical integration of the above shape function, a numerical integration may be preferred in order to work out the transformation coefficients for the elastic stage. The method of numerical integration adopted herein is the so-called *midpoint rule* or *rectangle rule*, which permits to compute an approximation to a definite integral by finding the area of a collection of rectangles, whose heights are determined by the values of the function. This discretization process gives rise to the expressions reported below.
The generalized elastic mass is given by:

$$m_e^* = \int_0^{2\pi} \int_0^R \rho h \psi^2(r)\, r \,\mathrm{d}\theta \,\mathrm{d}r \tag{5.137}$$

$$= 2\pi\rho h \sum_{k=1}^{N_R} \psi_k^2\, k\triangle r^2 \tag{5.138}$$

where:

- $N_R = \frac{R}{\triangle r}$, being $\triangle r$ the spatial step for the numerical integration, defined as a fraction of R;
- $\psi_k = \psi(k\triangle r)$ is the elastic shape function evaluated in $r = k\triangle r$.

The generalized elastic stiffness is:

$$\begin{aligned} k_e^* &= D \int_0^{2\pi} \int_0^R \left[\left(\frac{\partial^2 \psi}{\partial r^2} + \frac{1}{r}\frac{\partial \psi}{\partial r} \right)^2 - 2(1-\nu)\left(\frac{\partial^2 \psi}{\partial r^2} \frac{1}{r}\frac{\partial \psi}{\partial r} \right) \right] r \,\mathrm{d}\theta \,\mathrm{d}r \\ &\quad + \int_0^{2\pi} \int_0^R k_s \psi^2\, r \,\mathrm{d}\theta \,\mathrm{d}r \qquad (5.139) \\ &= 2\pi D \sum_{k=1}^{N_R - 1} \left[\left(\frac{\triangle^2 \psi}{\triangle r^2} + \frac{1}{k\triangle r}\frac{\triangle \psi}{\triangle r} \right)^2 - 2(1-\nu)\left(\frac{\triangle^2 \psi}{\triangle r^2} \frac{1}{k\triangle r}\frac{\triangle \psi}{\triangle r} \right) \right] k\triangle r^2 \\ &\quad + 2\pi \sum_{k=1}^{N_R - 1} k_s \psi_k^2\, k\triangle r^2 \qquad (5.140) \end{aligned}$$

where the partial derivatives expressed in terms of finite differences are defined as follows:

$$\frac{\triangle \psi}{\triangle r} = \frac{\psi_{k+1} - \psi_k}{\triangle r} \tag{5.141}$$

$$\frac{\triangle^2 \psi}{\triangle r^2} = \frac{\triangle\left(\dfrac{\triangle \psi}{\triangle r}\right)}{\triangle r} = \frac{\psi_{k+2} - 2\psi_{k+1} + \psi_k}{\triangle r^2} \tag{5.142}$$

It should be noted that in the expression for the generalized stiffness (equation 5.140) appears a term dependent of k_s, being the term that takes into account the soil contribute.
The generalized load coefficient is:

$$p_e^* = p(t) \int_0^{2\pi} \int_0^b \psi(r)\, r\, \mathrm{d}\theta\, \mathrm{d}r \tag{5.143}$$

$$= p(t)\, 2\pi \sum_{k=1}^{N_b} \psi_k\, k \triangle r^2 \tag{5.144}$$

$$= p(t)\, L_e^* \tag{5.145}$$

where:

$$N_b = \frac{b}{\triangle r} \tag{5.146}$$

with b being the radius of the uniformly distributed loaded region.

5.3.2 Plastic mechanism and ultimate resistance

The problem of soil-structure interaction has been studied with great interest both by geotechnical and structural engineers for many years. Generally, the treatment of this problem is preferable approached by plastic or limit analysis methods instead of elastic methods. Plastic theories propose simpler methods of analysis, giving more reliable results which are less sensitive to the exact distribution of the contact stress between the foundation and the supporting soil than those of the elastic theories (Chen and Han, 1988).

In this section, the ultimate resistance load of concrete slabs on elastic foundation is studied. In literature many examples can be found which provide the upper bounds of the collapse load of a concrete slab, mainly under the title of *yield line theory* (Chen and Han, 1988). This approach was first introduced independently of the limit analysis theorems by Johansen (1972); in his book *Yield line formulae for slabs* many examples can be found about foundation slabs with different geometry and several boundary conditions along with their collapse load.

Let's consider now the load carrying capacity of a concrete slab under a central uniform load with a variable radius. The slab is assumed to rest on a linear elastic (Winkler) soil medium. The use of plastic methods requires the right collapse mechanism definition. This is not an easy task because the collapse mechanism will depend on the geometrical dimensions and on the elastic properties of the soil and of the slab. In this work, two collapse mechanisms are proposed: the first one (case 2.A) considers the formation of a negative circular yield line with an inverted cone shape inside of it, while the other mechanism (case 2.B) considers only the inverted cone shape originating from the plate edge.

Case 2.A involves a very flexible plate, namely a plate large enough in order to allow the formation of the circular yield line and low values of soil displacements at the plate edges. On the other hand, case 2.B involves very small and stiff plates with large values of soil displacements at the plate edges, with no formation of the circular yield line. These examples will be developed in the following subsections.

As it was exposed, case 2.A and case 2.B are opposite cases, so a mathematical tool is needed in order to distinguish one to the other. The collapse load depends on the radius d of the negative circular yield line, which is unknown (Meda, 2003). Meda proposes a very large slab supported on grade subjected to a concentrated load and the circular crack is assumed to occur at the location of the maximum negative moment. Westergaard (1926) indicates the maximum negative moment at $2l_c$ with l_c (characteristic length) equal to:

$$l_c = \sqrt[4]{\frac{D}{k_{soil}}} \tag{5.147}$$

Therefore, if $R < 2l_c$ there is no negative plasticization line. If $R > 2l_c$ there is a negative plasticization line, which can be computed according to the theory of Chen and Han (1988). The relation between R and $2l_c$ helps to distinguish between case 2.A and 2.B, but it should be remembered that other conditions regarding the soil displacement at the plate edges are required.

It has been noticed that different stiffness conditions will lead to different solutions; to address this issue the plot shown in figure 5.22 was developed.

As can be seen in this graph, when l_c is small (i.e., when the plate stiffness is small with respect to the soil one), $\psi_{el}(r = R)$ has decreasing values as R increases, meaning that the displacement at the plate edges is smaller when the plate is thinner and wider. In this last case, the midspan displacement is predominant with respect to the one at the plate extremities. On the contrary, when $\psi_{el}(r = R)$ increases, the displacement at the slab endings is predominant with respect to the midspan one. Summarizing, we could say that within this framework $\psi_{el}(r = R)$ is a representative parameter of the plate-soil system flexibility. Note that figure 5.22 was developed for $b = 0.1$ m and $h = 0.10$ m. By using the algorithms proposed in this work it is possible to draw figures like 5.22 for any value of b and h.

Knowing the geometrical dimensions (R, h, b) and the stiffness parameters (k_{soil}, D) of a plate-soil system, just placing a point in the graph 5.22 a designer can know if the conditions belong either to a very rigid plate or to a very flexible plate. In this work it has been supposed that values of $0.9 < \psi_{el}(r = R) < 1$ fulfil the hypothesis assumed for rigid plates with absence of the circular yield line, while values of $0 < psi_el(r = R) < 0.1$ fulfil the hypothesis assumed for very flexible plates with presence of the circular yield line. In this way, the plot could be used by the designer to distinguish between the two cases that will be presented and solved in the following subsections.

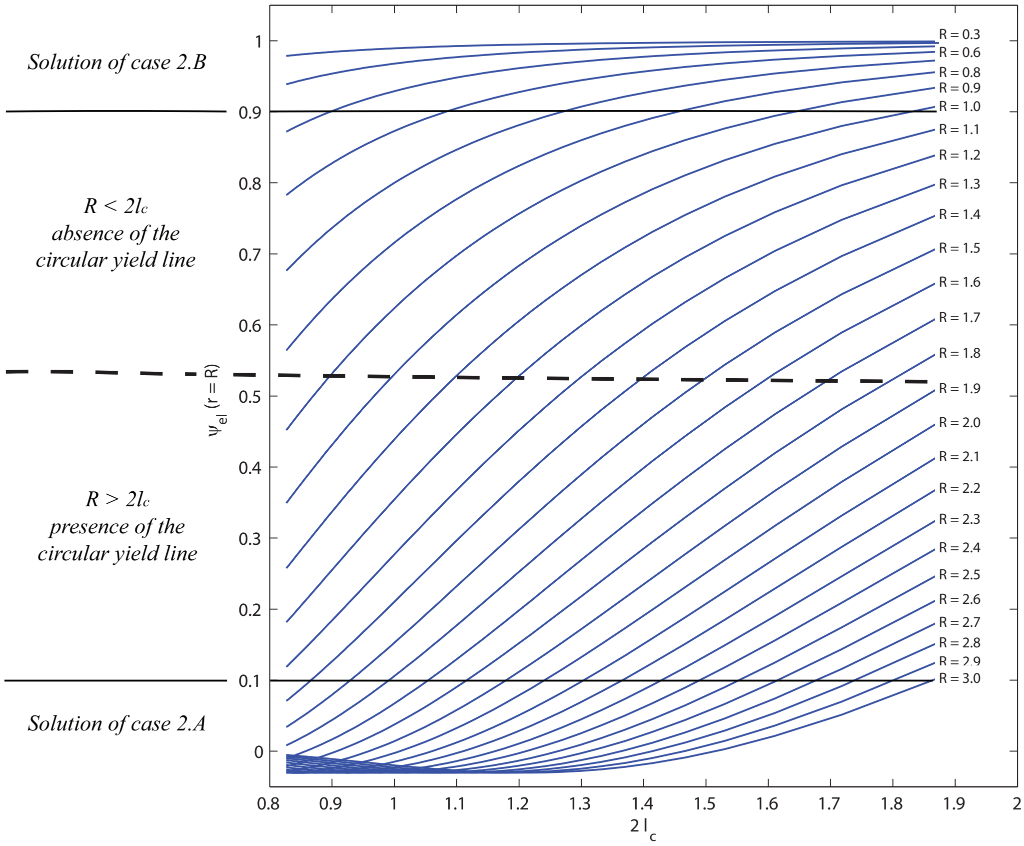

Figure 5.22: Variation of $\psi_{el}(r = R)$ as a function of the characteristic length $l_c = \sqrt[4]{D/k_{soil}}$ and of the plate radius R.

5.3.3 Case 2.A: presence of the negative circular yield line ($R > 2l_c$)

As the load p is applied to the concrete pavement over a circle of radius b, the slab would be driven into the soil until plastic radial moments are realized and a plastic mechanism develops in the slab, as shown in figure 5.23. This collapse mechanism was first studied by Chen and Han (1988) and consists of an infinite number of radial yield lines and a circular yield line of radius d. Therefore the plastic shape assumed in presence of the formation of a circular yield line has the following expression:

$$\psi_{pl}(r) = \begin{cases} 1 - \dfrac{r}{d} & \text{if } 0 \leq r \leq d, \\ 0 & \text{if } d < r \leq R. \end{cases} \tag{5.148}$$

In order to assume this shape function and the corresponding collapse mechanism herein described, it is necessary to satisfy the hypothesis that the elastic deformation at the slab edges $\psi_{el}(r = R)$ is very small with respect to the central deformation of the plate. Under this hypothesis it is reasonable to neglect the displacement at the slab edges, and to consider a plastic shape as defined by equation 5.148. With further increase of the load, the slab deforms into a conical surface but no sudden failure is observed; even though the external forces are increasing, the system is kept in equilibrium since also the soil reactions are increasing. However, the displacement rate under the applied external load grows rapidly at the formation of the failure mechanism until the load and the collapsed concrete sink into the ground (Chen and Han, 1988). The interest of limit analysis is to determine the load at which a plastic collapse mechanism develops in the slab. Thereby, in the following calculation, the soil reaction q is assumed to have a conical distribution with radius R.

The work done by the applied load W_p and by the upward soil reaction W_q are given by:

$$W_p = \int_0^{2\pi} \int_0^b p_0 \delta \left(1 - \frac{r}{d}\right) r \, \mathrm{d}\theta \, \mathrm{d}r \tag{5.149}$$

$$= 2\pi \frac{F_{su}}{\pi b^2} \delta \int_0^b \left(1 - \frac{r}{d}\right) r \, \mathrm{d}r \tag{5.150}$$

$$= F_{su} \delta \left(1 - \frac{2b}{3d}\right) \tag{5.151}$$

$$W_q = - \int_0^{2\pi} \int_0^d q_0 \left(1 - \frac{r}{R}\right) \delta \left(1 - \frac{r}{d}\right) r \, \mathrm{d}\theta \, \mathrm{d}r \tag{5.152}$$

$$= -2\pi q_0 \delta \int_0^d \left(1 - \frac{r}{R}\right) \left(1 - \frac{r}{d}\right) r \, \mathrm{d}r \tag{5.153}$$

$$\tag{5.154}$$

By enforcing the equilibrium between the load distribution and the soil reaction one can work out the value of q_0 as follows:

$$q_0 = \frac{3F_{su}}{\pi b^2} \tag{5.155}$$

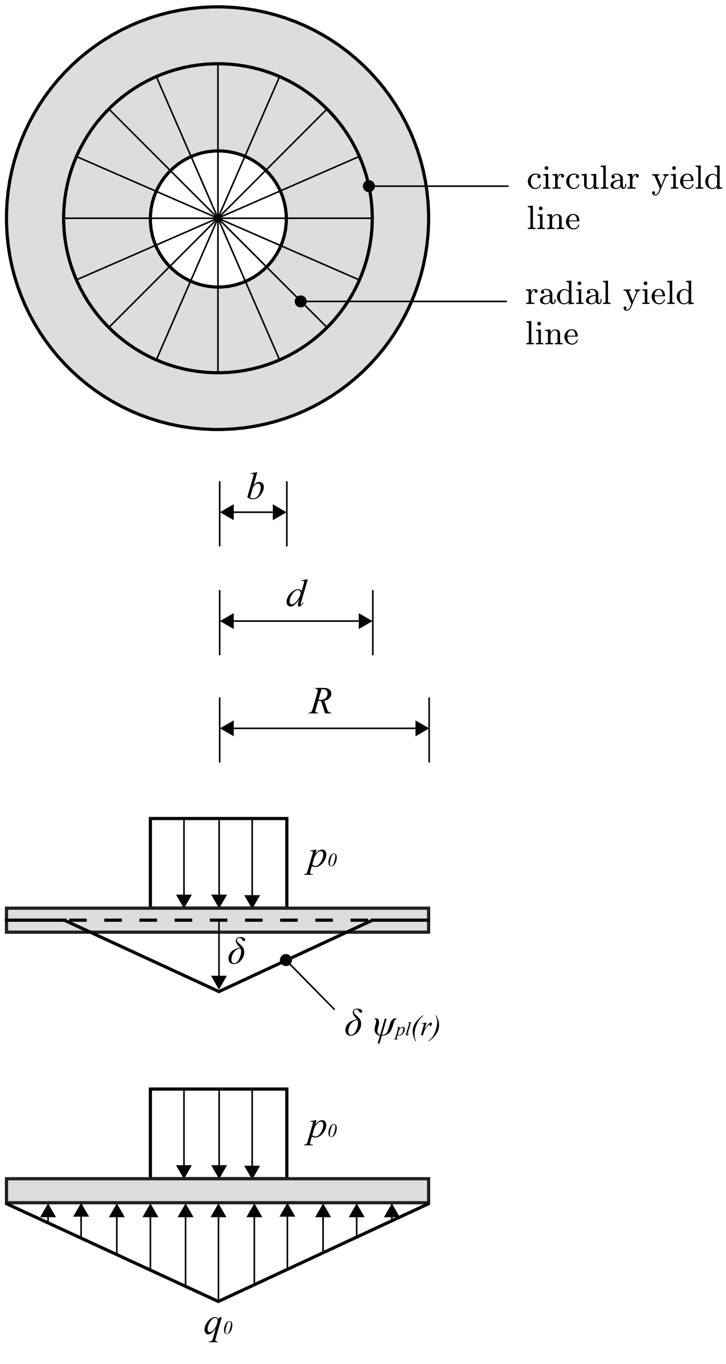

Figure 5.23: Case 2.A: failure mechanism and assumed pressure distribution.

By substituting this value into equation 5.154, one can finally get:

$$W_q = -2\pi \frac{3F_{su}}{\pi b^2} \delta \int_0^d \left(1 - \frac{r}{R}\right)\left(1 - \frac{r}{d}\right) r \,\mathrm{d}r \tag{5.156}$$

$$= -F_{su}\delta \left(\frac{d}{R}\right)^2 \left(1 - \frac{d}{2R}\right) \tag{5.157}$$

Now considering the internal works, with the deflection given, the rotation about the radial yield line in the θ direction ϕ_θ is easy to obtain as $\phi_\theta = \delta/(rd)$ (Chen and Han, 1988). Therefore the rate of internal energy dissipation per unit area is $m_0\delta/(rd)$. Integrating over the collapse area, one can get the total rate of energy dissipation:

$$W_r = 2\pi \int_0^d m_0 \frac{\delta}{rd} \,\mathrm{d}r = 2\pi m_0 \delta \tag{5.158}$$

Considering that the rotation about the circular yield line in the radial direction ϕ_d can simply be obtained as $\phi_d = \delta/d$, the internal energy dissipation worked out by the circular yield line has the following expression:

$$W_d = 2\pi d m_0 \delta/(d) = 2\pi m_0 \delta \tag{5.159}$$

The virtual work theorem states that:

$$W_E = W_I \tag{5.160}$$

that means:

$$W_p + W_q = W_r + W_d \tag{5.161}$$

From this work equation the ultimate resistance force [N] is obtained:

$$F_{su} = \frac{4\pi m_0}{1 - \frac{2}{3}\frac{b}{R}\frac{R}{d} - \left(\frac{d}{R}\right)^2 + \frac{1}{2}\left(\frac{d}{R}\right)^3} \tag{5.162}$$

The position of the circular yield line can be determined from the following minimization:

$$\frac{\partial F_{su}(d)}{\partial d} = 0 \tag{5.163}$$

This condition leads to the following quartic equation in the variable d:

$$\frac{9}{R^4}d^4 - \frac{12}{R^3}d^3 + 4\frac{b}{R} = 0 \tag{5.164}$$

which can be solved with the smart analytical method discovered by Ferrari, and first published in 1545 in Gerolamo Cardano's book *Ars Magna* (Cardano, 1993). The solution of this equation obviously yields four roots: two of them are complex, and the other two are real, but since one of them is always greater than the slab radius R, only one root actually has the sought physical meaning. Therefore, given the ratio b/R, the relative radius of the circular yield line d/R can be found from the previous equation. By substituting the value of d/R so obtained into the equation for $F_{su}(d)$, an upper bound ultimate resistance F_{su}

is obtained.
Equation 5.162 is plotted in figure 5.24 as a function of the relative load radius b/R. As expected, the graph shows a sharp increasing tendency as b/R increases until 0.75, due to the greater penetration of the plate into the soil.
Figure 5.25 clearly shows how the relative radius of the circular yield line d/R varies when the relative load radius b/R changes.

It can be observed that for values of $b/R > 0.75$ there is no more a negative circular yield line. This means that from a certain point on, the failure mechanism must switch from the one previously assumed to another conical mechanism which involves the entire slab area. Consequently, the ultimate resistance force changes and it is no more equal to the one given by the expression developed before (see case 2.B).

Note that, for this collapse mechanism, the inverted cone shape is formed after the circular yield line is developed. Therefore, the threshold value $\widetilde{w}_{max}$, expressed in equations 5.13 and 5.29, is evaluated for $R = d$, because in this case d represents the radius of the base of the inverted cone.

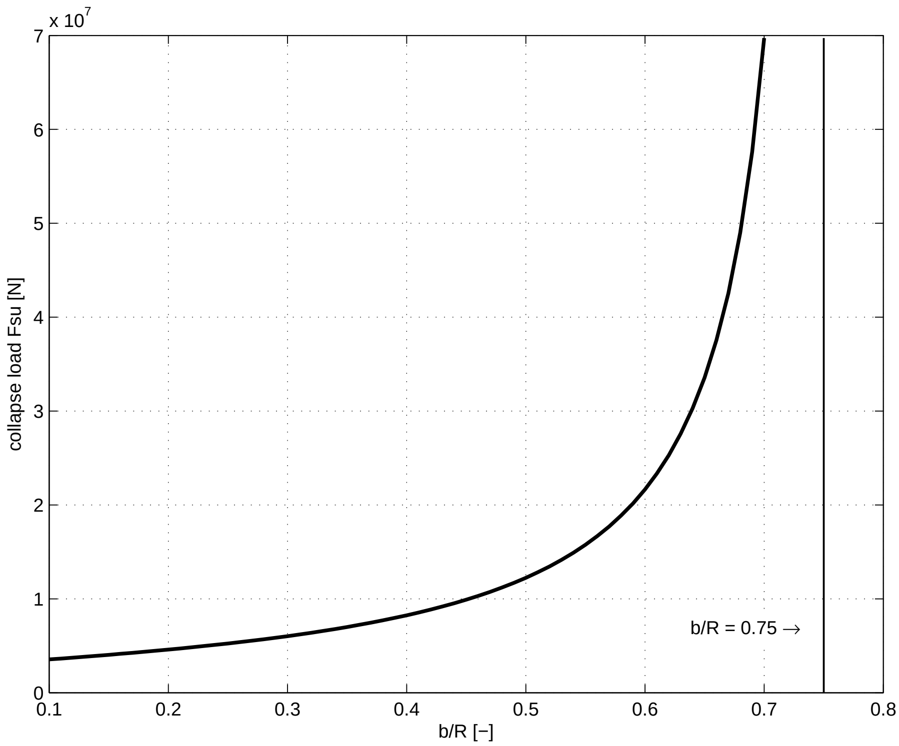

Figure 5.24: Case 2.A: relative load radius b/R vs collapse load F_{su}.

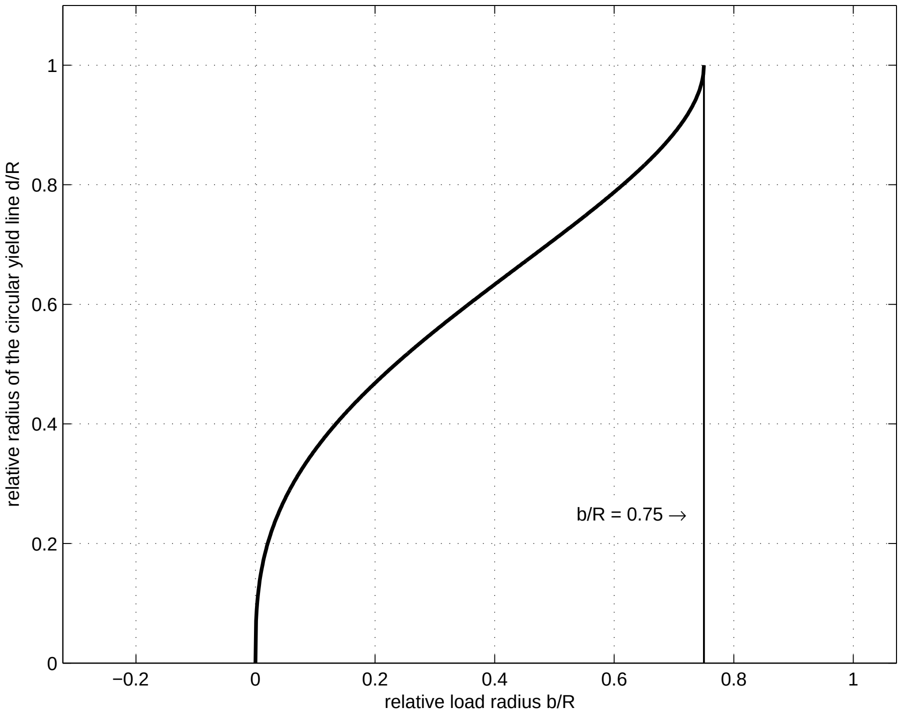

Figure 5.25: Relative load radius b/R vs relative radius of the circular yield line d/R.

Plastic stage coefficients

Considering the plastic shape function as described by equation 5.148, the plastic stage transformation coefficients are derived as follows:

$$m_p^* = \int_0^{2\pi} \int_0^d \rho h \psi^2(r)\, r\, d\theta\, dr \tag{5.165}$$

$$= 2\pi\rho h \int_0^d \left(1 - \frac{r}{d}\right)^2 r\, dr \tag{5.166}$$

$$= \frac{1}{6}\rho h \pi d^2 \tag{5.167}$$

$$k_p^* = 0 \tag{5.168}$$

$$p_p^* = p(t) \int_0^{2\pi} \int_0^b \psi(r)\, r\, d\theta\, dr \tag{5.169}$$

$$= 2\pi p(t) \int_0^b \left(1 - \frac{r}{d}\right) r\, dr \tag{5.170}$$

$$= p(t)\, 2\pi \left(\frac{b^2}{2} - \frac{b^3}{3d}\right) \tag{5.171}$$

$$= p(t)\, L_p^* \tag{5.172}$$

According to Biggs (1964):

$$K_M^p = \frac{m_p^*}{m_t} \tag{5.173}$$

$$K_R^p = 0 \tag{5.174}$$

$$K_L^p = \frac{p_p^*(t)}{p_t(t)} \tag{5.175}$$

where m_t is the total mass and $p_t(t)$ is the total load, which in this case is equal to $p_t(t) = p(t)\pi b^2$. Therefore by substitution the following normalized parameters can be obtained:

$$K_M^p = \frac{1}{6}\left(\frac{d}{R}\right)^2 \tag{5.176}$$

$$K_L^p = 1 - \frac{2}{3}\frac{b}{d} \tag{5.177}$$

Example of dynamic analysis

In the current example, a very flexible plate is modelled, large enough to develop a circular yield line. The data assumed to perform this analysis are the following ones:

Slab geometry:

- slab thickness $h = 0.10$ m;
- slab radius $R = 2.00$ m.

FRC reinforcement characteristics:

- $f_{eq1} = 5.34$ MPa;
- $f_{eq2} = 3.91$ MPa;
- $f_{ck} = 75$ MPa.

Load characteristics:

- load radius $b = 1.00$ m;
- peak pressure $p_{max} = 1$ MPa;
- total load time duration $t_d = 10$ ms;
- shape of the pulse: right-angle triangle.

Soil characteristics:

- Winkler constant $k_s = 0.10$ GPa/m (gravel).

In the current example all the data were hypothesized in order to obtain a very flexible plate, with a rigidity smaller than the soil one.
The dynamic analysis was run considering to reach three peaks in the displacement response before the analysis stopped (i.e., $n_{peaks} = 3$), as can be seen in figure 5.31.

First, stiffness and rigidity comparative parameters are calculated, obtaining $2l_c = 0.88$, then by using figure 5.22 with $R = 2$ m the problem's statement is placed in the case in which the plate is less rigid than the soil (i.e. $0 < \psi_{el}(r = R) < 0.1$).
In this case the plate's deformation is larger than the soil one, meaning that the energy dissipation is worked out, mostly, by the plate.
When, as in this case, the plate's rigidity is much smaller than the soil one, the deformation and the energy dissipated in the entire system is provided, practically, only by the plate. Figures 5.26 and 5.27 show this argument. The soil deformation is evidently much smaller than the plate deformation, which is very high in comparison.

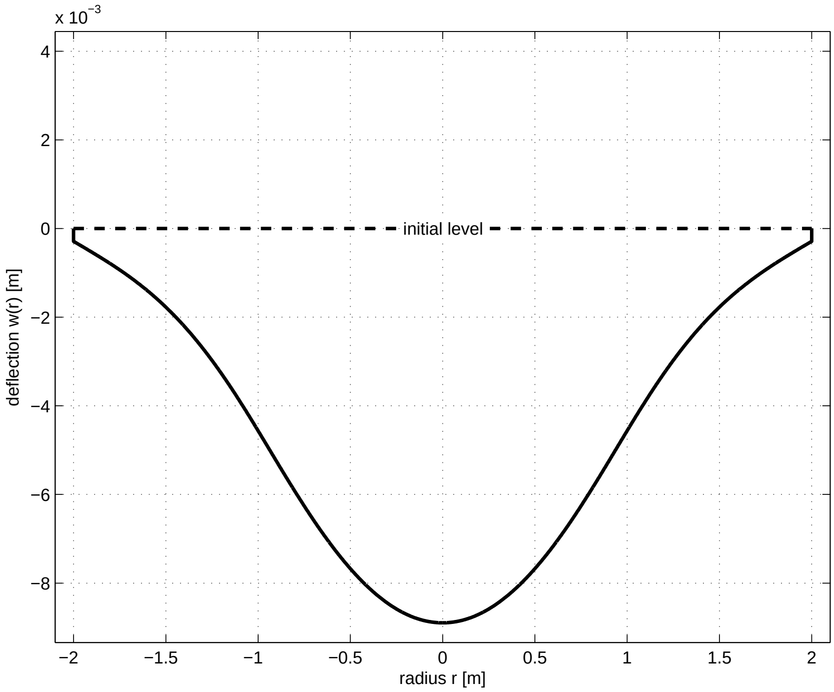

Figure 5.26: Case 2.A: elastic deformation.

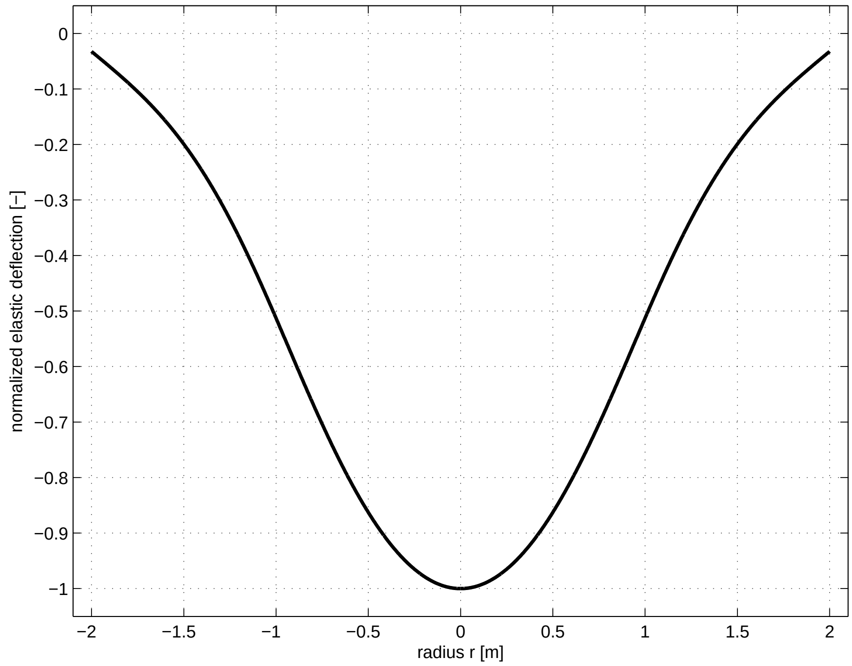

Figure 5.27: Case 2.A: normalized elastic shape of deformation.

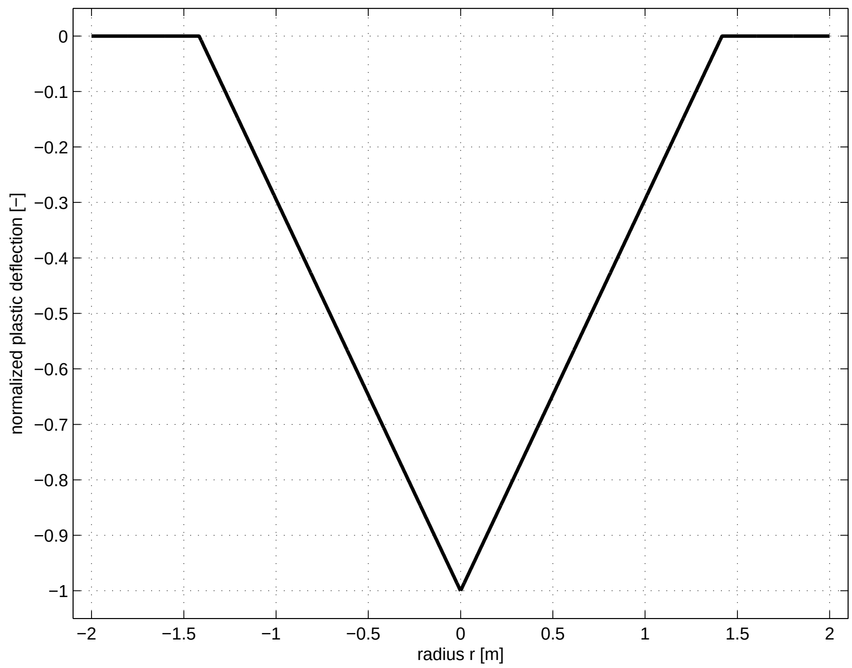

Figure 5.28: Case 2.A: plastic shape of deformation.

The elastic and plastic deformation profiles (figures 5.27 and 5.28) show a considerable difference between them and this is also evident in figure 5.29, where a remarkable step in the plot of the generalized load p^* corresponds to the change of behaviour from elastic to plastic one.

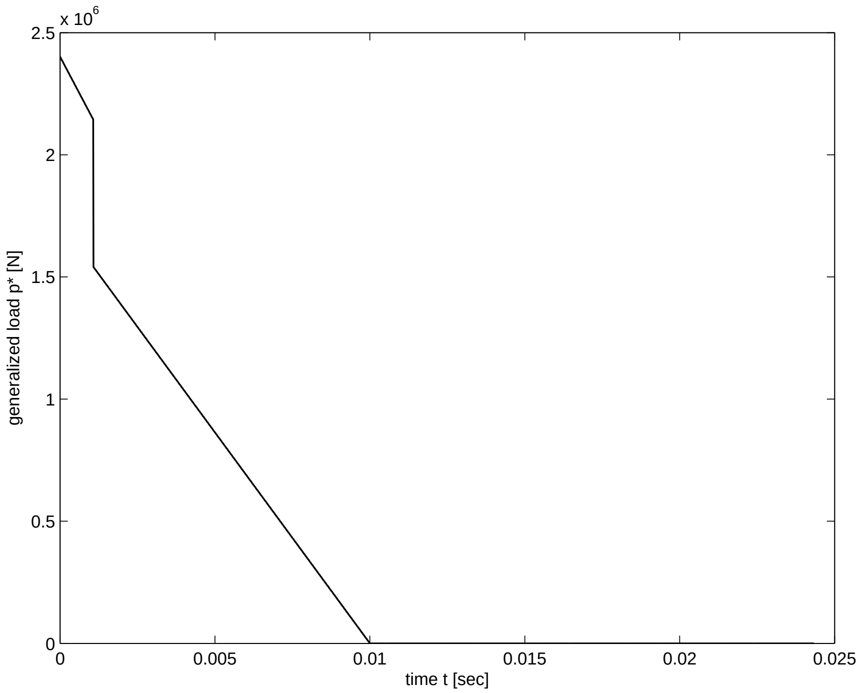

Figure 5.29: Case 2.A: generalized load vs time.

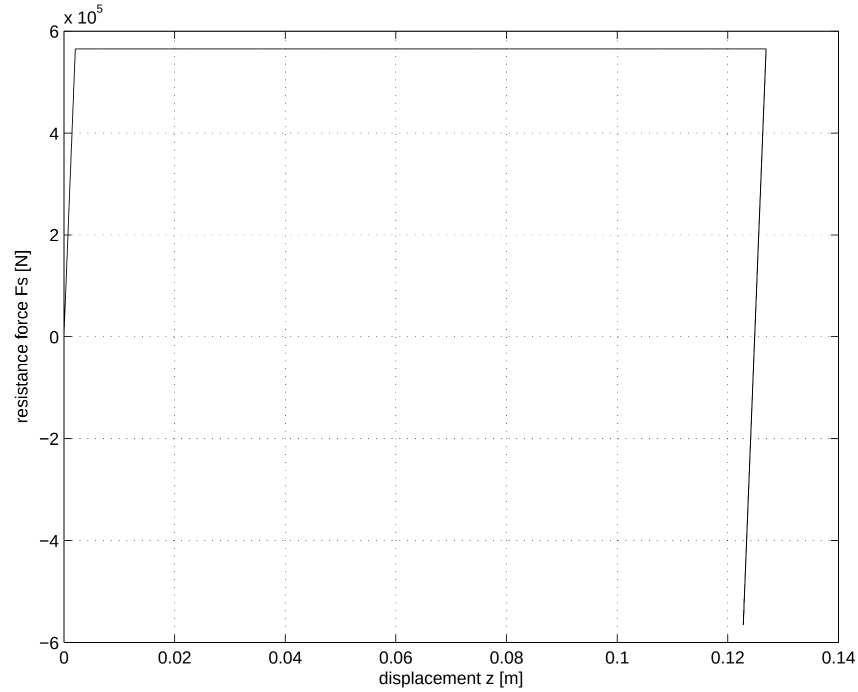

Figure 5.30: Case 2.A: mid-span displacement versus resistance force.

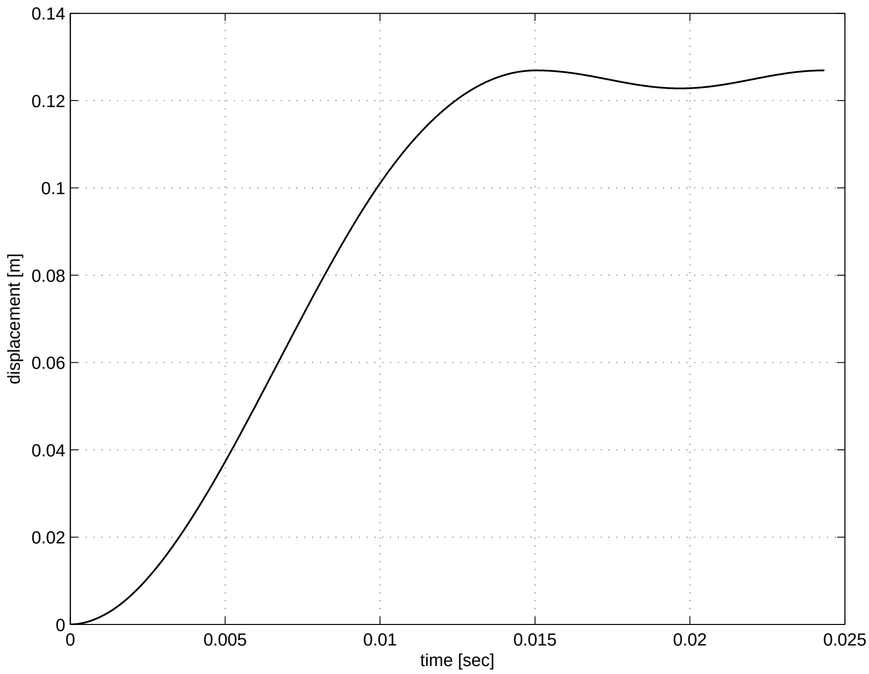

Figure 5.31: Case 2.A: mid-span displacement versus time.

As can be seen in figure 5.32, at around 1 ms the plastic stage is reached and the shape function changes from the elastic one to the plastic one. At about 15 ms the plasticization of the system ends and the elastic branch is followed again according to the unloading path.

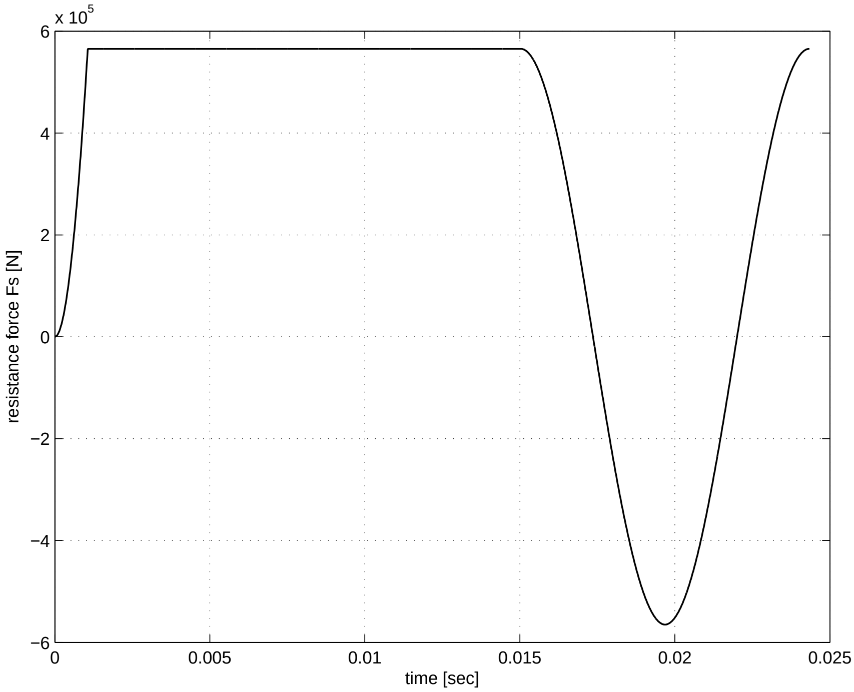

Figure 5.32: Case 2.A: resistance force versus time.

5.3.4 Case 2.B: absence of the negative yield line ($R < 2l_c$)

Due to the absence of the circular yield line, the expected collapse mechanism has an inverted cone shape where the radial yield lines appear progressively during the loading process. For this case, it is known that the plate is much more rigid than the soil, then a greater deformation of the soil with respect to the one of the plate is expected.
The collapse mechanism proposed in this section considers that the reaction of the soil has a rectangular distribution (see figure 5.34), disregarding the very small triangular distribution provided by the very small deformation of the plate. As was previously mentioned, it was decided that this hypothesis holds if the plate deformation is lower than the 10% of the total system displacement, or, equivalently, if the elastic displacement at the plate borders must be greater than the 90% of the total system's displacement.
According to the hypotheses just explained, the assumed plastic shape is:

$$\psi_{pl}(r) = 1 - (1 - \psi_{el}(r = R))\,\frac{r}{R} \tag{5.178}$$

During the stage of definition of this shape, it was thought to include in it the term $\psi_{el}(r = R)$ that takes into account the displacement at the plate extremities which has been reached at the end of the preceding elastic stage. In other words, the term $\psi_{el}(r = R)$ corresponds to the elastic displacement at the plate's edges achieved just before reaching the plastic stage. The assumed plastic shape for this case is graphically visualized in figure 5.33.
Going through the procedure developed below by using the upper-bound theory and the principle of virtual works, it is feasible to obtain the expression of F_{su}. Considering the plastic shape as defined by equation 5.178, the external work rate done by the applied load is:

$$W_p = \int_0^{2\pi}\int_0^b p_0\,\delta\,\psi_{pl}\,r\,\mathrm{d}\theta\,\mathrm{d}r \tag{5.179}$$

$$= 2\pi\int_0^b p_0\,\delta\left[1 - (1 - \psi_{el}(R))\,\frac{r}{R}\right] r\,\mathrm{d}r \tag{5.180}$$

$$= 2\pi\,p_0\,\delta\left[\frac{b^2}{2} - (1 - \psi_{el}(R))\,\frac{b^3}{3\,R}\right] \tag{5.181}$$

The external work rate done by the soil reaction is:

$$W_q = -\int_0^{2\pi}\int_0^R q_0\,\delta\,\psi_{pl}\,r\,\mathrm{d}\theta\,\mathrm{d}r \tag{5.182}$$

$$= -2\pi\int_0^R q_0\,\delta\left[1 - (1 - \psi_{el}(R))\,\frac{r}{R}\right] r\,\mathrm{d}r \tag{5.183}$$

$$= -2\pi\,q_0\,\delta\left[\frac{R^2}{2} - (1 - \psi_{el}(R))\,\frac{R^2}{3}\right] \tag{5.184}$$

By means of static equilibrium between plate load and soil reaction one can work out:

$$q_0 = p_0\left(\frac{b}{R}\right)^2 \tag{5.185}$$

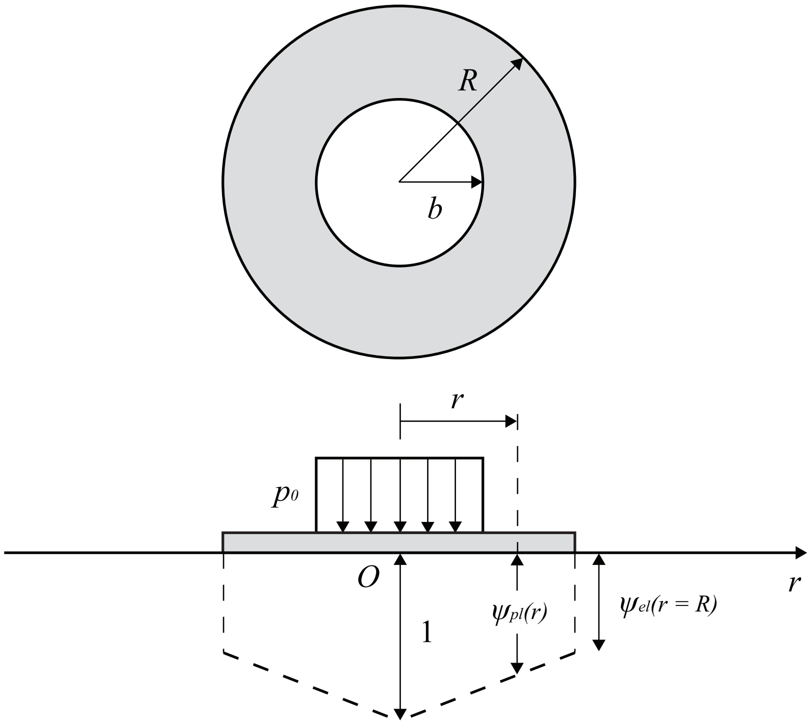

Figure 5.33: Case 2.B: plastic shape of deflection.

Finally:

$$W_q = -2\pi\, p_0\, \delta \left[\frac{b^2}{2} - (1 - \psi_{el}(R))\, \frac{b^2}{3} \right] \tag{5.186}$$

The total external work is:

$$W_E = W_p + W_q = 2\pi\, p_0\, \delta\, (1 - \psi_{el}(R))\, \frac{b^2}{3} \left(1 - \frac{b}{R} \right) \tag{5.187}$$

The internal work is given by:

$$W_I = 2\pi m_0 \delta\, (1 - \psi_{el}(R)) \tag{5.188}$$

The virtual work theorem states that:

$$W_E = W_I \tag{5.189}$$

Therefore the ultimate resistance force [N] is:

$$F_{su} = p_0(\pi b^2) = \frac{3\pi\, m_0}{1 - \dfrac{b}{R}} \tag{5.190}$$

Note that the collapse load F_{su} does not depend on $\psi_{el}(r = R)$. Equation 5.190 is plotted in figure 5.35. This plot clearly shows that, when the load tends to occupy the entire slab surface, the resistance of the plate tends to infinite, meaning that the plate simply penetrates in the soil, and this is consistent with the theory previously discussed.

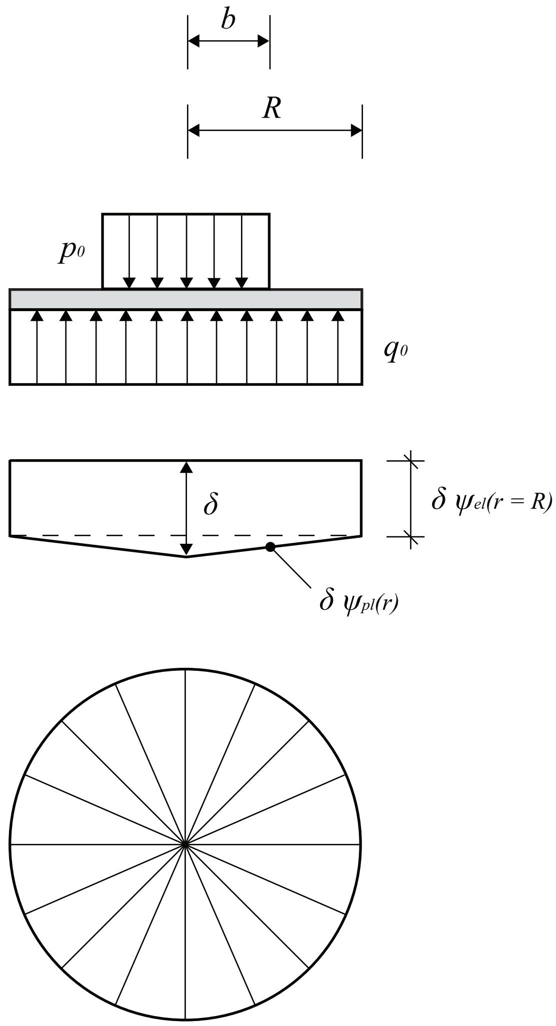

Figure 5.34: Case 2.B: failure mechanism and assumed pressure distribution.

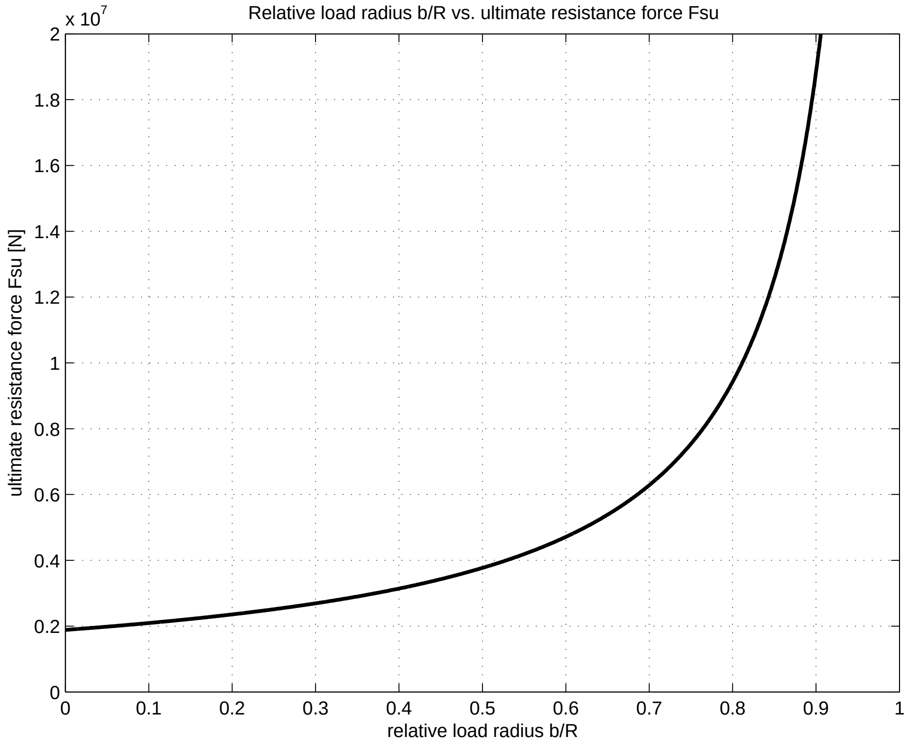

Figure 5.35: Case 2.B: relative load radius versus ultimate resistance load.

Plastic stage coefficients

Considering the plastic shape function as defined by equation 5.178, one can work out the transformation coefficients for the plastic stage. The plastic coefficients are thus given by:

$$m_p^* = \int_0^{2\pi}\int_0^R \rho\, h\, \psi_{pl}^2(r)\, r\, \mathrm{d}\theta\, \mathrm{d}r \tag{5.191}$$

$$= \pi R^2\, \rho\, h \left(\frac{1}{6} + \frac{1}{3}\,\psi_{el}(R) + \frac{1}{4}\,\psi_{el}^2(R)\right) \tag{5.192}$$

$$k_p^* = 0 \tag{5.193}$$

$$p_p^* = p(t)\int_0^{2\pi}\int_0^R \psi_{pl}(r)\, r\, \mathrm{d}\theta\, \mathrm{d}r \tag{5.194}$$

$$= p(t)\, 2\pi \left[\frac{b^2}{2} + \frac{b^3}{3R}\,(\psi_{el}(R) - 1)\right] \tag{5.195}$$

$$= p(t)\, L_p^* \tag{5.196}$$

Example of dynamic analysis

In the current example, a very rigid plate in which there is no development of the circular yield line is modelled. Dimensions and material characteristics try to represent a shock tube specimen.
The data assumed to perform this analysis are the following ones:

Slab geometry:

- slab thickness $h = 0.10$ m;
- slab radius $R = 0.29$ m.

FRC reinforcement characteristics:

- $f_{eq1} = 5.34$ MPa;
- $f_{eq2} = 3.91$ MPa;
- $f_{ck} = 75$ MPa.

Load characteristics:

- load radius $b = 0.24$ m;
- peak pressure $p_{max} = 2.6$ MPa;
- total load time duration $t_d = 10$ ms;
- shape of the pulse: right-angle triangle.

Soil characteristics:

- Winkler constant $k_s = 0.03$ GPa/m (dense sand).

The load radius b and the Winkler constant were chosen in order to simulate the characteristics of a typical specimen in a shock tube test. In fact, the plate specimen of radius 29 cm will be subjected to a uniform pressure distribution having radius equal to 24 cm. Moreover, the plate will be supposed to rest on dense sand, thus the soil modulus is selected accordingly.
The dynamic analysis was run considering to reach three peaks in the displacement response before the analysis stopped (i.e., $n_{peaks} = 3$).

First, stiffness and rigidity comparative parameters are calculated, obtaining $2l_c = 1.2$, then by using figure 5.22 with $R = 0.29$ m the problem's statement is placed in the case in which the plate is much more rigid than the soil (i.e. $0.9 < \psi_{el}(r = R) < 1$).
When, as in this case, the plate's rigidity is much greater than the soil one, the deformation and the energy dissipated in the entire system is mainly provided by the soil. Figure 5.36 shows this argument. The soil deformation is evidently much higher than the plate deformation, which is very small in comparison.

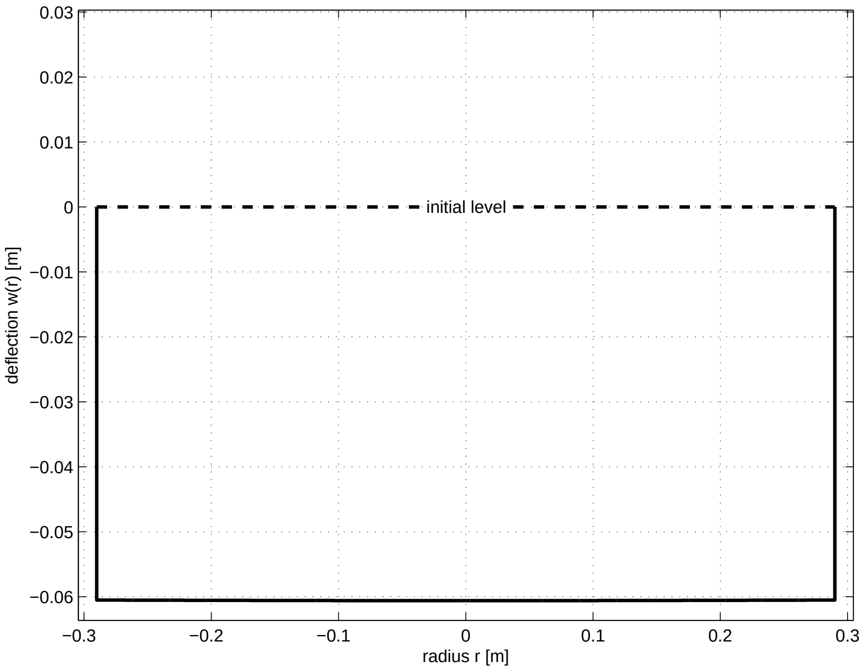

Figure 5.36: Case 2.B: elastic deformation.

Figure 5.37 illustrates the normalized plate's deformation. The elastic shape of deformation just describes the elastic qualitative form; due to the fact that the deformation magnitude is very low, looking at the vertical axis one can see that the border's displacement respect to the central one is about 0.14% (flat slope profile).

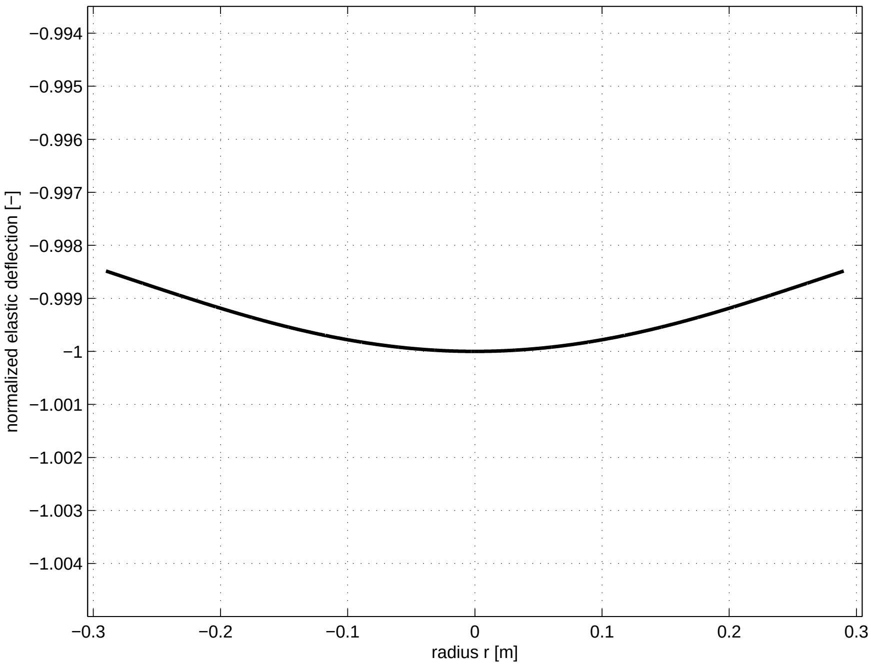

Figure 5.37: Case 2.B: normalized elastic shape of deformation.

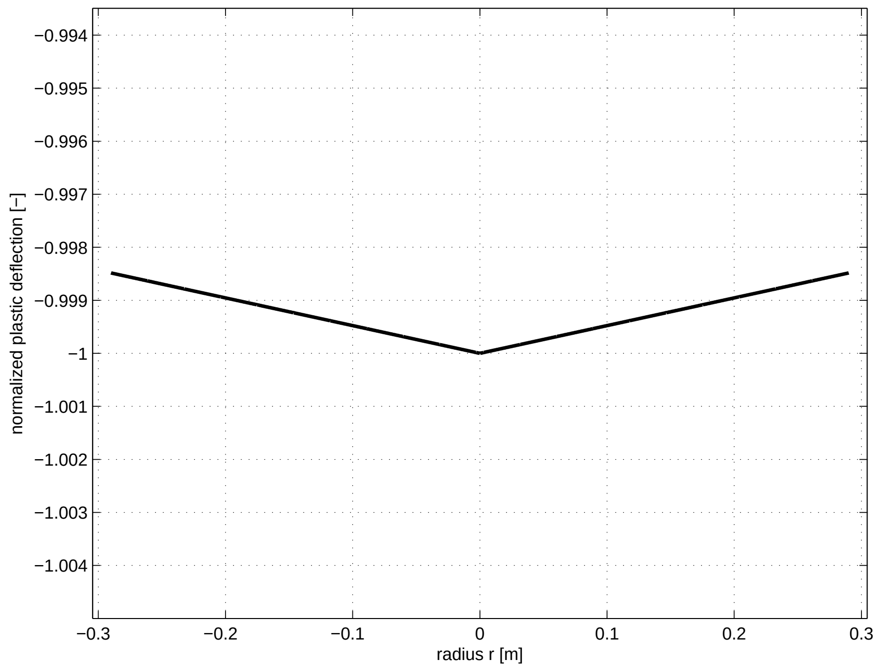

Figure 5.38: Case 2.B: plastic shape of deformation.

At around 5.5 ms the plastic stage is reached and the shape function changes from the elastic one to the plastic one (see figure 5.42), therefore in the generalized parameters there should be a change corresponding to this passing. In figure 5.39, which plots the generalized load p^* against time, there are no evident changes or steps in the graph, because the elastic and plastic shapes of deformation are very flat and similar one to the other, so the change of shape function is not perceivable.

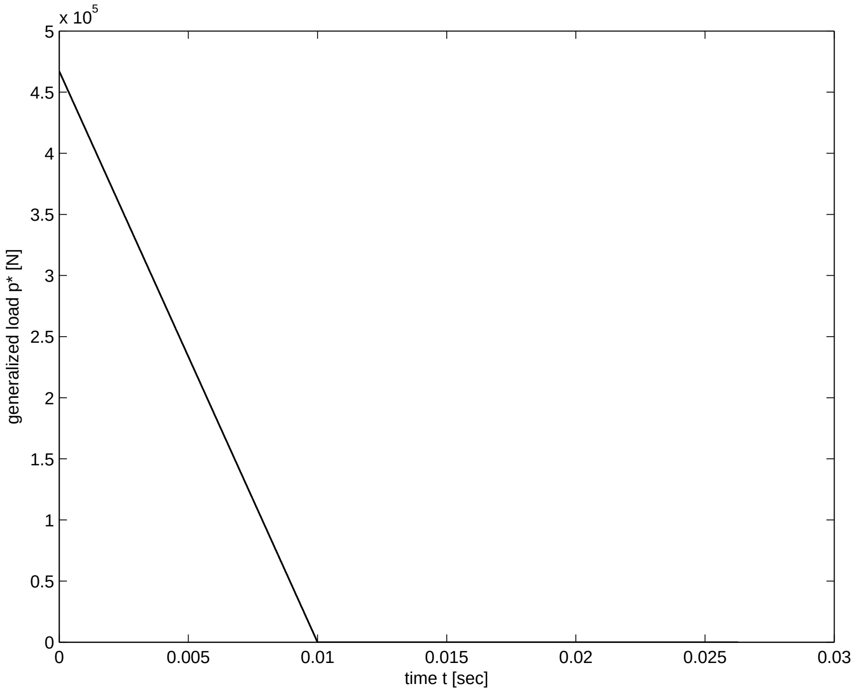

Figure 5.39: Case 2.B: generalized load vs time.

The system reaches the plastic phase in the first cycle and, after that, several cycles of loading and unloading are developed, reaching almost the negative plastic phase (see figures 5.40 and 5.42).

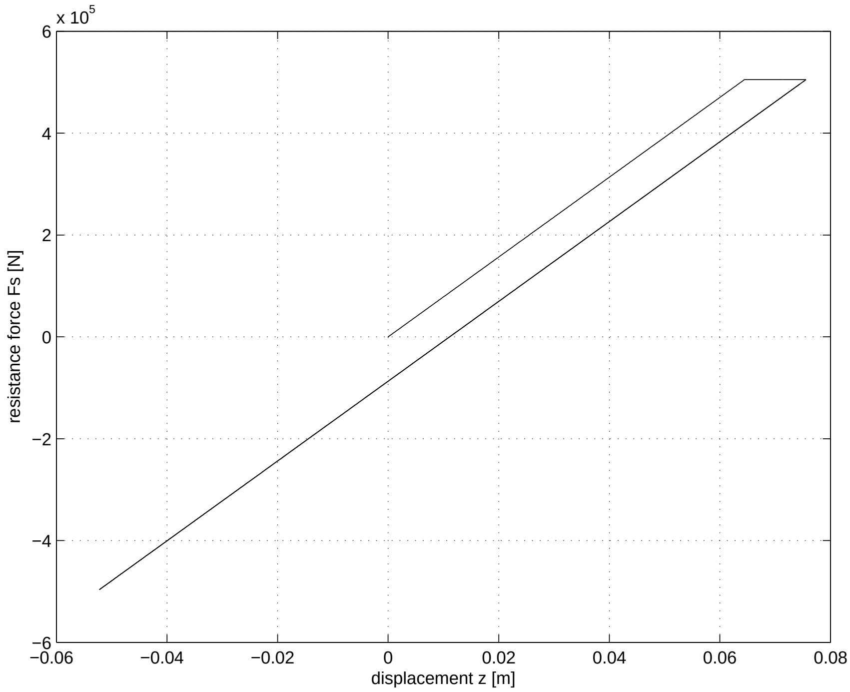

Figure 5.40: Case 2.B: mid-span displacement versus resistance force.

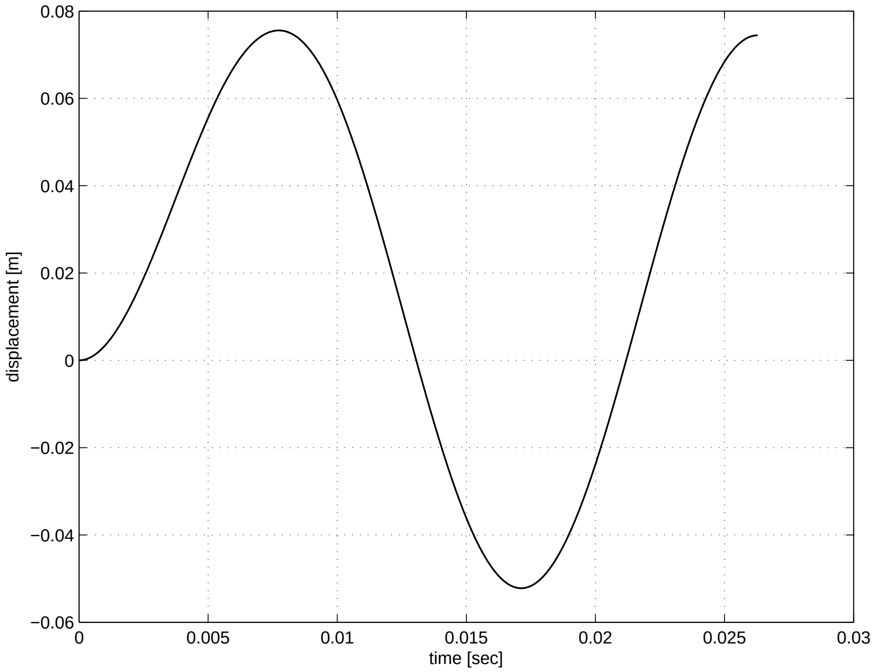

Figure 5.41: Case 2.B: mid-span displacement versus time.

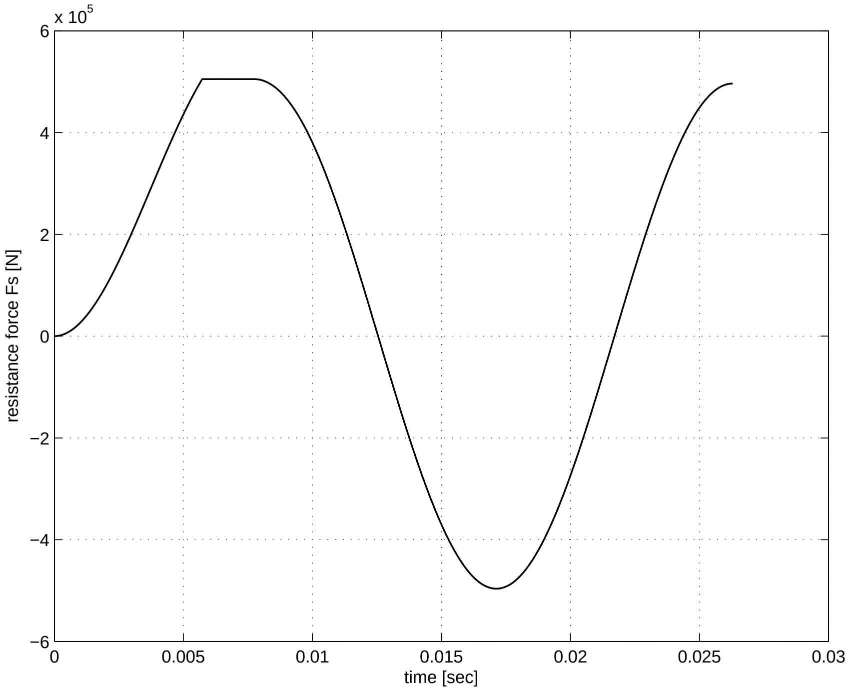

Figure 5.42: Case 2.B: resistance force versus time.

5.3.5 Pressure-impulse diagrams

Putting into practice the concepts already seen in chapter 4, this section develops all the calculations in order to derive the p-i diagrams.
The calculation of the asymptotes takes advantage of the energetic approach described in the previous chapter, for which it is necessary to compute the maximum external energy, the maximum kinetic energy and the maximum internal energy dissipated by the system.
It will be found that there are two cases for computing the maximum internal energy depending on the allowable threshold displacement $\widetilde{w}_{max}$, because this value may lie in the elastic phase or in the plastic one according to the characteristics of the generalized system.
After the asymptotes calculation, the p-i curve is derived with the algorithms proposed in chapter 4, namely by means of iterative calculations.

Kinetic energy. Referring to the generic plate element as represented in figure 5.14, one can compute the kinetic energy as follows:

$$K = \int\int_S \frac{1}{2}\,\overline{m}\,v_0^2\,\mathrm{d}S = \int_0^{2\pi}\int_0^b \frac{1}{2}\,\rho\,h\,v_0^2\,r\,\mathrm{d}\theta\,\mathrm{d}r \tag{5.197}$$

where v_0 is the initial velocity, which can be defined exploiting the momentum definition according to the impulse theorem:

$$v_0 = \frac{I}{m} = \frac{i\,r\,\mathrm{d}\theta\,\mathrm{d}r}{\rho\,h\,r\,\mathrm{d}\theta\,\mathrm{d}r} = \frac{i}{\rho\,h} \tag{5.198}$$

being I the total impulse, i the specific impulse and $m = \rho\,h\,r\,\mathrm{d}\theta\,\mathrm{d}r$ the total mass of the plate element. Finally the expression of the kinetic energy can be rewritten as:

$$K = 2\pi\rho h\frac{1}{2}\int_0^b \frac{i^2}{\rho^2\,h^2}\,r\,\mathrm{d}r = \frac{i^2\pi b^2}{2\rho h} \tag{5.199}$$

A) Case in which $\widetilde{w}_{max} < w_{el}$

Elastic strain energy. When the selected damage threshold is smaller than the displacement at the elastic limit (namely $\widetilde{w}_{max} < w_{el}$), the strain energy is simply represented by the elastic one, as was shown in figure 5.16.

$$U_{el} = \frac{1}{2}\,k_e^*\,\widetilde{w}_{max}^2 \tag{5.200}$$

Maximum possible work. When the selected damage threshold is smaller than the displacement at the elastic limit (namely $\widetilde{w}_{max} < w_{el}$), the shape function to assume in the computation of the maximum possible work is the elastic one.

$$W_{max}^{el} = \int\int_S p(r)w(r)\mathrm{S} = \int_0^{2\pi}\int_0^b p_0 w(r)\,r\,\mathrm{d}\theta\,\mathrm{d}r \tag{5.201}$$

Recalling that the elastic shape function for case 2 was defined in a numerical way, the discretization process yields to the following expression for the maximum possible work:

$$W_{max}^{el} = \widetilde{w}_{max} \left[2\pi\, p_0 \sum_{k=1}^{N_b} \psi_{el}(k\triangle r)\, k\triangle r^2 \right] \tag{5.202}$$

Quasi-static asymptote. By exploiting the definition that permits to work out the quasi-static asymptote as it was presented in the previous chapter:

$$U_{el} = W_{max}^{el} \tag{5.203}$$

and performing the needed substitutions one can get:

$$\frac{1}{2}\, k_e^*\, \widetilde{w}_{max}^2 = \widetilde{w}_{max} \left[2\pi\, p_0 \sum_{k=1}^{N_b} \psi_{el}(k\triangle r)\, k\triangle r^2 \right] \tag{5.204}$$

Finally the quasi-static asymptote has the following expression:

$$q.s.a. = p_0 = \frac{k_e^*}{4\pi\, \sum_{k=1}^{N_b} \psi_{el}(k\triangle r)\, k\triangle r^2}\, \widetilde{w}_{max} \tag{5.205}$$

Recalling that:

$$L_e^* = 2\pi \sum_{k=1}^{N_b} \psi_{el}(k\triangle r)\, k\triangle r^2 \tag{5.206}$$

(which is the multiplier coefficient to get the generalized load in the elastic stage), equation 5.205 can be rewritten in a compact form as follows:

$$q.s.a. = \frac{k_e^*}{2L_e^*}\, \widetilde{w}_{max} \tag{5.207}$$

from which it is clear that the quasi-static asymptote is dependent of stiffness and geometric characteristics.

Impulsive asymptote. As was done previously talking about case 1, the impulsive asymptote can be obtained by exploiting the following equation:

$$K = U_{el} \tag{5.208}$$

Substituting equations 5.199 and 5.200 into the previous expression:

$$\frac{i^2 \pi b^2}{2\rho h} = \frac{1}{2}\, k_e^*\, \widetilde{w}_{max}^2 \tag{5.209}$$

Equation 5.209 can be rewritten in compact form as follows, working out the impulsive asymptote:

$$i.a. = \sqrt{\frac{2\overline{m}\, U_{el}}{A_{load}}} \tag{5.210}$$

where $\overline{m} = \rho\, h$ is the specific mass per unit area and $A_{load} = \pi b^2$ is the plate area occupied by the load.

B) Case in which $\widetilde{w}_{max} > w_{el}$

Elastoplastic strain energy. When the selected damage threshold is greater than the displacement at the elastic limit (i.e. $\widetilde{w}_{max} > w_{el}$), the strain energy is represented by the sum of the elastic and plastic ones, as can be seen in figure 5.17. In the calculation of the maximum possible work both the elastic and plastic contributes will be considered. The energy will be computed assuming that the damage threshold $\widetilde{w}_{max}$ is reached during the first cycle, namely in the loading branch and not in the unloading one, thus excluding the possibility of obtaining a negative work contribute.
Under this hypothesis, the elastoplastic strain energy is equal to:

$$U_{ep} = U_{el} + U_{pl} = \frac{w_{el} \cdot F_{su}}{2} + (\widetilde{w}_{max} - w_{el})F_{su} = F_{su}\left(\widetilde{w}_{max} - \frac{w_{el}}{2}\right) \quad (5.211)$$

Maximum possible work. When $\widetilde{w}_{max} > w_{el}$, both the contributes of the elastic and plastic stages to the total work must be considered.

$$W^{ep}_{max} = p^{*el}_{max}\, w_{el} + p^{*pl}_{max}\, (\widetilde{w}_{max} - w_{el}) \quad (5.212)$$

$$= L^*_e\, p_0\, w_{el} + L^*_p\, p_0\, (\widetilde{w}_{max} - w_{el}) \quad (5.213)$$

where L^*_e and L^*_p are the multiplier coefficients to get the generalized load in the elastic stage and plastic stage, respectively.

$$L^*_e = 2\pi \sum_{k=1}^{N_b} \psi_{el}(k\triangle r)\, k\triangle r^2 \quad (5.214)$$

It should be remembered that the value of L^*_p changed according to the assumed plastic shape function. This means that, in case 2.A (presence of the circular yield line), the value of L^*_p is given by:

$$L^*_p = 2\pi\left[\frac{b^2}{2} - \frac{b^3}{3d}\right] \quad (5.215)$$

On the other hand, in absence of the circular yield line (case 2.B), the value of L^*_p is provided by:

$$L^*_p = 2\pi\left[\frac{b^2}{2} - (1 - \psi_{el}(r = R))\,\frac{b^3}{3R}\right] \quad (5.216)$$

Quasi-static asymptote. As was done previously, the expression for the quasi-static asymptote is exploited:

$$U_{ep} = W^{ep}_{max} \quad (5.217)$$

which yields, together with equations 5.211 and 5.213:

$$F_{su}\left(\widetilde{w}_{max} - \frac{w_{el}}{2}\right) = L^*_e\, p_0\, w_{el} + L^*_p\, p_0\, (\widetilde{w}_{max} - w_{el}) \quad (5.218)$$

The last equality provides the expression for the quasi-static asymptote:

$$q.s.a. = p_0 = \frac{U_{ep}}{L^*_e\, w_{el} + L^*_p\, (\widetilde{w}_{max} - w_{el})} \quad (5.219)$$

Impulsive asymptote. Also here the procedure is the same that was previously followed, namely by making use of the equation:

$$K = U_{ep} \tag{5.220}$$

and recalling equation 5.199 and 5.211, one can get:

$$\frac{i^2 \pi b^2}{2\rho h} = F_{su}\left(\widetilde{w}_{max} - \frac{w_{el}}{2}\right) \tag{5.221}$$

Rearranging the last equation one can finally achieve the expression for computing the impulsive asymptote:

$$i.a. = i = \sqrt{\frac{2\rho\, h\, F_{su}\left(\widetilde{w}_{max} - \frac{w_{el}}{2}\right)}{\pi\, b^2}} \tag{5.222}$$

Equation 5.222 can be rewritten in a compact form as follows:

$$i.a. = \sqrt{\frac{2\overline{m}\, U_{ep}}{A_{load}}} \tag{5.223}$$

where $\overline{m} = \rho\, h$ is the specific mass per unit area and $A_{load} = \pi b^2$ is the plate area occupied by the load.

At this point, it is useful to highlight some concepts treated in the previous sections. In the case 1, it was explained the variability of $\widetilde{w}_{max}/w_{el}$ with respect to R, in an explicit algebraic form. For this case, it is not so easy to explain this relation because all the formulations are complex and solved using numerical algorithms. Thereby it is not possible to follow the same procedure as in the case 1, because the boundary conditions in the case 2 are completely different and depending on the values of k_{soil}. Besides, another geometrical variable b (load radius) appears, making this analysis even more complex. In fact, the relation of $\widetilde{w}_{max}/w_{el}$ is not only dependent on the plate's geometrical dimensions (R, h), but also depends on the charge's dimension (b). Moreover, the value of F_{su} has a strong dependence of b/R (see figures 5.24 and 5.35). It has been observed that, when the value of b/R is close to 0.75 for case 2.A and to 1.0 for case 2.B, F_{su} increases in a very fast way, tending to infinitive. Recalling that $w_{el} = F_{su}/k_e^*$, it can be seen that, for large values of F_{su}, w_{el} increases. Due to the increasing of F_{su}, the relation $\widetilde{w}_{max}/w_{el}$ tends to decrease.

Let's remember that the case 2.A is limited to small values of $\psi_{el}(r = R)$ (edges' displacement), thus, in order to meet this condition, values of b/R must be small enough as well. Thereby, the ratio $\widetilde{w}_{max}/w_{el}$ will probably remain greater than 1 for most of the cases, meaning that $\widetilde{w}_{max}$ is more likely to fall into the plastic stage.

On the other hand, the case 2.B works with high values of $\psi_{el}(r = R)$ and, for that reason, it will be more likely to find values of $\widetilde{w}_{max}/w_{el}$ lower than 1, but this will happen just for special combination of R, b, h and material properties.

Let's remember that the value of $\widetilde{w}_{max}$ represents a limit value of the midspan displacement obtained according to a chosen criterion; for this reason it is worth noting that such criterion does not necessarily imply that the system is completely plasticised when the midspan displacement reaches $\widetilde{w}_{max}$.

Plotted diagrams

As was done for the case 1, in this section some results of p-i diagrams will be presented. The results illustrated as follows correspond to circular plates made in RC and FRC. The geometrical and material properties are assumed as the same values taken from the dynamic analysis example; however these data are written inside the figures. The chosen excitation pulse shape is a decreasing exponential function, with the parameter λ set equal to 5, in order to have a more realistic representation of a blasting load shape. The value of w_{max} is recorded in the figures and corresponds to the threshold displacement.

RC. The following example (figure 5.43) shows the p-i curve generated by using the algorithms proposed in this work. The geometrical dimensions and RC material properties were adopted in order to obtain a very flexible plate which allows for the formation of the negative circular yield line. Gravel ($k_s = 0.10$ GPa/m) was chosen in order to represent the supporting soil.

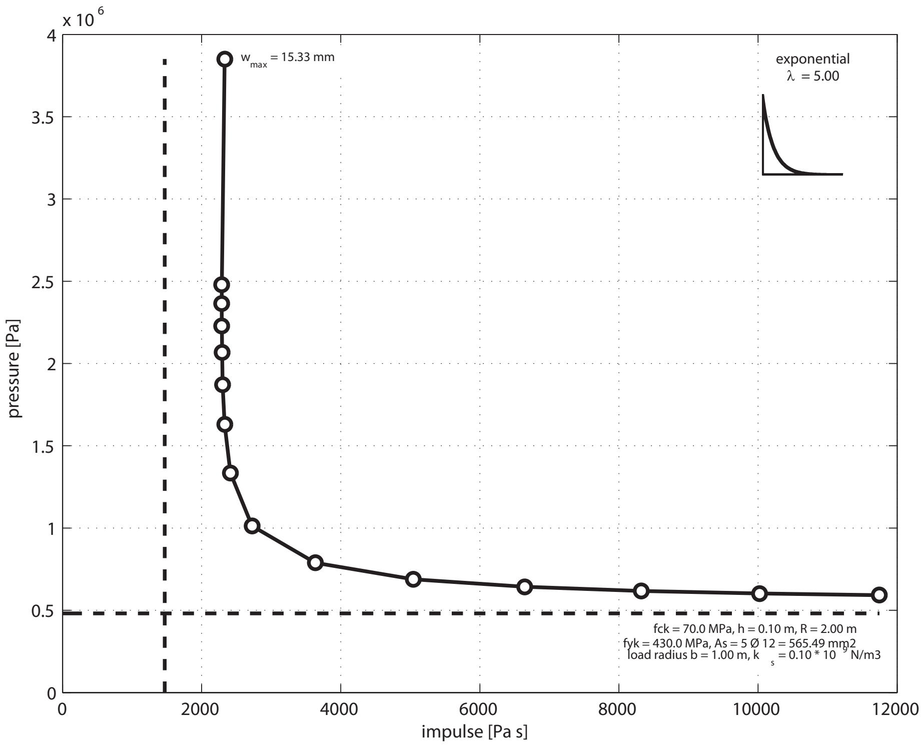

Figure 5.43: Case 2.A: example of p-i diagram for a reinforced concrete plate.

FRC. As follows, an example of the algorithms' application is performed for special plate's characteristics (figure 5.44), which correspond to a possible shock tube's sample test. The FRC material properties adopted are taken from experimental results recorded in the paper *Mechanical properties of steel fibre reinforced concrete exposed to high temperatures* (Colombo et al., 2010). Also here, gravel ($k_s = 0.10$ GPa/m) was chosen in order to represent the supporting soil.

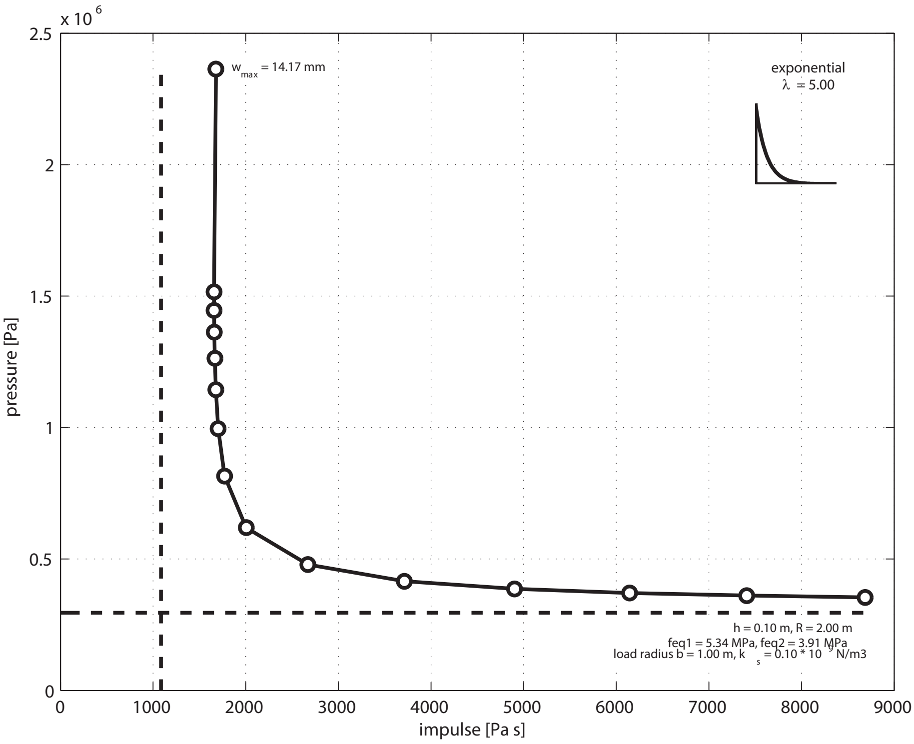

Figure 5.44: Case 2.A: example of p-i diagram for a fibre reinforced plate.

RC. The following example (figure 5.45) shows the p-i curve generated by using the algorithms proposed in this work. The geometrical dimensions and RC materials properties were adopted in order to represent a sample for the shock tube test. Dense sand ($k_s = 0.03$ GPa/m) was chosen in order to represent the supporting soil.

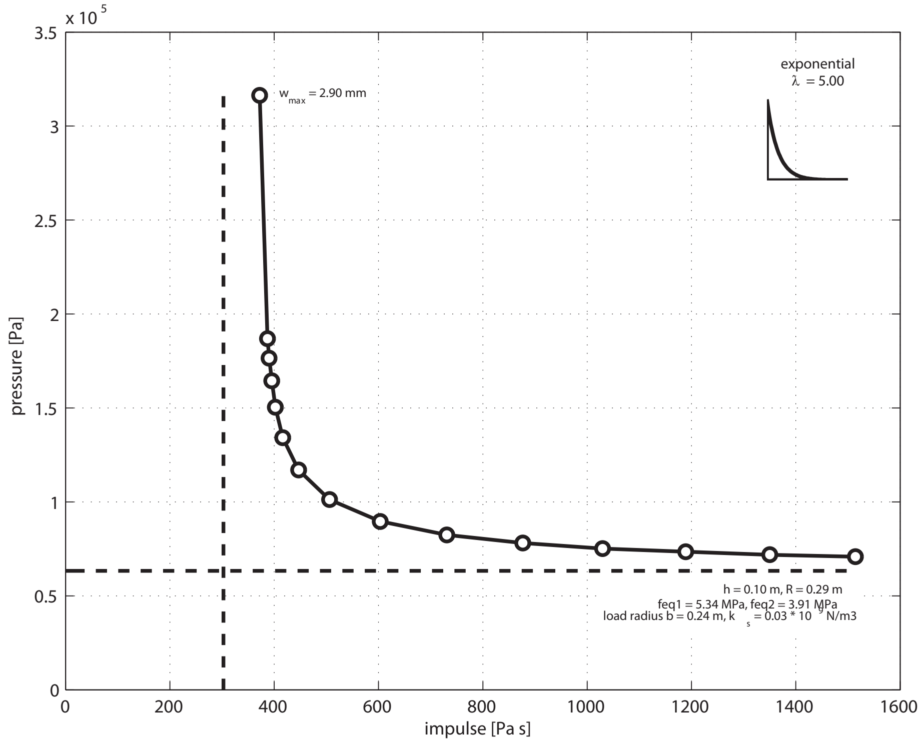

Figure 5.45: Case 2.B: example of p-i diagram for a reinforced concrete plate.

FRC. As follows, an example of the algorithms' application is performed for special plate's characteristics (figure 5.46), which correspond to a possible shock tube's sample test. The FRC material properties adopted are taken from experimental results recorded in the paper *Mechanical properties of steel fibre reinforced concrete exposed to high temperatures* (Colombo et al., 2010). Also here, dense sand ($k_s = 0.03$ GPa/m) was chosen in order to represent the supporting soil.

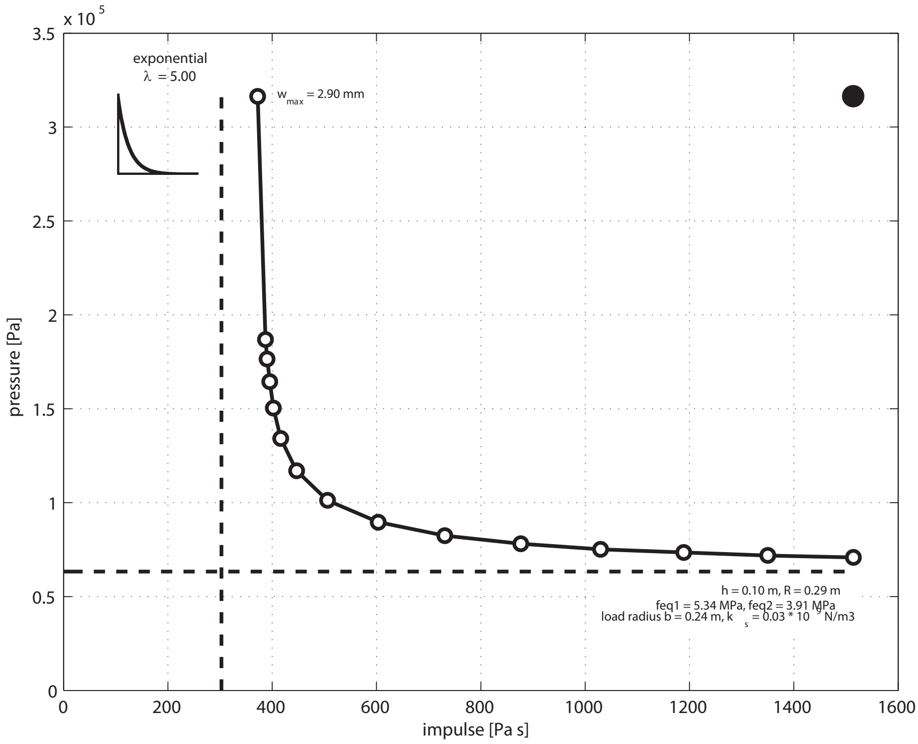

Figure 5.46: Case 2.B: example of p-i diagram for a fibre reinforced plate.

Figure 5.47 and table 5.2, which will be presented in the next pages, aim to summarize all the applications that were solved in the present work, along with the transformation coefficients and the collapse loads computed for each case.

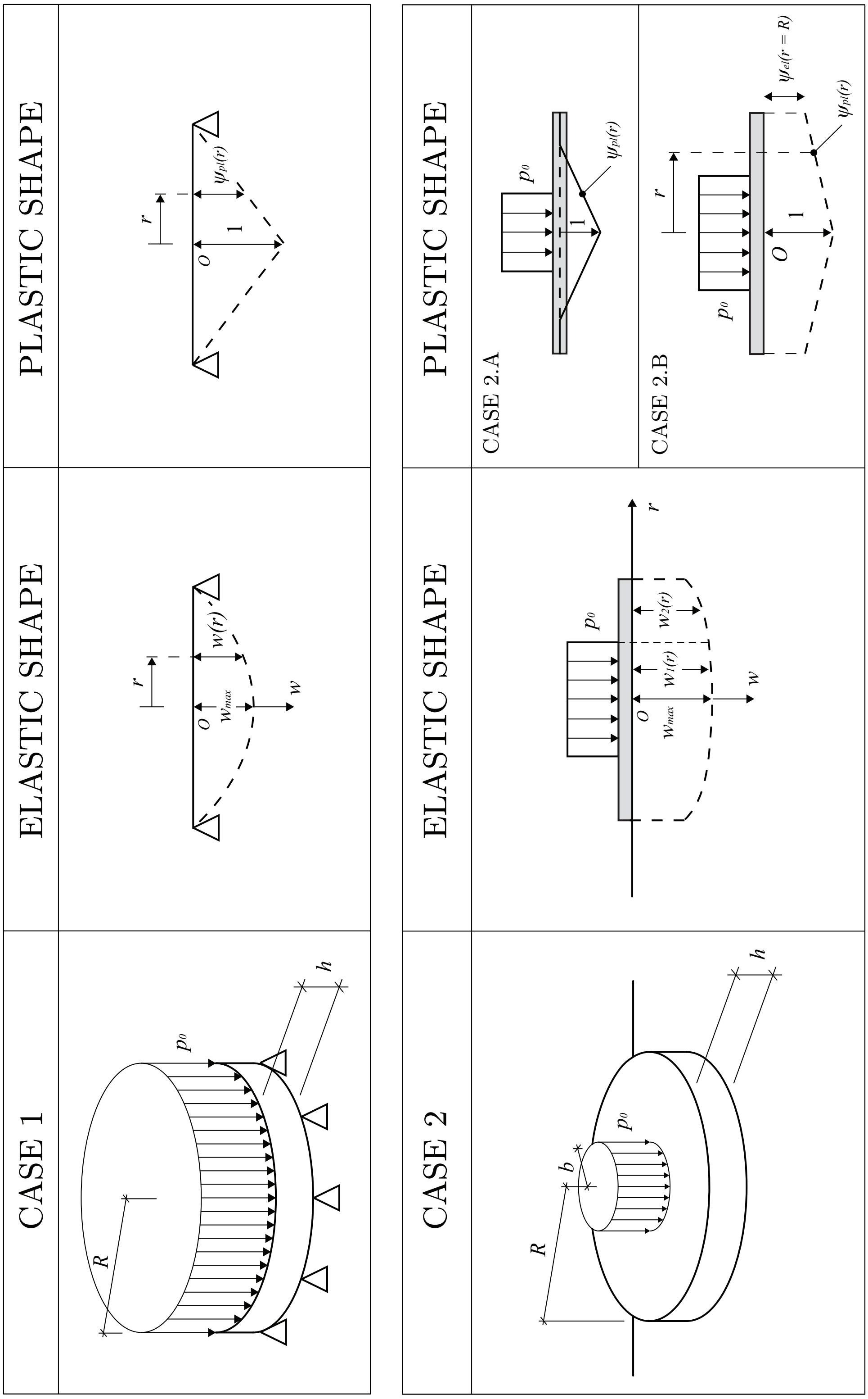

Figure 5.47: Review of the application cases.

Table 5.2: Review of the transformation coefficients for the application cases.

Case	Elastic stage coefficients	Collapse load	Plastic stage coefficients
Case 1	$m_e^* = \dfrac{\pi R^2 \rho h (3\nu^2 + 36\nu + 113)}{15(\nu+5)^2}$	$F_{su} = 6\pi m_0$	$m_p^* = \dfrac{\rho h \pi R^2}{6}$
	$k_e^* = \dfrac{64\pi D(\nu+1)(\nu+7)}{3R^2(\nu+5)^2}$		$L_p^* = \dfrac{\pi R^2}{3}$
	$L_e^* = \dfrac{\pi R^2(\nu+7)}{3(\nu+5)}$		
Case 2	$m_e^* = 2\pi\rho h \sum_{k=1}^{N_R} \psi_k^2\, k \triangle r^2$	Case 2.A	$m_p^* = \dfrac{1}{6}\rho h \pi d^2$
	for k_e^* see equation 5.140	$F_{su} = \dfrac{4\pi m_0}{1 - \dfrac{2}{3}\dfrac{b}{R}\dfrac{R}{d} - \left(\dfrac{d}{R}\right)^2 + \dfrac{1}{2}\left(\dfrac{d}{R}\right)^3}$	$L_p^* = 2\pi\left(\dfrac{b^2}{2} - \dfrac{b^3}{3d}\right)$
	$L_e^* = 2\pi \sum_{k=1}^{N_b} \psi_k\, k \triangle r^2$	Case 2.B	$m_p^* = \pi R^2 \rho h \left(\dfrac{1}{6} + \dfrac{1}{3}\psi_{el}(R) + \dfrac{1}{4}\psi_{el}^2(R)\right)$
		$F_{su} = p_0(\pi b^2) = \dfrac{3\pi m_0}{1 - \dfrac{b}{R}}$	$L_p^* = 2\pi\left[\dfrac{b^2}{2} + \dfrac{b^3}{3R}(\psi_{el}(R) - 1)\right]$

5.4 Sensitivity analysis

In all the examples so far presented only one p-i curve for each diagram has been plotted; in this section, on the contrary, some diagrams containing more than one p-i curve will be shown in order to highlight the influence arising from the variation of different parameters. Actually it is of great interest herein to understand how and to which extent the variation of a single parameter can affect the p-i curve in its whole. Some of these diagrams were developed considering either application case 1 (simply supported slab) or case 2 (slab on grade); moreover, both FRC and RC were used.

Plates with large dimension of R, under the same charge, are subjected to large bending moments as occurs analogously with beams, for instance a simply supported beam, with a uniform distribution q and length l, will have a moment at the middle span equal to $ql^2/8$, then the bending moment increases when the longitudinal dimension increases. This fact, for plates, is exposed in figure 5.48, where plates with large values of R are subjected to very large values of bending moment, therefore the undamaged zone in the p-i diagram decreases as R increases. On the other hand, large values of the thickness h increase the plate rigidity and allow to dissipate more energy, as proven by figure 5.49.

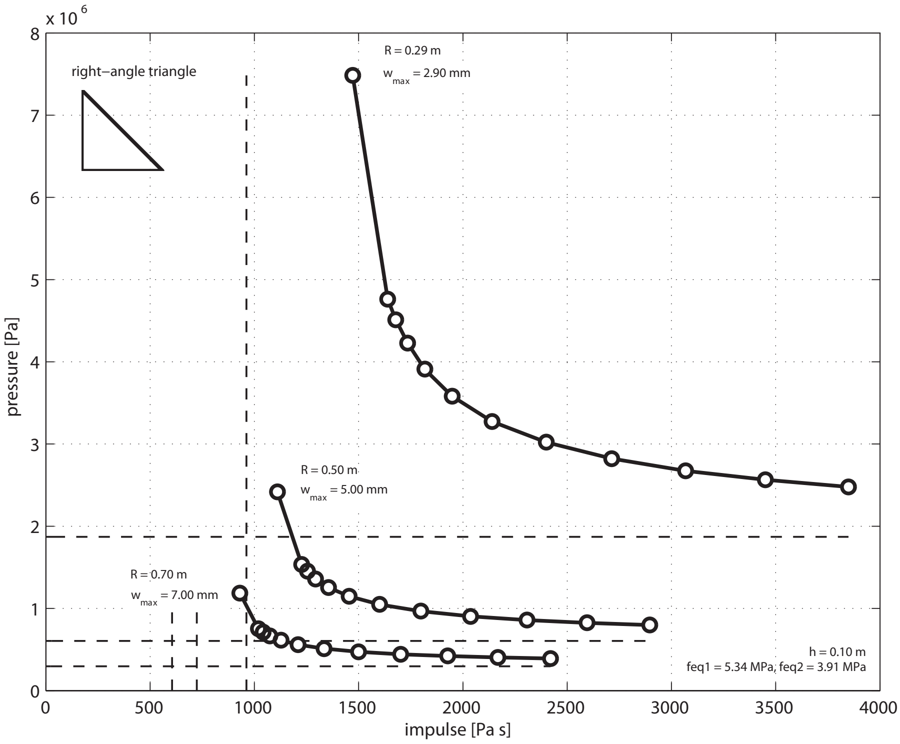

Figure 5.48: Case 1: variation of the plate radius.

Let's remember that the simplified elastic-perfectly plastic model used in this work is an approximation of a hardening behaviour with a plateau tendency. Therefore, the elastic part represents not only the strict elastic phase but also a partial plasticization coming from the appearance of some yield lines. The perfectly plastic phase (plateau) represents the entire plasticization of the system, which means the complete appearance of all yield lines necessary to reach the structural collapse. But actually the plate's plasticization has started further back, in the approximated elastic phase, as was shown in figure 3.1.

Figure 5.48 shows how a plate with a higher value of R is forced to dissipate less energy and resist less than a plate with a low value of R.
Conversely, figure 5.49 the same argument for a variation of the plate thickness h. As one would expect, an increase in the plate thickness induces an increase in its resistance against a blasting phenomenon.

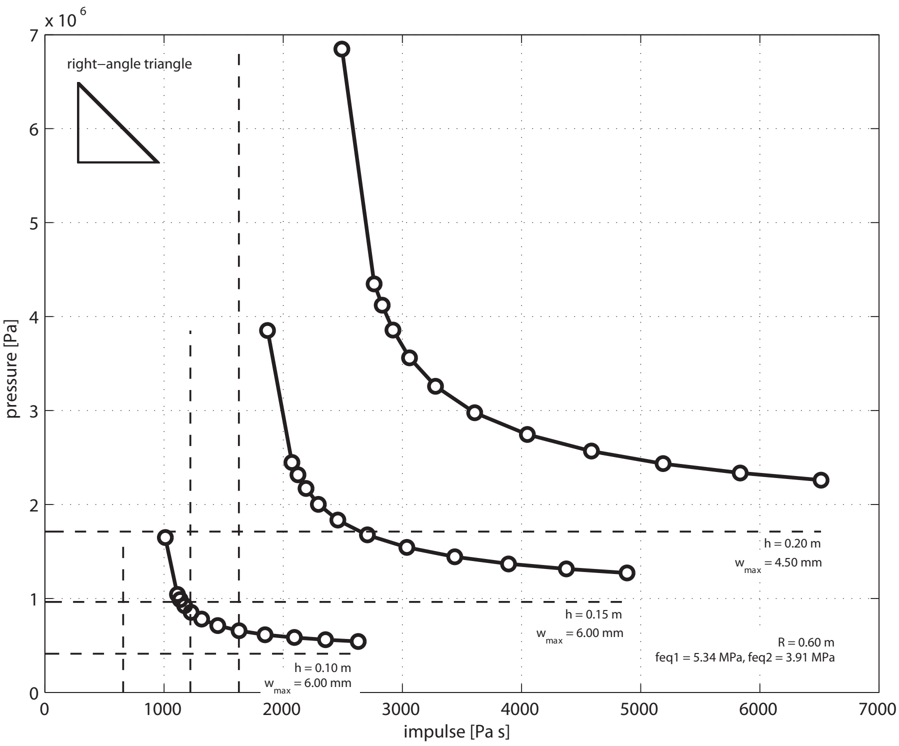

Figure 5.49: Case 1: variation of the plate thickness.

By using more resistant materials, it is expected to obtain more resistance in the overall behaviour of the plate, as it is shown in figure 5.50, in which the increasing of the cylindrical compressive strength of concrete provides an increment of the undamaged zone in the p-i diagrams.

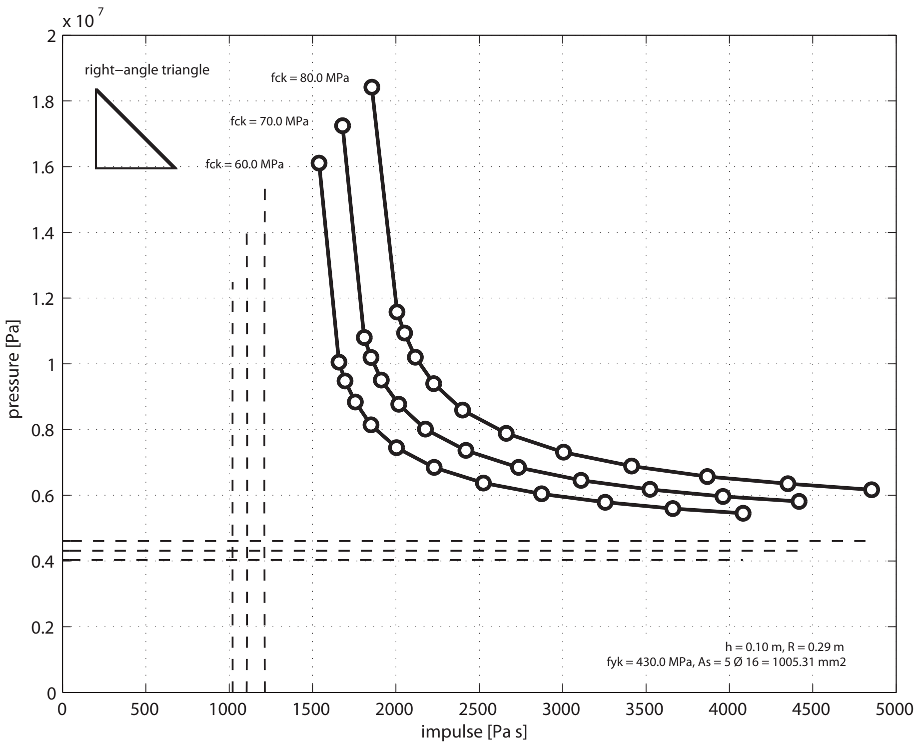

Figure 5.50: Case 1: variation of the characteristic concrete strength.

For RC plates, the increment of steel reinforcement area provides a better performance in the quasi-static domain, but a worse performance in the impulsive domain. On the contrary, a decrease in the reinforcement area provides a better performance in the impulsive domain, namely for blast loadings with short impulses and high pressures, as it is highlighted in figure 5.51.

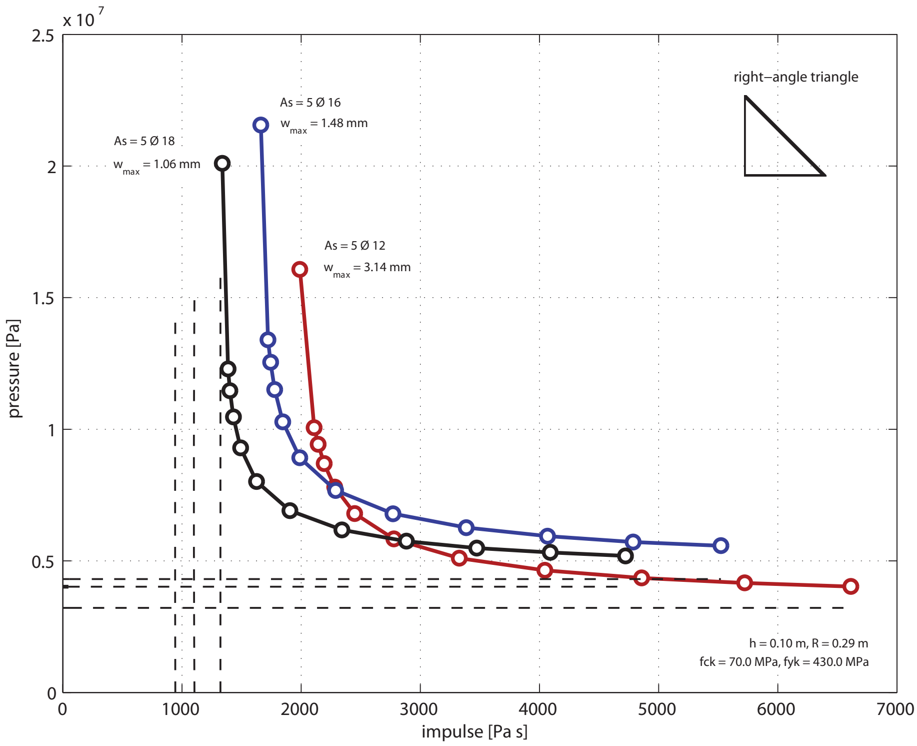

Figure 5.51: Case 1: variation of the steel area.

In figure 5.52 two functions are plotted: one was developed taking into account the partial factors (design curve), and the other one was obtained using characteristic values. As it was expected, the design curve is under the characteristic one, because the former owns a certain degree of safety. It is interesting to know how much all different partial factors affect the p-i diagram, giving rise to an overall factor of safety (FS). Looking at figure 5.52, the difference between the vertical asymptotes gives a value of FS around 1.4, while analysing the horizontal asymptotes, the FS is around 1.2. Therefore a plate will be a little more unsafe for large values of impulse than a plate subjected to a high pressure with short impulse. The design curve will find more application in the design field whilst the characteristic curve will find more application in the experimental field, in order to compare experimental and theoretical results. Furthermore, it is reasonable to expect that experimental results obtained from the shock tube test will be more likely to fall inside the area enclosed by the design and the characteristic p-i curves.

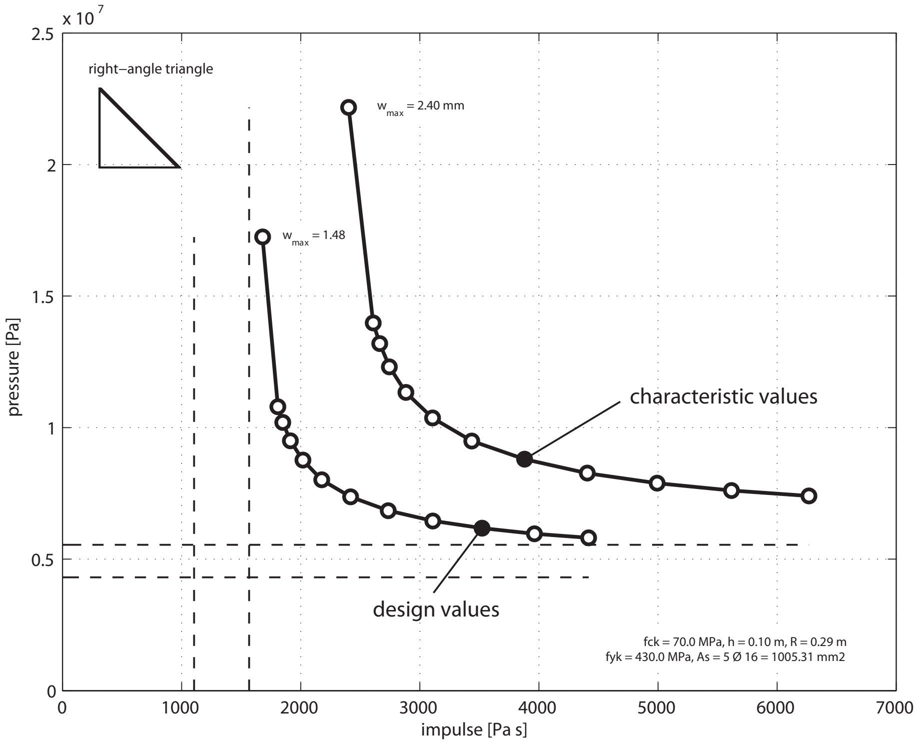

Figure 5.52: Case 1: comparison between p-i curve given by characteristic values and p-i curve given by design values.

Load pulse shape affects the structure response manly in the quasi-static and dynamic domains rather than in the impulsive regime. Figure 5.53 shows how the p-i curves tends more rapidly to the quasi-static asymptote when the load pulse shape has a greater impulse. Actually, at a same time duration of the pulse t_d, a rectangular pulse shape encloses the largest area under the pressure-time curve, i.e., it has the largest impulse, thus the p-i curve is quickly led to the horizontal asymptote. The opposite case is illustrated by the general triangle pulse shape, and all the other assumed pulse shapes appear to fall in an intermediate position between the two extreme cases.

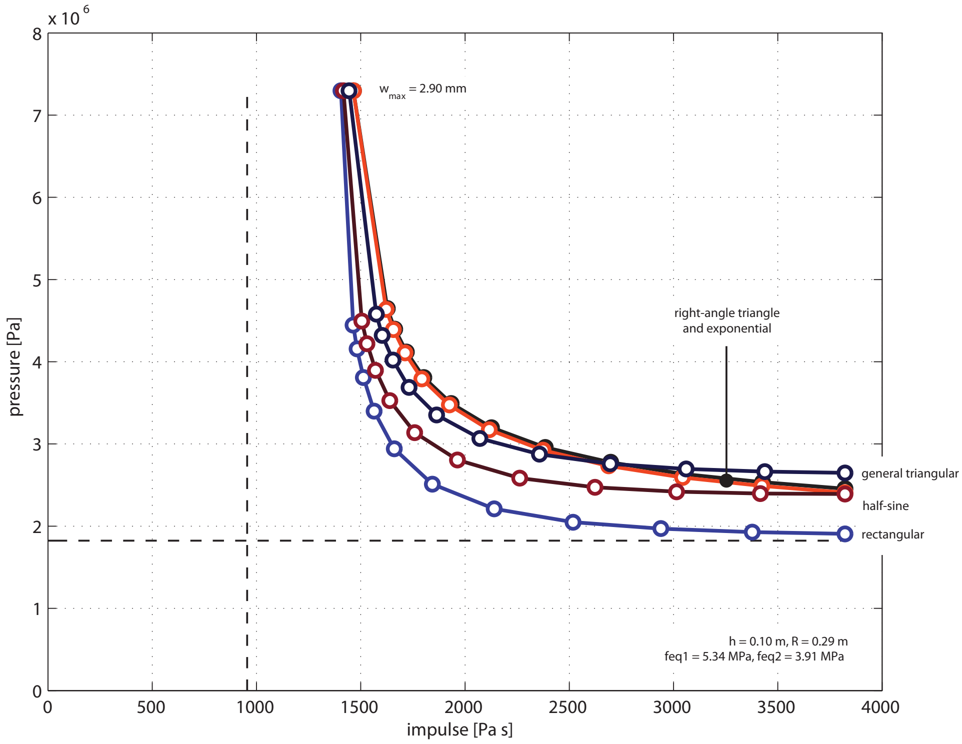

Figure 5.53: Variation of the pulse shape (case 1).

A plate supported on a deformable soil (case 2.B) will show a better performance than the one resting on a stiffer ground, due to the fact that a more deformable soil is able to dissipate more energy for the entire system, increasing its overall resistance and providing a wider undamaged zone in the p-i diagram. Figure 5.54 shows this fact for a Winkler soil medium. The values of the soil Winkler constants assumed in this frame were the following (Bowles, 1968):

- $k_s = 0.01$ GPa/m, representing loose sand;
- $k_s = 0.03$ GPa/m, representing medium dense sand;
- $k_s = 0.05$ GPa/m, representing dense sand.

Furthermore, figure 5.54 shows that the variation of the soil modulus affects mainly the impulsive and the dynamic domains, whilst negligible influence is observed for the quasi-static domain. As last remark, it is worth noting that, as one would expect, higher values of k_s provide a smaller penetration of the plate into the ground. This fact is pointed out in the figure by the $w_{plate+soil}$ values, which denote the midspan displacement of the overall plate-soil system.

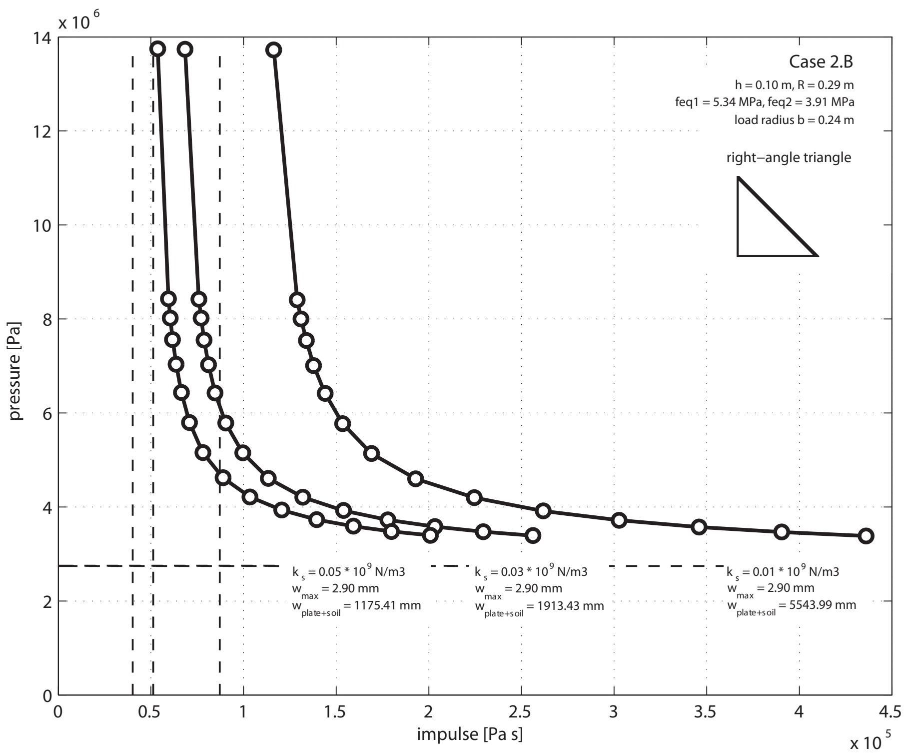

Figure 5.54: Case 2.B: variation of the Winkler constant.

Finally, always making reference to case 2.B, it is expected that an increment of the loading area (i.e., of the load radius b) will affect a plate more than a small loading area, because the total load is also increased. From a p-i diagram point of view, large charges will reduce the undamaged zone, as it is shown in figure 5.55.
Note that, as one would expect, higher values of the load radius induce a deeper embedment of the plate into the ground. This fact is pointed out in the figure by the $w_{plate+soil}$ values, which denote the midspan displacement of the overall plate-soil system.

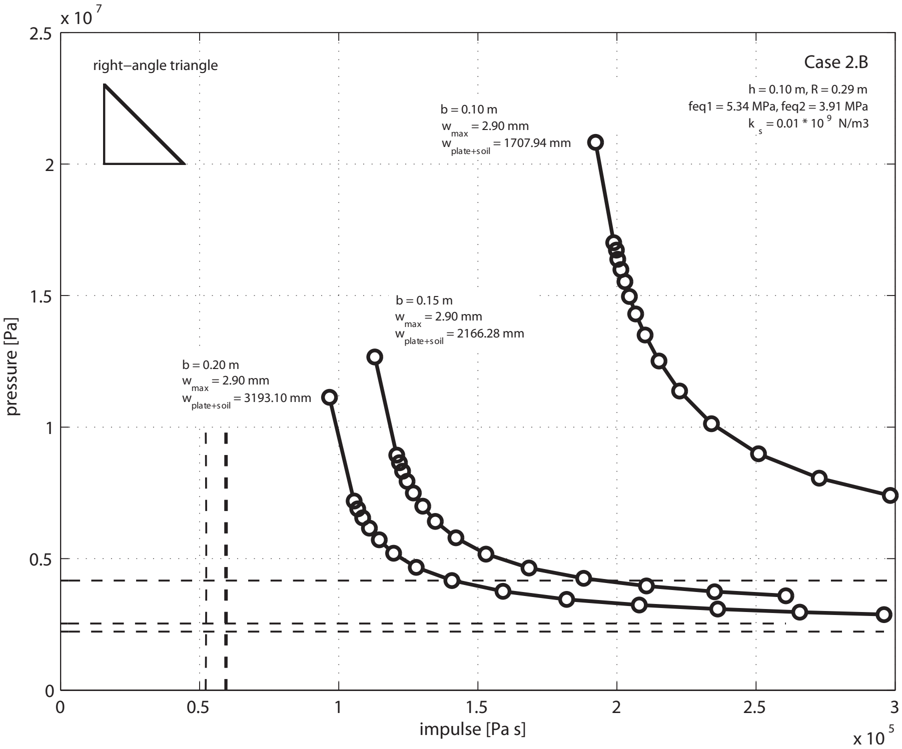

Figure 5.55: Case 2.B: variation of the load radius.

5.5 Conclusions

The results obtained in this work have essentially two aims. First, they provide a useful and powerful tool for structural designers, who will be able to implement the algorithms and p-i graphs in order to design and assess circular plates subjected to dynamic loads. Second, the results can be used to evaluate and forecast experiments performed with the shock tube.

As was already mentioned, many codes were developed within the framework of this work which allowed to perform the dynamic analyses and to work out the pressure-impulse diagrams that were herein presented. All these codes were sketched in this thesis as UML diagram representation; however, they are available in order to perform further analyses and improvements. One of the possible improvements could be the implementation of the Reissner-Mindlin theory for moderately thick plates, in order to account for shear effects.

Let's remember that the p-i diagrams plotted in this work have dimensional axes, while usually p-i diagrams performed in other works are plotted with non-dimensional axes in order to obtain comparable scales. Plotting dimensional p-i diagrams has its advantage, because the user can apply these diagrams in a direct way, just placing a point representing the desired conditions of pressure and impulse inside the p-i diagram. However, since the ratio between the vertical and the horizontal axis is very big, traditional algorithms cannot trace the complete curve. Therefore this work proposed a modification of the traditional algorithms in order to achieve a complete and well defined curve. This improvement makes the results more useful in practice.

All the analyses of plates performed in this work considered only the flexural behaviour, thereby the maximum resistance of the system corresponds to the energy dissipated by flexural plasticization. Therefore, the real experiments related to this work can be comparable with the theoretical models just in the case in which the collapse mechanism belongs to a flexural pattern and low dissipation of energy by shear mechanism takes place. This assumption has a geometrical connotation, because for values of plate diameter over plate thickness lower than 4 the shear behaviour starts having more interest, as was already mentioned at the beginning of the second chapter. For situations in which the shear mechanism of collapse assumes a predominant role more complex analyses are required, involving theories which take into account the shear behaviour in a rigorous way.

Note that the representation of the soil using a Winkler elastic medium is a strong assumption, because generally soils do not behave as purely elastic materials but as elasto-plastic softening or hardening materials. For the case 2, the soil was modelled as a infinite elastic material and its rupture was not considered. In the real world, this type of soil does not exist. Therefore, experimental tests may provide results in which the soil plasticity plays an important role and then the proposed theoretical models are not suitable any more. These phenomena are likely to happen when the plate is much more rigid than the soil, consequently for the case 2.B. In any case, the Winkler soil may be adopted in reality as an artificial elastic material, for instance in presence of a special type of rubber. In some tunnel structures, the final cover structure is supported over other previous covering material, and these could be represented as elastic materials and then they could be simulated adequately by Winkler elastic medium.

As this work is a tool for structural designers and researchers, several elements like tables, figures and graphs are provided, that will help the designer or the researcher in the choice of the right application case according to structure's particular conditions. To this aim, figure 5.22 was plotted in order to differentiate if the conditions belong either to a very rigid plate or to a very flexible plate with respect to the soil rigidity, just knowing the geometrical dimensions (R, h, b) and the stiffness parameters (k_{soil}, D) of a plate-soil system.

Finally, other structural elements different from plates could be analysed; for example, from the point of view of the analysis of tunnels subjected to explosive loadings, it would be of great interest to treat the problem of the dynamics of shell structural elements, working out the corresponding pressure-impulse diagrams.

In conclusion, open windows remain in order to complete, improve and expand this work. Further studies could take into account thick plates, different slab shapes, other boundary conditions, different dynamic excitations, elastic-plastic hardening or softening models, new materials like layered ones, application on more global structure like shells and feedbacks from experimental results aiming to an improvement of the theoretical model.

Bibliography

Abramowitz, M. and Stegun, I. A. (1965). *Handbook of Mathematical Functions.* Dover Publications.

Alaoui, S. and Oswald, C. (2007). Blast-resistant design considerations for precast, prestressed concrete structures. *PCI Journal.*

Asprone, D., Jalayer, F., Prota, A., and Manfredi, G. (2010). Proposal of a probabilistic model for multi-hazard risk assessment of structures in seismic zones subjected to blast for the limit state of collapse. *Structural Safety*, 32:25–34.

Baker, W. E., Cox, P. A., Westine, P. S., Kulesz, J. J., and Strehlow, R. A. (1983). *Explosion Hazards and Evaluation.* Elsevier Scientific Publishing Company.

Belluzzi, O. (1966). *Scienza delle Costruzioni Vol. 3.* Zanichelli.

Biggs, J. M. (1964). *Introduction to Structural Dynamics.* McGraw-Hill.

Blasko, J. R., Krauthammer, T., and Astarlioglu, S. (2004). Pressure-impulse diagrams for reinforced concrete slabs. Technical report, University Park, PA: Protective Technology Center, The Pennsylvania State University.

Bowles, J. E. (1968). *Foundation Analysis and Design.* McGraw-Hill.

Bulson, P. S. (1997). *Explosive Loading of Engineering Structures.* Chapman & Hall.

Campidelli, M. and Viola, E. (2007). An analyticalnumerical method to analyze single degree of freedom models under airblast loading. *Journal of Sound and Vibration*, 302:260–286.

Cardano, G. (1993). *Ars magna or The Rules of Algebra.* Dover Publications.

CEB-FIP (1993). *Model Code 1990.* Thomas Telford.

Chen, W.-F. and Han, D.-J. (1988). *Plasticity for Structural Engineers.* Springer.

Chopra, A. K. (1995). *Dynamics of Structures.* Prentice-Hall.

Clough, R. W. and Penzien, J. (1993). *Dynamics of Structures.* Prentice-Hall.

Colombo, M., Prisco, M. D., and Felicetti, R. (2010). Mechanical properties of steel fibre reinforced concrete exposed at high temperatures. *Materials and Structures*, 43:475–491.

Corigliano, A. and Taliercio, A. (2005). *Meccanica Computazionale*. Editrice Esculapio.

Earnshaw, S. (1860). On the mathematical theory of sound. *Philosophical Transactions of the Royal Society of London*, 150:133–148.

El-Dakhakhni, W. W., ASCE, M., Mekky, W. F., and Changiz-Rezaei, S. H. (2009). Vulnerability screening and capacity assessment of reinforced concrete columns subjected to blast. *Journal of Performance of Constructed Facilities*, pages 353–365.

Fallah, A. S. and Louca, L. A. (2007). Pressureimpulse diagrams for elastic-plastic-hardening and softening single-degree-of-freedom models subjected to blast loading. *International Journal of Impact Engineering*, 34:823–842.

Farlow, S. J. (1993). *Partial Differential Equations for Scientists and Engineers*. Dover Publications.

Feldgun, V. R., Kochetkov, A. V., Karinski, Y. S., and Yankelevsky, D. Z. (2008). Internal blast loading in a buried lined tunnel. *International Journal of Impact Engineering*, 35:172–183.

Ferrara, L., Prisco, M. D., Colombo, M., and Mauri, M. (2004). On the identification of sfrc constitutive law in uniaxial tension. *Fibre-reinforced concretes*, pages 827–836.

Fischer, K. and Hring, I. (2009). Sdof response model parameters from dynamic blast loading experiments. *Engineering Structures*, 31:1677–1686.

Florek, J. and Benaroya, H. (2005). Pulsepressure loading effects on aviation and general engineering structures - review. *Journal of Sound and Vibration*, 284:421–453.

Fowler, M. (2003). *UML Distilled Third Edition*. Addison-Wesley.

Gong, S., Lu, Y., Tu, Z., and Jin, W. (2009). Validation study on numerical simulation of rc response to close-in blast with a fully coupled model. *Structural Engineering and Mechanics*, 32:283–300.

Ishikawa, N. and Beppu, M. (2007). Lessons from past explosive tests on protective structures in japan. *International Journal of Impact Engineering*, 34:1535–1545.

Jahnke, E. and Emde, F. (1945). *Tables of Functions with Formulae and Curves*. Dover Publications.

Jirasek, M. and Bazant, Z. P. (2001). *Inelastic Analysis of Structures*. Wiley.

Johansen, K. W. (1972). *Yield-line formulae for slabs*. Taylor & Francis.

Kaplunov, J. D., Kossovich, L. Y., and Nolde, E. V. (1998). *Dynamics of Thin Walled Elastic Bodies*. Academic Press.

Krauthammer, T. (2008). *Modern Protective Structures*. CRC Press.

Krauthammer, T., Astarlioglu, S., Blasko, J., Soh, T., and Ng, P. (2008). Pressure impulse diagrams for the behavior assessment of structural components. *International Journal of Impact Engineering*, 35:771–783.

Lamb, H. (1895). *Hydrodynamics*. Cambridge University Press.

Lan, S., Lok, T.-S., and Heng, L. (2005). Composite structural panels subjected to explosive loading. *Construction and Building Materials*, 19:387–395.

Li, G.-Q., Yang, T.-C., and Chen, S.-W. (2009). Behavior and simplified analysis of steel-concrete composite beams subjected to localized blast loading. *Structural Engineering and Mechanics*, 32:337–350.

Li, Q. M. and Meng, H. (2002a). Pressure-impulse diagram for blast loads based on dimensional analysis and single-degree-of-freedom model. *Journal of Engineering Mechanics*, pages 87–92.

Li, Q. M. and Meng, H. (2002b). Pulse loading shape effects on pressureimpulse diagram of an elasticplastic, single-degree-of-freedom structural model. *International Journal of Mechanical Sciences*, 44:1985–1998.

Lindberg, H. E. and Firth, R. O. (1967). Afwl-tr-66163. Technical report, Air Force Weapons Lab, Kirtland, USA.

Low, H. Y. and Hao, H. (2001). Reliability analysis of reinforced concrete slabs under explosive loading. *Structural Safety*, 23:157–178.

Low, H. Y. and Hao, H. (2002). Reliability analysis of direct shear and flexural failure modes of rc slabs under explosive loading. *Engineering Structures*, 24:189–198.

Lu, Y. (2009). Modelling of concrete structures subjected to shock and blast loading: An overview and some recent studies. *Structural Engineering and Mechanics*, 32:235–249.

Luccioni, B. M. and Luege, M. (2006). Concrete pavement slab under blast loads. *International Journal of Impact Engineering*, 32:1248–1266.

Ma, G. W., Huang, X., and Li, J. C. (2009). Damage assessment for buried structures against internal blast load. *Structural Engineering and Mechanics*, 32:301–320.

Ma, G. W., Shi, H. J., and Shu, D. W. (2007). Pi diagram method for combined failure modes of rigid-plastic beams. *International Journal of Impact Engineering*, 34:1081–1094.

Magrab, E. B., Azarm, S., Balachandran, B., Duncan, J., Herold, K., and Walsh, G. (2010). *An Engineer's Guide to MATLAB*. Prentice-Hall.

Meda, A. (2003). On the extension of the yield line method to the design of sfrc slabs on grade. *Studies and researches*, 24:223–237.

Morison, C. M. (2006). Dynamic response of walls and slabs by single-degree-of-freedom analysis - a critical review and revision. *International Journal of Impact Engineering*, 32:1214–1247.

Ngo, T. and Mendis, P. (2009). Modelling the dynamic response and failure modes of reinforced concrete structures subjected to blast and impact loading. *Structural Engineering and Mechanics*, 32:269–282.

Park, J. Y. and Krauthammer, T. (2009). Inelastic two-degree-of-freedom model for roof frame under airblast loading. *Structural Engineering and Mechanics*, 32:321–335.

Philip, E. B. (1944). Blast pressure and impulse in a tunnel: a note on the latest piezo-gauge measurements. Technical report, UK Home Office.

Save, M. A., Massonnet, C. E., and de Saxce, G. (1997). *Plastic Limit Analysis of Plates, Shells and Disks.* Elsevier Scientific Publishing Company.

Scherbatiuk, K., Rattanawangcharoen, N., Pope, D. J., and Fowler, J. (2008). Generation of a pressureimpulse diagram for a temporary soil wall using an analytical rigid-body rotation model. *International Journal of Impact Engineering*, 35:530–539.

Selvadurai, A. P. S. (1979). *Elastic Analysis of Soil-Foundation Interaction.* Elsevier Scientific Publishing Company.

Shi, Y., Hao, H., and Li, Z.-X. (2008). Numerical derivation of pressure-impulse diagrams for prediction of rc column damage to blast loads. *International Journal of Impact Engineering*, 35:1213–1227.

Stewart, M. G. and Netherton, M. D. (2008). Security risks and probabilistic risk assessment of glazing subject to explosive blast loading. *Reliability Engineering and System Safety*, 93:627–638.

Talaslidis, D. G., Manolis, G. D., Paraskevopoulos, E., Panagiotopoulos, C., Pelekasis, N., and Tsamopoulos, J. A. (2004). Risk analysis of industrial structures under extreme transient loads. *Soil Dynamics and Earthquake Engineering*, 24:435–448.

Timoshenko, S. P. and Woinowsky-Krieger, S. (1959). *Theory of Plates and Shells.* McGraw-Hill.

Ventsel, E. and Krauthammer, T. (2001). *Thin Plates and Shells.* Marcel Dekker, Inc.

VV.AA. (2004). *Eurocode 2: Design of concrete structures.* European Committee for Standardization (CEN).

VV.AA. (2006). Istruzioni per la progettazione, esecuzione ed il controllo di strutture di calcestruzzo fibrorinforzato. Technical report, Consiglio Nazionale delle Ricerche.

Wang, M. L. and Tan, L.-Z. (1995). Stochastic techniques for analyzing shallow-buried reinforced concrete box-type structure. *Soil Dynamics and Earthquake Engineering*, 14:279–287.

Young, W. and Budynas, R. (2001). *Roark's Formulas For Stress And Strain*. McGraw-Hill.

Zhou, X. Q., Kuznetsov, V. A., Hao, H., and Waschl, J. (2008). Numerical prediction of concrete slab response to blast loading. *International Journal of Impact Engineering*, 35:1186–1200.